Tyler, Damian J. (2002) Quantitative measurements in obstetric MRI. PhD thesis, University of Nottingham.

Quantitative Measurements in Obstetric MRI

By Damian J Tyler, M.Sci.

Thesis submitted to the University of Nottingham for the degree of

Doctor of Philosophy, May 2002.

INDEX

<u>Abstract</u>

This thesis describes the development and application of quantitative echo planar magnetic resonance imaging techniques to the study of human placental development in normal and compromised pregnancies.

Initially, a method of rapidly and accurately measuring the transverse relaxation time is proposed using a multi-echo measurement sequence. The method is described, validated on $CuSO_4$ phantoms and applied in the study of the human placenta and gastric dilution. It is shown that the inversion provided by sinc pulses is insufficient to generate an accurate measurement but using adiabatic refocusing pulses yields a measurement that is comparable with a single spin echo.

Subsequently, a rapid magnetisation transfer method is presented that allows the quantification of the relative size of the bound proton pool. An experimental pulse sequence is proposed, along with a theoretical model, that permits the investigation of the bound proton pool's transition towards the steady state. The sequence and model are validated using agar gel phantoms and shown to agree well with literature values. When applied in the study of the human placenta, it is shown that there is no significant variation in the fitted value of the bound proton pool size with increasing gestational age or in compromised pregnancies.

Finally, several methods of measuring the oxygenation level of blood within the human placenta are investigated. The signal intensities of cardiac gated T_2^* and T_2 weighted images acquired at various points in the maternal cardiac cycle are explored but no significant variation is shown through the cycle. A pulsed gradient spin echo sequence that utilises anti-symmetric sensitising gradients is validated and then applied in the human placenta. Oxygenation measurements with this technique are shown to be unfeasible but the potential of the sequence to monitor blood flow in the placenta is demonstrated.

Acknowledgements

I would gratefully like to thank the following people for all the help and assistance that they have given me over the last three years.

Dr Penny Gowland for all her support, encouragement and ideas. And for always having the answer.

The Medical Research council for providing the funding for my studies and research.

Prof Richard Bowtell, Prof Peter Morris, Dr Sue Francis, Dr Paul Glover, Dr Helen Geen, Dr Martin Benscik, Dr David Rourke, Dr Malcom Prior and Dr Sekhar Ramanathan for answering my questions and helping to fill in the gaps.

Dr Ron Coxon and Dr Andy Peters for their continual assistance with all things computerised.

Mr Paul Clark and Mr Ian Thexton for all their help making, fixing and improving all the bits and bobs of hardware that I have needed and Mr D Jephcote for his amazing ability to acquire everything that I ever needed, no matter how strange the requests.

Mrs Dawn Lemon, Mrs Wendy Phillips, Mrs Julie Kenney, Mrs Margaret Carter, Mrs Stephanie Hill and Miss Melanie Stretton for their never ending help in pointing me in the right direction and generally making life that little bit easier.

Jamie, Nav, Andrea, Davide and Kay who at some stage have been 'office buddies' and managed to put up with me.

Rachel, Luca, Jon and Caroline, the 'half T' group, old and new, for constantly helping to keep the scanner going and being the only ones who really understand the magic of the gradient filters.

Prof. Phil Baker, Prof. Ian Johnson, Dr Bryony Strachan, Dr Keith Duncan, Dr Rachel Duckett and Dr Stephen Ong for medical assistance throughout the project.

Andy G, Sarah, Jane, Peck, Alex, Axel, Mike, Paul, Adnan, Jiabao, Dan Konn, Dan Green, Jim, Charles, Alison, Ben, Jose, Jennie and all the other post grads, past and present, who have all in some way made the MR centre the fun place to work that it has been for the last three years.

Lee, Paul and Anna, housemates of Harrington Drive, who had to cope with my occasionally irrational mood swings.

My parents for their continued support and encouragement, not only for the last three years, but all the way through and for making me believe I could do it.

And finally Charlotte, for always providing the distraction I needed and making the whole thing worthwhile.

1   Introduction

1.1   Project Outline

Pregnancy is a condition that can be severely affected by numerous incidental diseases. In England and Wales in the 1930's, due directly to pregnancy and childbirth, there were about 5 maternal deaths and approximately 60 perinatal deaths for every 1000 total births. By the 1990's this value had fallen to around 5 maternal deaths per 100 000 total births and 8 perinatal deaths per 1000 total births[1]. Although this reduction is mainly due to improvements in social conditions, a large factor must be due to the continual development of obstetric care. The ability to diagnose problems that previously would have gone undetected has enabled patients to be given the care needed to ensure safe delivery of the fetus. Conditions, such as Eclampsia due to untreated Pre-Eclampsia (PE), that were once a major cause of maternal mortality are now considered to be preventable.

To further reduce the perinatal mortality rate, it is necessary to further improve the diagnostic techniques used in obstetrics and to increase our understanding of the aetiology of complications of pregnancy. Diagnostic techniques, such as Ultrasound (US) and Cardiotocography (CTG) are very useful in the monitoring of fetal well-being, but they yield very little quantitative information[1]. It is possible to produce measurements of fetal volume by ultrasound but preliminary studies already show that measurements of fetal organ volume are significantly more accurate when using Magnetic Resonance Imaging (MRI)[2]. It has also been suggested that fetal liver measurements could prove useful in the diagnosis of Intrauterine Growth Restriction (IUGR)[3]. However, the real power of obstetric

MRI lies in its ability to quantitatively measure parameters that could further our understanding of the causes of complications in pregnancy[4,5,6].

The development of ultra fast techniques for MRI, such as EPI, FLASH and HASTE, has lead to a great deal of recent advancement in the field of obstetric MRI. Artefacts caused by unpredictable and non-periodic fetal motion have previously hampered the use of MRI in pregnancy. The irregular nature of the fetal movement means that simple artefact reduction techniques, such as gating, cannot be used. Of these rapid techniques, Echo Planar Imaging (EPI) has several major advantages for fetal imaging. Firstly the speed of image production is said to 'freeze' fetal motion, preventing the production of artefacts. The speed also minimises the total scanning time and therefore helps to reduce patient discomfort and stress.

Secondly, the images are acquired following a single Radiofrequency (RF) excitation pulse meaning that the power deposition within the patient is minimal, an obvious advantage when scanning a fetus where temperature regulation may be compromised. Also, the susceptibility of the fetus and surrounding maternal tissue are well matched, reducing susceptibility artefacts that can cause serious problems with EPI images. Finally, the EPI sequence is very modular in nature and so allows for the easy addition of preparation sequences prior to imaging. This allows the straightforward measurement of properties, such as relaxation times and diffusion coefficients.

The soft tissue contrast that can be obtained when using MRI, especially when weighting images using variations in the relaxation times, makes it an ideal tool for obstetric imaging. In addition, the quantitative results that can be achieved

with EPI provide a significant advantage over other diagnostic imaging techniques.

1.2 Scope of Thesis

The work presented in this thesis describes the work I have carried out during the period from September 1998 to August 2001 within the Magnetic Resonance Annexe of the School of Physics and Astronomy at the University of Nottingham. The initial aim was to examine different ways of producing accurate and reproducible quantitative measurements of the human placenta *in vivo* to enable the study of complications of pregnancies such as Pre-Eclampsia and IUGR.

Chapters 2 and 3 provide a theoretical overview of Nuclear Magnetic Resonance (NMR) and MRI. The major steps in the development of a versatile imaging modality are described along with the basic theory needed to explain each of the developments. A basic overview of the fundamental theory behind magnetic resonance parameters such as relaxation times and magnetisation transfer is given along with a description of the basic pulse sequences used to measure them. The k-space representation of imaging procedures is explained and used to describe some of the early image acquisition techniques that led to the development of EPI. The theory behind EPI is then provided in greater detail.

The experimental hardware that has been used to acquire all of the data presented in this thesis is subsequently described in chapter 4. Each aspect of the equipment needed for a MRI scanner is briefly explained with particular reference to the specific system design employed at the University of Nottingham.

Chapter 5 examines the normal anatomy and development of the fetus and placenta during human pregnancy. The initial stages of development are described

to provide an understanding of the normal method of placental implantation and the growth of the maternal and fetal vascular systems. The pathologies of Pre-Eclampsia and IUGR are subsequently described with reference to the normal anatomy previously mentioned.

Chapter 6 provides an overview of safety considerations in the MRI environment. The three main sources of safety concern, namely the static, the spatially and temporally varying and the radiofrequency magnetic fields, are separately explained. The specific safety concerns relating to the application of MRI in the study of human pregnancy are then described with reference to the safety studies previously carried out at the University of Nottingham.

In chapter 7 a rapid and accurate pulse sequence for the measurement and mapping of the transverse relaxation time from a single Free Induction Decay (FID) is proposed. The sequence uses a combination of accurate Multi-Echo (ME) measurements and rapid imaging techniques. To overcome the effect of RF pulse errors in multi-echo sequences, the application of adiabatic refocusing pulses to provide improved accuracy is discussed and the proposed sequence validated against a single spin echo EPI sequence. The validated sequence is then applied in the measurement of the transverse relaxation time of the human placenta. The usefulness of the sequence is further demonstrated with its application in the study of gastric function through the monitoring of gastric dilution and the functionality of an antacid preparation.

A technique for producing a quantitative measure of Magnetisation Transfer (MT) on a clinically feasible time scale is proposed in chapter 8. Through the combination of pulsed off-resonance irradiation and EPI image acquisition, a quantitative imaging sequence that negates the need for continuous wave

irradiation is created. A model is proposed for data analysis involving the step-by-step solution of the Bloch equations to generate a quantitative measure of the bound proton pool size. The sequence and model are applied in the study of a series of agar gels of varying concentrations and the results compared to those from the literature. An improvement to the model is suggested to allow for the measurement of the transverse relaxation time of the bound proton pool and the improvement is subsequently validated with the use of the agar gels. The chapter then concludes with a description of the application of the sequence in a longitudinal and cross-sectional study of the human placenta in an attempt to provide further information about the source of relaxation time variations previously shown with gestational age and condition of pregnancy.

Chapter 9 presents a summary of the work carried out in an attempt to produce a direct measurement of the oxygenation level within the human placenta. The initial sections focus on the variation of signal intensities through the maternal cardiac cycle via the acquisition of cardiac gated T_2^* and T_2 weighted images. Later sections concentrate on the investigation of a Pulsed Gradient Spin Echo (PGSE) sequence that uses anti-symmetric sensitising gradients to measure diffusion. The ability of the sequence to overcome errors introduced by background gradients is initially validated against a standard PGSE sequence. The sequence is then applied in the human placenta and although no background gradients are measured, the sequence is used to investigate blood flow within the placenta.

Chapter 10 contains a brief summary of the results obtained and details the key findings of the work. Possible future directions for the project are also presented along with suggestions for applications of the work in different clinical settings.

References

[1] Hull, M., et al., *Undergraduate Obstetrics and Gynaecology*. 3rd ed. 1997: Butterworth-Heinemann. 467.

[2] Baker, P.N., et al., *Fetal Weight Estimation by Echo-Planar Magnetic-Resonance- Imaging*. Lancet, 1994. **343**(8898): p. 644-645.

[3] Baker, P.N., et al., *Measurement of Fetal Liver, Brain and Placental Volumes with Echo-Planar Magnetic-Resonance-Imaging*. British Journal of Obstetrics and Gynaecology, 1995. **102**(1): p. 35-39.

[4] Francis, S.T., et al., *Non-invasive mapping of placental perfusion*. Lancet, 1998. **351**(9113): p. 1397-1399.

[5] Gowland, P.A., et al., *In vivo relaxation time measurements in the human placenta using echo planar imaging at 0.5 T*. Magnetic Resonance Imaging, 1998. **16**(3): p. 241-247.

[6] Moore, R.J., et al., *In utero perfusing fraction maps in normal and growth restricted pregnancy measured using IVIM echo-planar MRI*. Placenta, 2000. **21**(7): p. 726-732.

[7] Baker, P.N., et al., *Estimation of Fetal Lung Volume Using Echo-Planar Magnetic Resonance Imaging*. Obstetrics and Gynecology, 1994. **83**(6): p. 951-954.

[8] Duncan, K.R., et al., *Assessment of fetal lung growth in utero with echo-planar MR imaging*. Radiology, 1999. **210**(1): p. 197-200.

[9] Gowland, P.A., et al., *In vivo perfusion measurements in the human placenta using echo planar imaging at 0.5 T*. Magnetic Resonance in Medicine, 1998. **40**(3): p. 467-473.

[10] Johnson, I.R., et al., *Imaging the Pregnant Human-Uterus with Nuclear Magnetic- Resonance*. American Journal of Obstetrics and Gynecology, 1984. **148**(8): p. 1136-1139.

[11] Johnson, I.R., et al., *Study of Internal Structure of the Human Fetus Inutero by Echo- Planar Magnetic-Resonance-Imaging*. American Journal of Obstetrics and Gynecology, 1990. **163**(2): p. 601-607.

[12] Levine, D. and P.D. Barnes, *Cortical maturation in normal and abnormal fetuses as assessed with prenatal MR imaging*. Radiology, 1999. **210**(3): p. 751-758.

[13] Mansfield, P., et al., *Echo Planar Imaging of the Human Fetus Inutero at 0.5-T*. British Journal of Radiology, 1990. **63**(755): p. 833-841.

[14] Moore, R.J., et al., *In vivo intravoxel incoherent motion measurements in the human placenta using echo-planar imaging at 0.5 T*. Magnetic Resonance in Medicine, 2000. **43**(2): p. 295-302.

[15] Moore, R.J., et al., *In vivo diffusion measurements as an indication of fetal lung maturation using echo planar imaging at 0.5T*. Magnetic Resonance in Medicine, 2001. **45**(2): p. 247-253.

[16] Moore, R.J., et al., *Antenatal determination of fetal brain activity in response to an acoustic stimulus using functional magnetic resonance imaging*. Human Brain Mapping, 2001. **12**(2): p. 94-99.

[17] Powell, M.C., et al., *Magnetic-Resonance Imaging (Mri) in Obstetrics .2. Fetal Anatomy*. British Journal of Obstetrics and Gynaecology, 1988. **95**(1): p. 38-46.

[18] Roberts, N., et al., *Estimation of Fetal Volume by Magnetic-Resonance-Imaging and Stereology*. British Journal of Radiology, 1994. **67**(803): p. 1067-1077.

[19] Smith, F.W., et al., *NMR Imaging in Human Pregnancy: A Preliminary Study*. Magnetic Resonance Imaging, 1984. **2**: p. 57-64.

[20] Stehling, M.K., et al., *Echo-Planar Imaging of the Human Fetus Inutero*. Magnetic Resonance in Medicine, 1990. **13**(2): p. 314-318.

2   Theory of Nuclear Magnetic Resonance (NMR)

2.1   An Historical Overview

In the history of NMR, the first major discovery was that of the nuclear spin, which was initially postulated in 1924 by Pauli to describe the hyperfine structure of atomic spectra. However, it was 15 years later that Rabi first demonstrated nuclear magnetic resonance by using a beam of hydrogen molecules in a static magnetic field and measuring the specific radiofrequency absorption. In 1945, Purcell *et al* working at Harvard University observed the NMR phenomenon in solid paraffin wax, whilst at the same time Bloch *et al* working at Stanford University did likewise with water. Both groups published their results in the same issue of Physical Review and went on to share the Nobel Prize in 1952 for their work. The next major step came with the discovery by Hahn in 1950 of the spin echo. He showed that it was possible to produce an echo of the NMR signal with the use of two pulses of radiofrequency magnetic fields. By 1953 the first commercial spectrometers were being produced and the introduction of Fourier Transform (FT) NMR spectroscopy by Ernst and Anderson in 1966 has gone on to ensure that NMR is a vital tool in the field of analytical spectroscopy[1].

2.2   The Quantum Mechanical Approach

2.2.1   NMR Nuclei

The phenomenon of NMR has its basis in the fact that certain nuclei possess a property known as spin, which can be visualised as a rotation of the nucleus about its own axis. Spin can be described by the quantum number, I, and can have integer, half integer or zero value depending on the combination of protons and neutrons contained within the nucleus. As with all spinning objects, these nuclei

have angular momentum and due to their charge, magnetic properties equivalent to a current circulating in a loop of wire. This means that a nucleus can be visualised as a tiny bar magnet rotating about its own axis. Quantum mechanical theory tells us that the magnitude of the angular momentum of a nucleus can only take certain values determined by the spin number of the nucleus as described by equation 2.1.

$$P = \hbar[I(I+1)]^{1/2}$$
  -     2.1

Where $\hbar$ is h/2π. The angular momentum is a vector property and can be further described by the quantum number, m, which comes about because the angular momentum can only have discrete values with respect to a given direction. For example if we define a set of Cartesian axes, we can write the angular momentum along the z axis using equation 2.2, where m can take any of the 2I+1 integer step values between I and -I.

$$P_z = m\hbar$$
  -     2.2

Nuclei with spin also possess a magnetic moment, $\underline{\mu}$, which defines the torque experienced by the nucleus when it is placed in an external magnetic field. The magnetic moment has the same direction as the angular momentum and the two are related via equation 2.3.

$$\underline{\mu} = \gamma \underline{P}$$
  -     2.3

Where γ is the gyromagnetic or magnetogyric ratio, which is normally a positive constant.

The signals detected in NMR only arise from nuclei with a non-zero spin and the best NMR characteristics tend to be found in nuclei with a spin of ½. Table 2.1 details some of the most important NMR nuclei and lists their gyromagnetic ratio and natural abundance.

Nucleus	Spin Quantum Number	Gyromagnetic Ratio (MHz/T)	Relative Abundance %
^{1}H	1/2	42.58	99.98
^{2}H	1	6.53	0.015
^{13}C	1/2	10.71	1.11
^{14}N	1	3.06	99.6
^{15}N	1/2	-4.30	0.37
^{19}F	1/2	40.05	100
^{23}Na	3/2	11.26	100
^{31}P	1/2	17.23	100
^{39}K	3/2	1.99	93.1
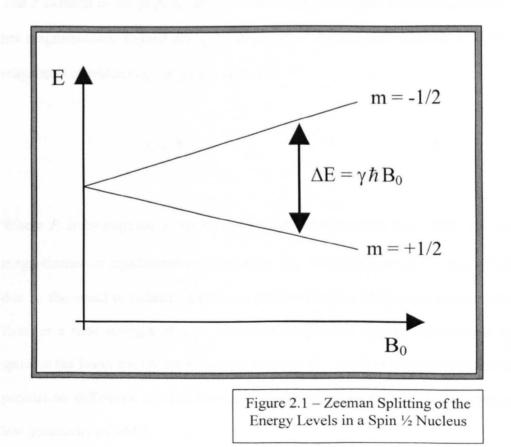
Table 2.1 – Common NMR Nuclei

2.2.2 Zeeman Splitting

When nuclei are placed in an external magnetic field, the nucleus acquires energy as a result of the interaction between the external field and its magnetic moment. The energy acquired is proportional to the magnitude of the external magnetic field and the magnetic moment as shown by equation 2.4.

$$E = -\underline{\mu}.\underline{B} \qquad - \qquad 2.4$$

If we consider the case of a nucleus with a spin of ½ and an external field placed along the z-axis of our Cartesian co-ordinate system, we can see from combining equations 2.2 and 2.3 that the nucleus will have two values of magnetic moment along the direction of the external field ($\pm 1/2 \, \gamma \hbar$) and therefore, according to equation 2.4, two different energy states. These states can be interpreted as nuclei whose spins are aligned parallel and anti-parallel to the magnetic field with the parallel spins having a lower energy. This difference in the energy with the spin state is represented diagrammatically in figure 2.1 and is known as the Zeeman splitting of the nucleus.

Figure 2.1 – Zeeman Splitting of the Energy Levels in a Spin ½ Nucleus

2.2.3   The Boltzmann Distribution

The presence of two energy levels in the spin ½ example means that with a large collection of spins, two energy populations will exist and the relative sizes of the populations can be defined by the Boltzmann distribution as described by equations 2.5 and 2.6.
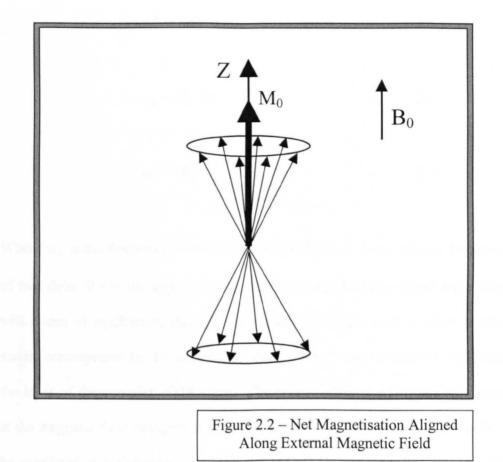
$$N^+ / N^- = e^{-\Delta E / kT} \qquad\qquad - \qquad 2.5$$

$$N^+ / N^- = e^{-\gamma \hbar B_0 / kT} \qquad\qquad - \qquad 2.6$$

Where N^+ and N^- are the populations of the $+$ ½ and $-$ ½ spin states respectively, ΔE is the energy difference, k is the Boltzmann constant and T is the temperature. The difference in the populations of the two spin states leads to the presence of a net magnetisation, aligned along the direction of the external magnetic field, the magnitude of which is given by equation 2.7.

$$M = \sum P_i \mu_i \qquad\qquad - \qquad 2.7$$

Where P_i is the population and μ_i is the magnetic moment of the ith state. The net magnetisation or equilibrium magnetisation, M_0, shown in figure 2.2 is very small due to the small population difference predicted by the Boltzmann distribution. Even at a field strength of 1.5T and room temperature the fractional excess of spins in the lower energy state is of the order of 10^{-5} and it is this relatively small population difference and equilibrium magnetisation that leads to the inherently low sensitivity of NMR.

Figure 2.2 – Net Magnetisation Aligned
Along External Magnetic Field

2.2.4 Induction of Quantum State Transitions

To produce signals in NMR, it is necessary to move the system away from equilibrium, something that can be achieved by raising the system into a higher energy state. The easiest way to accomplish this is to add energy to the system by inducing transitions between the different energy states. These transitions can be induced through the application of an oscillating magnetic field, applied in the x-y plane at the correct frequency. To induce the maximum number of transitions the frequency of the oscillating field should be such that the energy provided to the system is equal to the energy difference between the two states. This is achieved by the solution of equation 2.8.

$$\Delta E = \gamma \hbar B_0 = h \upsilon_0 \qquad - \qquad 2.8$$

$$\upsilon_0 = \gamma B_0 / 2\pi \qquad - \qquad 2.9$$

$$\omega_0 = \gamma B_0 \qquad - \qquad 2.10$$

Where υ_0 is the frequency of the oscillating field and ω_0 is the angular frequency of that field. When the application of the oscillating field is stopped, the system will return to equilibrium through the transition of spins back to their original states, accompanied by the emission of energy, which can be detected and forms the basis of the complex NMR signal. The energy difference between spin states at the magnetic field strengths used in NMR is such that the applied field needs to be oscillated at a frequency that is in the radiofrequency band and as such, the applied field is referred to as the RF field.

2.3   The Classical Approach

2.3.1   Larmor Precession

From a classical point of view, the net magnetisation of the spins in a sample can be pictured as a bar magnet that possesses angular momentum. If a bar magnet is placed in a magnetic field, just as with the needle of a compass, it aligns with the field and the same is true of the magnetisation. However, if the compass needle possessed angular momentum it would also precesses around the field, in the same way that a gyroscope precesses around the earth's gravitational field. This leads us to a picture of the net magnetisation that is aligned with the

externally applied magnetic field, B_0, and which precesses around the field at a rate that is proportional to the applied magnetic field. The constant of proportionality is the gyromagnetic ratio, γ, and shows us that the rate, or angular frequency, of the precession is the same as that given by equation 2.10 to describe the angular frequency of the RF field needed to induce transitions between spin states. The precession of spins about the external field is known as Larmor precession and the rate of the precession, ω_0, is known as the Larmor frequency.
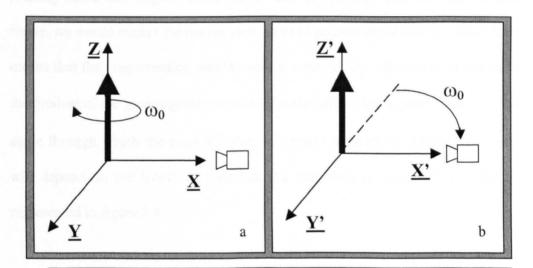
Figure 2.3a – Laboratory Frame of Reference. A Stationary Camera Along the X-Axis Would See Magnetisation Precessing About the Z-Axis with an Angular Frequency, ω_0

Figure 2.3b – Rotating Frame of Reference. The Camera Rotating in the XY-Plane at an Angular Frequency, ω_0, Would See Stationary Magnetisation Along the Z-Axis

2.3.2   The Rotating Frame

It is possible to simplify the visualisation of the NMR experiment by imagining that the Cartesian co-ordinate system we have set up is not static but instead rotating about the z-axis at the Larmor frequency. This rotation would mean that the precessing magnetisation would appear to be static and aligned along the z-axis of our new frame of reference. The static appearance of the

magnetisation would also imply that the external magnetic field is apparently equal to zero from equation 2.10. This reference frame, referred to as the Rotating Frame, is visualised in figure 2.3 and is represented by the axis x', y' and z', where z' is in fact equivalent to the non-rotating z-axis.
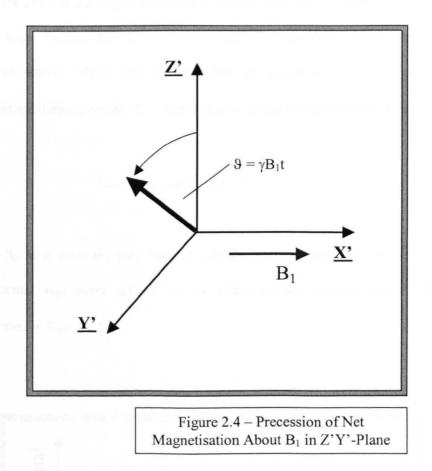
2.3.3 The Application of Radiofrequency Electromagnetic Fields

We now consider the application of a magnetic field, B_1, which is static in the rotating frame and aligned along the x'-axis. By analogy with the non-rotating frame, we would expect the net magnetisation to precess about this new field. This means that the magnetisation would rotate around the z'y'-plane at a rate equal to the product of the gyromagnetic ratio and the strength of the applied field, B_1. The angle through which the magnetisation will rotate is given by equation 2.11 and will depend on the length of time that the new field is applied for, t. This is represented in figure 2.4.

$$\theta = \gamma B_1 t \qquad\qquad - \qquad 2.11$$

The question that arises from this is how do we generate a field that appears to be static along the x'-axis of the rotating frame? The answer comes from returning to the non-rotating frame, where we will see a magnetic field that rotates around the z-axis at a rate equal to the Larmor frequency. The generation of this field is achieved through the application of an electromagnetic field rotating in the xy-plane of the non-rotating frame of reference at the Larmor frequency, exactly equivalent to the result generated from the Quantum mechanical approach to explain the transition of spins between states.

$$\vartheta = \gamma B_1 t$$

Figure 2.4 – Precession of Net Magnetisation About B_1 in Z'Y'-Plane
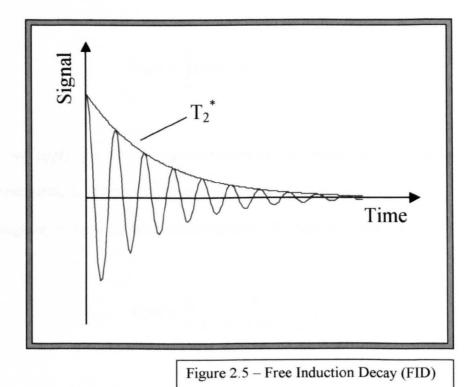
2.3.4   The Free Induction Decay

After the application of a pulse of RF energy sufficient to produce a 90° rotation of the magnetisation, the ensemble of spins will precess coherently, creating a net magnetization that will rotate around in the xy-plane. This rotating magnetisation generates the signals detected in the NMR experiment through the induction of an electromotive force (emf) in a receiver coil. If every spin experienced exactly the same external magnetic field and had exactly the same gyromagnetic ratio, this signal would continue as a simple sinusoid and assuming that the system lost no energy, would carry on forever. However, the external magnetic field is not perfectly homogeneous and each nucleus experiences a slightly different field that leads to a loss of the coherent rotation of the

magnetization. As each spin rotates at a slightly different frequency, a dephasing of the spins occurs and as such the signal they produce decays away. The measured signal, which can be described by equation 2.12, decays with a characteristic time constant, T_2^*, and is known as the Free Induction Decay.

$$Signal = S_0 \cos(\omega_0 t + \phi)e^{-t/T_2^*} \qquad - \qquad 2.12$$

Where S_0 is a constant that depends on the net magnetisation as well as the experimental equipment and ϕ is the phase of the received signal. This is represented in figure 2.5.

Figure 2.5 – Free Induction Decay (FID)

2.3.5 Fourier Transformation of the FID

The interest in NMR comes from the fact that the different components of a sample are all subject to different chemical environments. The chemical environments cause each nucleus to experience slightly different magnetic fields and as such, precess at different frequencies, leading to a complex FID. The change in the frequency for a particular component is referred to as its chemical shift. To obtain information about the components of a sample in spectroscopy, or to provide spatial information in an imaging experiment, it is necessary to break down the signal received into its various frequency components. This is achieved with the use of a Fourier transform.

Fourier transformation allows a time varying signal to be analysed as a function of its frequency components and it can be defined by equation 2.13.
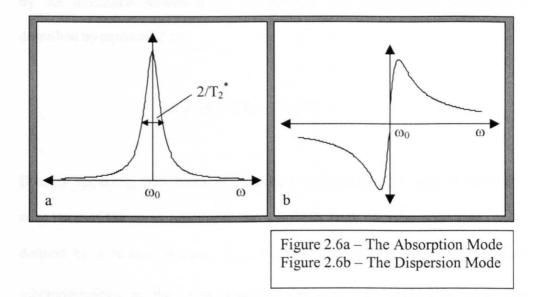
$$F(\omega) = \int_{-\infty}^{\infty} f(t) e^{i\omega t} dt \qquad - \qquad 2.13$$

If we apply the Fourier transformation to the signal obtained in an NMR experiment, as given in equation 2.12 with ϕ equal to zero, we obtain a real and imaginary component described by equations 2.14 and 2.15 respectively.

$$F(\omega) = \frac{S_0}{2} \frac{T_2^*}{1 + (T_2^*)^2 (\omega - \omega_0)^2} \qquad - \qquad 2.14$$

$$F(\omega) = \frac{iS_0}{2} \frac{\omega - \omega_0}{1 + (T_2^*)^2 (\omega - \omega_0)^2} \qquad - \qquad 2.15$$

These are referred to as the absorption and dispersion modes and they are represented in figure 2.6. The two modes can be considered to be the M_X and M_Y components of the magnetisation in the idealised case when the detected phase, ϕ, is zero. In reality the results of the Fourier transform will be a combination of the two modes and the use of phase correction is needed to separate them.

Figure 2.6a – The Absorption Mode
Figure 2.6b – The Dispersion Mode

The lineshape of the absorption mode for this idealised case is a Lorentzian with the Full Width at Half Maximum (FWHM) being proportional to the inverse of the decay time constant, T_2^*.

2.4   NMR Parameters and their Measurement

2.4.1   The Bloch Equations

The unstable, non-equilibrium state that the system is in after the application of a pulse of RF energy leads to the recovery of the system back to equilibrium through relaxation processes. The recovery of the original longitudinal magnetisation, M_o, aligned along the z-axis is brought about by the exchange of

the spins' excess energy with their surroundings or 'lattice'. Hence the recovery of the longitudinal magnetisation is also termed spin-lattice relaxation. The recovery back to equilibrium is brought about by the transition of spins from the higher to the lower energy state, a process that would occur spontaneously but only over a very long period of time. This process is accelerated primarily through dipolar interactions between spins leading to stimulated transitions that are caused by the molecular movement in the sample. The longitudinal relaxation is described by equation 2.16.

$$dM_z / dt = (M_0 - M_z)/T_1 \qquad - \qquad 2.16$$

Broadly speaking, two types of processes bring about the loss of transverse coherence of the spins rotating in the xy-plane. Each of these processes can be defined by a relaxation time; T_{2inh}, related to the presence of constant field inhomogeneities in the main magnetic field and, T_2, related to static and oscillating magnetic fields generated by neighbouring magnetic moments. The T_{2inh} processes are primarily dependant on the experimental system and T_2 processes are sample specific. Equation 2.17 shows how these two times can be combined to give the T_2^* relaxation time defined in equation 2.12.

$$1/T_2^* = 1/T_{2inh} + 1/T_2 \qquad - \qquad 2.17$$

The loss of coherence caused by static inhomogeneities in the main magnetic field is a reversible process, and this allows the relaxation of the transverse

magnetisation caused by the sample, T_2, to be measured. T_2 is described by the phenomenological equations 2.18 and 2.19 and is termed the transverse or spin-spin relaxation.

$$\blacksquare \qquad - \qquad 2.18$$

$$\blacksquare \qquad - \qquad 2.19$$

Equations 2.16, 2.18 and 2.19 can be grouped together and termed the Bloch equations. The processes that cause the longitudinal and the transverse relaxation of the system are covered in more detail in the following sections along with descriptions of experimental methods that can be applied to measure their relevant relaxation times.

2.4.2   Longitudinal (Spin-Lattice) Relaxation

Both longitudinal and transverse relaxations are brought about through the interaction of spins with their surrounding environment. Various types of interaction are responsible for the recovery back to equilibrium and the magnitude of the interactions is determined to a large extent by the motions of the nearby molecules. Two regimes can be considered; one where the molecular motion is rapid as it is in the liquid state and one where the motions are relatively slow as in the solid state. In biological examples we shall be mainly interested in the rapid regime, but the presence of large proteins and macromolecules does provide an environment where slow motions are present and therefore must be considered. Of all the interactions involved in relaxation processes, the most important is that

generated by neighbouring spins, termed the dipole-dipole interaction. Spins can be imagined as magnetic dipoles that are surrounded by other dipoles, which are tumbling and generating varying magnetic fields. These magnetic fields are a major source of relaxation.

As mentioned in the previous section, longitudinal relaxation is accelerated by the stimulated transmission of spins from the upper to the lower energy state and the subsequent transmission of energy to the surrounding lattice. To stimulate a transition the spin must be subjected to a magnetic field that is varying at, or around, the Larmor frequency. In the regime where molecular motion is relatively rapid, the surrounding spins are tumbling and generating fields at a wide range of frequencies. The distribution of frequencies produced is related to the spectral density, $J(\omega)$, which for most cases can be expressed in the form of equation 2.20, as a function of τ_c, the correlation time that describes the rate of the molecular motions.

$$J(\omega) = \tau_c / (1 + \omega^2 \tau_c^2) \qquad - \qquad 2.20$$

The rate of longitudinal relaxation will depend on the magnitude of the fields generated in the xy-plane by the dipole-dipole interactions, B_{XY}, and by the spectral density at the Larmor frequency, $J(\omega_0)$. It is then possible to write a simplified expression for the rate of relaxation as shown in equation 2.21.

$$1/T_1 \propto B_{XY}^2 \tau_c / (1 + \omega_0^2 \tau_c^2) \qquad - \qquad 2.21$$

From this expression, we can see that the rate of longitudinal relaxation will be maximised when the time scale of the molecular motion is such that $\omega_0 \tau_c$ is unity, i.e. when $1/\tau_c = \omega_0$, equivalent to molecular motions at the Larmor frequency.

2.4.3   Transverse (Spin-Spin) Relaxation

In the case of transverse relaxation, energy is not transferred to the lattice but coherence between the spins is lost through the presence of a range of magnetic field strengths and therefore a range of precessional frequencies. The size of the magnetic field experienced by a spin is not simply determined by the main magnetic field but also by the orientation of surrounding spins via the dipole-dipole interaction. In a sample with slow molecular motions, each spin will experience different magnetic fields due to the unique orientation it has with respect to its neighbouring dipoles. As such, each spin will precess at a slightly different frequency and coherence will be lost rapidly. In a sample with rapid molecular motions, the field experienced by a particular dipole will be continually changing. As the time scale of the motions increases, the average field experienced by a particular spin will become more similar to that of its neighbours. This is due to averaging of the dipole-dipole interaction and will lead to a smaller range of precessional frequencies and a decrease in the rate of the transverse relaxation. This means that the rate of transverse relaxation can be related to the coherence time through the expression given in equation 2.22.

$$1/T_2 \propto B_z^2 \tau_c \qquad\qquad - \qquad 2.22$$
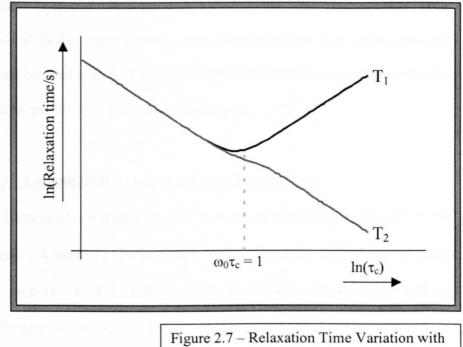
Longitudinal relaxation also has an effect on the transverse relaxation due to the finite lifetime that spins spend in the excited state, leading to an uncertainty in their precessional frequency. This uncertainty can be visualised as a broadening in the range of frequencies present and therefore a loss of coherence. It is this fact that means that all processes causing longitudinal relaxation will also contribute to transverse relaxation and as such it is not possible for the transverse relaxation time to be longer than the longitudinal.

2.4.4   Further Relaxation Theory

From this brief summary of the dipole-dipole interactions, it can be seen that slow molecular motions are responsible for transverse relaxation and motions at the Larmor frequency are related to both longitudinal and transverse relaxation. However, motions at twice the Larmor frequency must also be considered because they can lead to simultaneous transition of both spins involved in the dipole-dipole interaction. This will obviously lead to a shortening of the longitudinal relaxation time and will also lead to a decrease in the transverse relaxation time through the processes mentioned in the previous section. When all the aspects of the dipole-dipole interaction are combined, it is possible to write down expressions for the relaxation times that should be expected in a sample of pure water due to the dipole-dipole interaction between the two protons on each molecule, whilst ignoring interactions between different molecules. These expressions are quoted in equations 2.23 and 2.24, as a function of the correlation time and the distance between the spins, r.

$$1/T_1 = \frac{3}{10} \frac{\gamma^4 \hbar^2}{r^6} \left(\frac{\tau_c}{1 + \omega_0^2 \tau_c^2} + \frac{4\tau_c}{1 + 4\omega_0^2 \tau_c^2} \right) \qquad - \qquad 2.23$$

$$1/T_2 = \frac{3}{20} \frac{\gamma^4 \hbar^2}{r^6} \left(3\tau_c + \frac{5\tau_c}{1 + \omega_0^2 \tau_c^2} + \frac{2\tau_c}{1 + 4\omega_0^2 \tau_c^2} \right) \qquad - \qquad 2.24$$

Figure 2.7 – Relaxation Time Variation with Correlation Time for a Sample of Pure Water
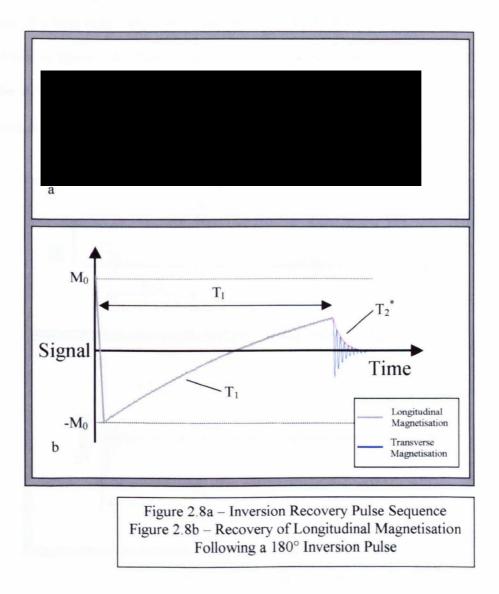
Figure 2.7 shows a sketch of equations 2.23 and 2.24 as a function of correlation time and provides a good summary of the theory that has been covered so far. It can be seen that the longitudinal relaxation is maximised when the frequency of the molecular motions is approximately equal to the Larmor frequency. It can also be seen that when molecular motions are slow (relating to high values of τ_c) the transverse relaxation time is very short and far removed from the longitudinal relaxation time. However, when molecular motions are very fast, leading to

averaging of the dipole-dipole interaction, the transverse relaxation time is long and approximately equal to the longitudinal relaxation.

It is found in biological samples that the relaxation times are shorter than those predicted by this theory and transverse relaxation is generally much more rapid than longitudinal relaxation. This is because the situation is more complex than that presented due to the presence of large proteins and macromolecules that tend to slow molecular motions and paramagnetic ions that generate very large localised fields. There are also many other processes that lead to relaxation that are not covered here, including the chemical shift anisotropy, scalar coupling, spin rotation and electric quadrupole interactions.

2.4.5   Longitudinal Relaxation Time Measurement

There are several experimental methods of measuring T_1, one of which is the Inversion Recovery pulse sequence. The sequence consists of two RF pulses, one that produces a 180° rotation of the equilibrium magnetization and one that produces a 90° rotation. These two pulses are separated in time by a period T_I, as shown in figure 2.8. The 180° pulse is also known as an inversion pulse because it inverts the magnetization with respect to the main magnetic field so that it lies parallel to the –z-axis. During the time between this inversion pulse and the subsequent 90°, or excitation, pulse the magnetisation will recover back to equilibrium exponentially following the Bloch equation that governs longitudinal relaxation, equation 2.16. The subsequent excitation pulse rotates the longitudinal magnetisation into the transverse plane and the magnitude of the signal is recorded yielding a measure of the longitudinal magnetisation at the time the excitation pulse was applied. This process is repeated, after a sufficiently long time to allow
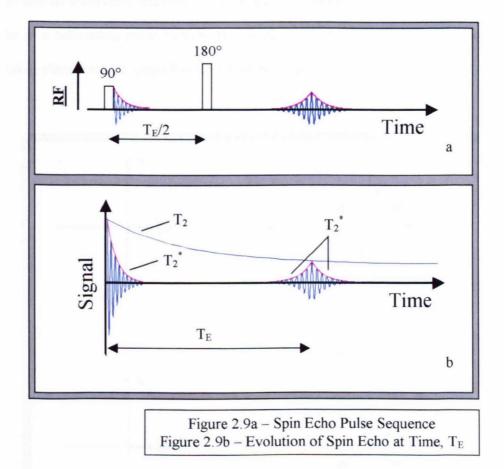
the longitudinal magnetisation to recover fully ($\sim 5T_1$), for a range of different interval times, T_I.

Figure 2.8a – Inversion Recovery Pulse Sequence
Figure 2.8b – Recovery of Longitudinal Magnetisation
Following a 180° Inversion Pulse

The resulting intensities are then used to fit for T_1 in equation 2.25, which is the solution to the Bloch equation for the recovery of the longitudinal magnetisation after the application of an inversion pulse.

2.25

2.4.6   Spin Echoes and Transverse Relaxation Time Measurement
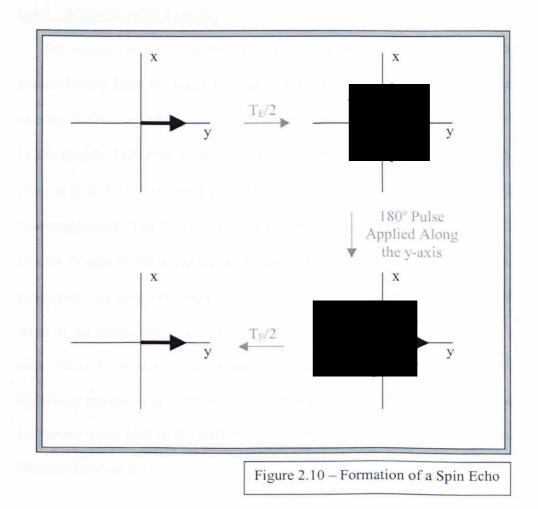
The measurement of the transverse relaxation time, T_2, is achieved with the use of a spin echo, which is formed by a $90°$-$T_E/2$-$180°$-$T_E/2$ pulse sequence as shown in figure 2.9a. The spin echo sequence generates the expected signal after the $90°$ pulse, but also generates a second signal that appears as two FIDs back to back at a time T_E (figure 2.9b).

Figure 2.9a – Spin Echo Pulse Sequence
Figure 2.9b – Evolution of Spin Echo at Time, T_E

If the $90°$ pulse is applied along the x-axis, the effect will be to rotate the spins in the y-z plane until they are aligned along the y-axis, where the natural loss of coherence through T_2^* mechanisms will cause the spins to dephase rapidly. A $180°$ pulse that is applied along the y-axis will rotate the spins through $180°$ in the x-z plane. The inverted spins will then continue to precess as before but now they

will begin to realign themselves, creating an echo as shown in figure 2.10. The formation of a spin echo will refocus any loss of coherence that is caused by magnetic field variations that have been static in time during the course of the experiment. Any relaxation that is caused by time varying field gradients will not be refocused. As such, the effect of the spin echo sequence is to generate an echo that has removed the effect of any inhomogeneities in the static field but has not overcome transverse relaxation effects. The 180° pulse in this sequence is referred to as a refocusing pulse because it is used to refocus the loss of coherence that takes place through reversible relaxation processes.

Figure 2.10 – Formation of a Spin Echo
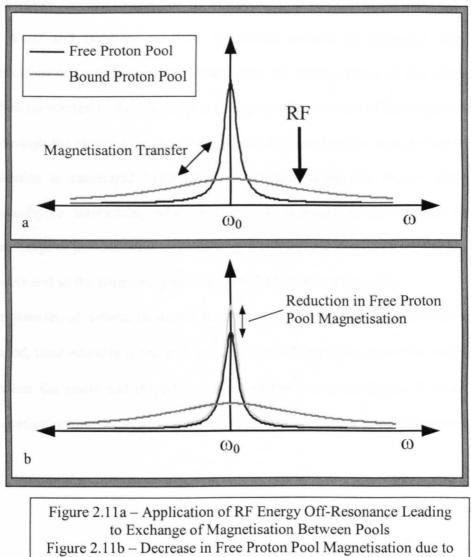
The spin echo's amplitude is governed by the transverse Bloch equations, described by equations 2.18 and 2.19, and a measurement of the transverse relaxation time can be made by the measurement of the amplitude of a spin echo at a series of different echo times T_E. The signal amplitude measured from these spin echoes is then used to fit for T_2 in equation 2.26, which is the solution of the transverse Bloch equations for this pulse sequence.

$$\blacksquare \qquad - \qquad 2.26$$

2.4.7   Magnetisation Transfer

The signals used in the production of magnetic resonance images come predominately from the water protons within the sample being imaged. There is also a contribution to the signal from the protons contained within any fat present in the sample. However, most biological samples contain many other sources of protons that do not contribute to the signal, such as bound water and protein macromolecules. The reason for these protons failing to have any effect on the images is due to the rapid decay of their signal through transverse relaxation processes. The transverse relaxation time of these 'bound' protons is so short that there is no measurable signal remaining at the time of image acquisition. The transverse relaxation time of free water is of the order of 0.5-2 seconds, whereas for bound protons it is on the microsecond scale. These differences in transverse relaxation times lead to the differences in the line shapes of the different proton species shown in figure 2.11a.

Figure 2.11a – Application of RF Energy Off-Resonance Leading to Exchange of Magnetisation Between Pools
Figure 2.11b – Decrease in Free Proton Pool Magnetisation due to Magnetisation Transfer

The narrow line shape of the free water protons reveals the relatively large effect that RF energy applied at, or close to, the Larmor frequency has on the equilibrium magnetisation compared with the effect it has on the bound protons. However, the application of a RF magnetic field at a frequency removed from the resonance position will have a negligible effect on the free protons, but can still cause a perturbation of the bound protons away from their equilibrium state. This

off-resonance behaviour can be utilised to allow the bound proton pool to be investigated through imaging of the free protons. In an experiment first suggested by Wolff and Balaban[3] in 1989, the bound protons are saturated with the application of continuous wave off-resonance RF energy. Some of this saturation is then transferred to the free protons through cross relaxation of the magnetisation or through the chemical exchange of protons. Cross relaxation is a process where saturation is transferred from the bound protons to the free protons due to a dipole-dipole interaction, whereas chemical exchange is due to the actual interchange of protons between molecules. Chemical exchange is a relatively slow process and so the dominating exchange method is cross relaxation.

The transfer of saturation means that when the free protons are subsequently imaged, their intensity is reduced by an amount related to the rate of the exchange between the pools and the relative sizes of the two pools (figure 2.11b). The magnetisation transfer experiment is covered in much greater detail in section 8.1.

References

[1] Grant, D.M. and R.K. Harris, *Encyclopedia of Nuclear Magnetic Resonance*. 1995: John Wiley.

[2] Callaghan, P.T., *Principles of Nuclear Magnetic Resonance Microscopy*. 1991: Clarendon Press. 492.

[3] Gadian, D.G., *NMR and its Applications to Living Systems*. 2nd ed. 1995: Oxford University Press. 283.

[4] Harris, R.K., *Nuclear Magnetic Resonance Spectroscopy*. 1986: Longman Scientific & Technical. 260.

[5] Mansfield, P. and I.L. Pykett, *Biological and Medical Imaging by NMR*. Journal of Magnetic Resonance, 1978. **29**: p. 355-373.

[6] Mansfield, P. and P.G. Morris, *NMR Imaging in Biomedicine*. 1982: New York Academic Press. 354.

[7] Marciani, L., *EPI of Gastric Function: The Effects of Physical Factors in Food - Ph.D. Thesis*, in *School of Physics and Astronomy*. 2001, Nottingham: Nottingham.

[8] Morris, P.G., *Nuclear Magnetic Resonance Imaging in Medicine and Biology*. 1986: Oxford : Clarendon. 320.

[9] Rinck, P.A., *Magnetic Resonance in Medicine : The Basic Textbook of the European Magnetic Resonance Forum*. 3rd ed. 1993: Blackwell Scientific Publications. 241.

[10] Stark, D.D. and W.G. Bradley, *Magnetic Resonance Imaging*. 3rd ed. 1999: Mosby International.

3   Theory of Magnetic Resonance Imaging (MRI)

3.1   An Historical Overview

To expand the phenomenon of NMR into an imaging modality, it is necessary to encode spatial information into the acquired signal. In 1951, Gabillard showed that the Fourier transform of the FID observed from a tube of water placed in a linearly varying magnetic field gradient produced a projection of the proton spin density. He used the technique to yield a measure of gradient strength but apparently did not realise that it could be used to produce images. It took until 1973 for MRI to be finally introduced by two groups working independently on either side of the Atlantic. Mansfield and Grannell, working at the University of Nottingham proposed a technique involving Fourier transformation of a signal recorded in the presence of a magnetic field gradient. At the same time, Lauterbur, working at Stonybrook University, used a rotating magnetic field gradient to produce a two-dimensional image that gave rise to the first published MR image of two tubes of water.

After this, the field of MRI expanded rapidly with new techniques being constantly introduced to provide better and faster image acquisition schemes. Kumar and colleagues proposed a technique in 1975 called 'Fourier Zeugmatography' that required the use of a two-dimensional Fourier transform for image reconstruction. This was followed by a technique called Field fOcused Nuclear mAgnetic Resonance (FONAR) established by Damadian in 1977. FONAR imaging required the sample to be physically moved through a small resonance aperture whilst signals were constantly acquired. In 1980, a group from Aberdeen University led by Edelstein, made some modifications to the Fourier Zeugmatography technique to design a new image acquisition scheme that they

named 'Spin Warp Imaging'. This was followed in 1981 by the publication of the first image to be produced by a technique called 'Echo Planar Imaging' (EPI). Mansfield had originally proposed EPI in 1977 but the exceptional demands that the acquisition scheme placed on the experimental hardware meant that its development was slow. The EPI scheme was unique because it allowed the production of images in a very short amount of time from a single FID[1].

Since the invention of EPI many new fast imaging techniques have been proposed but none can match its acquisition speed. However, EPI does suffer from several problems brought about by its fast acquisition. The need for high performance hardware places extra demands on the scanner and echo planar images suffer from image artefacts and an inherently low signal to noise ratio. The following sections introduce the theory behind the original magnetic resonance imaging schemes leading up to the invention of EPI. The final section describes some of the problems with echo planar image acquisition and methods of overcoming them.

3.2   Image Formation Theory

3.2.1   The Effect of a Magnetic Field Gradient

It is possible to encode spatial information in the NMR signal with the use of a linearly varying magnetic field. Equation 3.1 describes a magnetic field gradient that is superimposed on the static magnetic field of an NMR system such that the magnetic field strength varies linearly along the z-axis of the magnet.

$$B(z) = B_0 + G_z z$$
$$-\qquad 3.1$$

Where B_0 is the static field strength along the z-axis and G_z is the gradient strength, in units of T/m, in a direction parallel to the static field. Equation 2.10 states that the resonance frequency is proportional to the magnetic field strength and it is possible to rewrite equation 3.1 to take account of this to generate equation 3.2.

$$\omega(z) = \omega_0 + \gamma G_z z \qquad\qquad - \qquad 3.2$$

This shows that the frequency of precession is now a function of position along the z-axis. To excite all of the spins in this system, it is necessary to apply a pulse of RF energy with a bandwidth large enough to cover the range of frequencies that relates to the size of the sample. Fourier transformation of the signal recorded in the presence of this gradient field will yield a measure of the amplitudes of the frequency components contained in the signal. If relaxation effects are neglected, the result will be a projection of the spin density along the z-axis as shown in figure 3.1. The ability to encode positional information about the spin density in the frequency of the measured signal is known as frequency encoding.

Acquire signal in presence of field gradient

Fourier transform signal to yield projection of spin density

$B_0 - G_z z$ B_0 $B_0 + G_z z$

$\omega_0 - \gamma G_z z$ ω_0 $\omega_0 + \gamma G_z z$
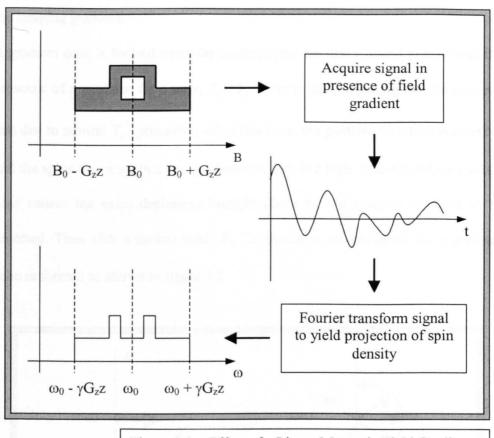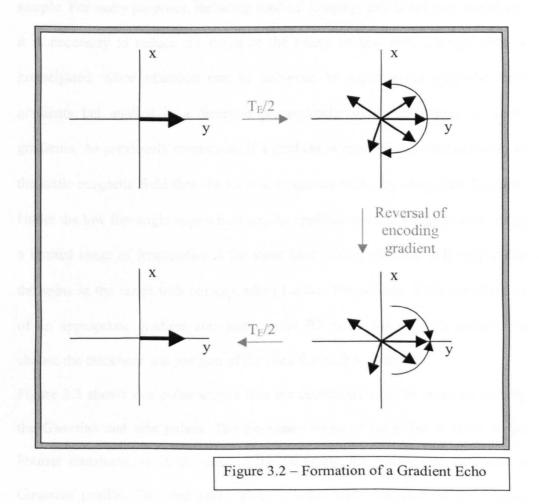
Figure 3.1 – Effect of a Linear Magnetic Field Gradient

3.2.2 Dephasing of Spins and Gradient Echo Formation

It may be possible to provide spatial information with the use of field gradients, but the presence of a variation in the magnetic field drastically reduces the observable signal. After the application of a 90° pulse, the magnetisation vector will lie in the X-Y plane, but the effect of the field gradient is to cause the spins to precess at different frequencies. This variation in the rate of precession will cause the spins to spread out or dephase and the measurable signal to be reduced. Thus the information that the gradients are adding to the signal is lost almost before it can be observed. However, the information can be recovered by

the reformation of the signal as a gradient echo, which is formed by a reversal of the imaging gradient.

A gradient echo is formed when the excited spins are first allowed to evolve in the presence of a gradient for a time, $T_E / 2$, causing spin dephasing that far exceeds that due to natural T_2^* processes. After this time, the gradient direction is inverted and the spins that were in a low gradient are now in a high gradient and vice versa. This causes the extra dephasing brought about by the imaging gradient to be reversed. Thus after a further time, $T_E / 2$, the spins are realigned and a gradient echo is formed as shown in figure 3.2.

Figure 3.2 – Formation of a Gradient Echo

The reversal of the encoding gradient will have no effect on any loss of coherence that has been caused by inhomogeneities in the static field or by time varying gradients. As such, the gradient echo is weighted by the T_2^* value of the sample and increasing the echo time will strengthen this weighting. It is also possible to combine a gradient echo and a spin echo to give a T_2 weighting to the signal.

3.2.3   Slice Selection and RF Pulse Design

If only frequency encoding is used to generate spatial information, any image produced will include the spin density along the gradient direction for the whole sample. For many purposes, including medical imaging, this is not very useful and it is necessary to reduce the range of the image so that only a single slice is investigated. Slice selection can be achieved by again using magnetic field gradients but applied in a direction perpendicular to the frequency or 'read' gradients. As previously mentioned, if a gradient is applied along the direction of the static magnetic field then the Larmor frequency will vary along that direction. Under the low flip-angle approximation, the application of an RF pulse containing a limited range of frequencies at the same time as this gradient, will only excite the spins in the range with corresponding Larmor frequencies. With the selection of an appropriate gradient size and careful RF pulse design, it is possible to choose the thickness and position of the slice that will be imaged.
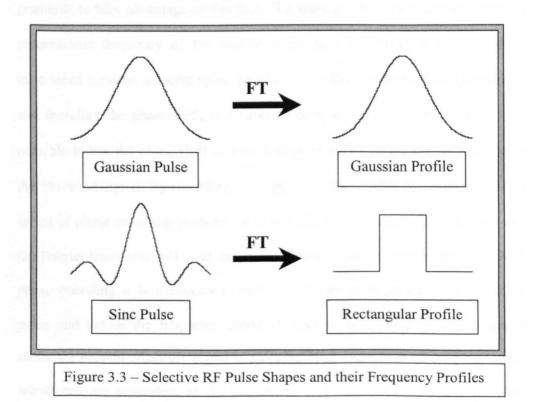
Figure 3.3 shows two pulse shapes that are commonly used in imaging, namely the Gaussian and sinc pulses. The frequency range of the pulse is given by its Fourier transform, so in the case of the Gaussian, the frequencies vary with a Gaussian profile. The sinc pulse gives a better slice selection as the Fourier

transform of the sinc pulse gives a function with a rectangular profile with a width described by equation 3.3.

$$\Delta v = 1/\tau \qquad\qquad - \qquad 3.3$$

Where τ is the time between the maximum of the sinc pulse and the first minimum. The rectangular profile means that the selected frequencies within the profile will be tipped through a uniform angle and any frequencies outside this range will not be excited. However, even under the low flip-angle approximation, the sinc pulse only provides a perfect rectangular profile if the pulse is infinitely long. For practical reasons the pulse has to be truncated and as such there is a rounding of the rectangular edges of the profile.

Figure 3.3 – Selective RF Pulse Shapes and their Frequency Profiles

During most RF pulses applied with magnetic field gradients to select the slice for imaging, the spins are dephased. To overcome this, the direction of the slice selective gradient is reversed after the RF pulse has been applied. To fully reverse the dephasing, it is necessary to apply the slice refocusing gradient with the same amplitude but for only half the length of the slice selection gradient.

3.2.4   Phase Encoding

To obtain a useful image, it is necessary to select an appropriate slice and spatially encode in more than one dimension. Encoding of the second dimension can be achieved with the use of phase encoding. In the NMR signal received from a sample, phase information is preserved as well as the amplitude. Phase encoding uses the application of gradients perpendicular to the slice and frequency encoding gradients to take advantage of this fact. The application of a gradient changes the precessional frequency of the sample spins, thus over time a phase shift is introduced between adjacent spins. Due to the fact that the precessional frequency, and therefore the phase shift, is a function of position within the gradient, it is possible to use the phase shift as a method of encoding positional information in the observed signal. By recording the signals produced after the application of a series of phase encoding gradients, it is possible to manipulate the data such that the Fourier transform will yield the proton density along the phase direction. With phase encoding it is necessary to apply the phase gradient after the excitation pulse and before the frequency encoding gradient is applied so that the phase shifts are present when the signal is recorded. The magnitude of the phase shifts introduced are dependent on the amplitudes and lengths of the phase encoding gradients. It is common to keep the time of the gradient pulse constant and

incrementally increase the amplitude so as to prevent any variation in the different signals recorded due to dephasing caused by field inhomogeneities. The number of pixels required in the phase direction determines the number of phase encoding steps that are needed.

3.2.5 k-Space Theory

The theory behind frequency and phase encoding is the same and can be explained by the use of reciprocal lattice space. The use of a reciprocal space wave vector, k, analogous to that used in optics to describe a plane wave, can be introduced by giving consideration to the evolution of the magnetisation vector in the presence of a field gradient. If we first consider the one-dimensional case of a sample with spin density, $\rho(x)$, in the rotating frame, it is possible to describe the FID, neglecting relaxation effects, using equation 3.4.

$$S(t) = \int \rho(x) e^{i\gamma x \int_0^t G_x(t')dt'} dx \qquad - \qquad 3.4$$

By defining the reciprocal space wave vector, k_x, as shown in equation 3.5.

$$k_x = \gamma \int_0^t G_x(t')dt' \qquad - \qquad 3.5$$

The measured FID signal can be written in terms of the reciprocal space wave vector in the form of equation 3.6.

$$S(k_x) = \int \rho(x)e^{ik_x x}dx \qquad - \qquad 3.6$$

This shows that the proton density along the x-direction is simply the Fourier transform of the FID in reciprocal space, where the reciprocal space wave vector is proportional to the integral of the applied gradient field.
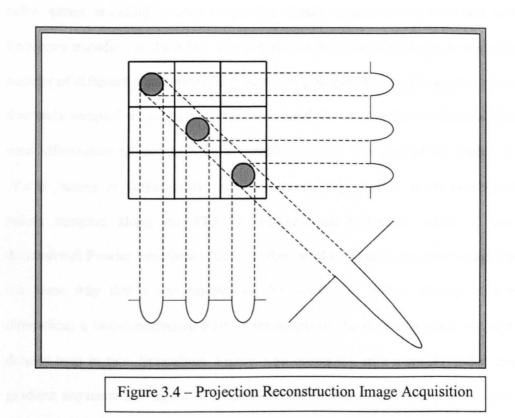
The use of k-space is a convenient way to explain the mathematics of frequency encoding and phase encoding. If the signal is measured in a particular direction, i, at a series of different values of the wave vector, k_i, then a simple Fourier transformation will provide a projection of the proton density along that direction. In the case of frequency encoding, the variation in wave vector values is produced along the gradient direction for each application, whereas the phase encoding data is built up over a series of gradient applications.

3.3 Image Acquisition Techniques

3.3.1 Projection Reconstruction

Projection reconstruction, or back projection, is one of the simplest image acquisition schemes because it only requires the use of frequency encoding. The technique involves the repeated measurement of an FID in the presence of a gradient that is successively rotated in the image plane. The image is produced by projecting the Fourier transformed signals back along the different gradient directions in a method similar to that used in computed tomography (CT) scans. A simple demonstration of the technique applied to three bottles of water is shown in figure 3.4.

Figure 3.4 – Projection Reconstruction Image Acquisition

To obtain an accurate reconstruction of the sample it is necessary to apply gradients in many different directions. The gradients should be applied along axes between 0° and 180° around the sample and separated by 1° or 2° to provide an acceptable image. It is not necessary to apply gradients in the directions between 180° and 360°, as they would simply provide repetitions of the results already obtained. An advantage with the projection reconstruction technique is that, because there is no phase encoding gradient, the acquisition time is short and it is therefore useful when the sample has a very short T_2 value.

3.3.2   Spin Warp Imaging

Spin warp imaging is a technique that requires the application of three gradients in mutually perpendicular directions to provide slice selection and the production of a two dimensional image. After the application of a slice selective

pulse, phase encoding is used to provide details in one spatial direction and frequency encoding in the other. The sequence consists of signal acquisition at a number of different phase encoding gradient amplitudes. The signals produced are discretely sampled to produce a two-dimensional data matrix that contains all the time information needed to form a complete image. The size of the matrix is $N \times M$, where N is the number of phase encode steps and M is the number of points sampled along the FID. A mathematical technique called a two-dimensional Fourier transform (2DFT) is then used to recreate the final image. In the same way that a one-dimensional FT yields the proton density in one dimension, a two-dimensional Fourier transform of the data will yield a proton density map in two dimensions. Figure 3.5a shows the spin warp RF pulse and gradient sequence and figure 3.5b shows the route that this data acquisition will take through k-space.

3.3.3   Echo Planar Imaging

Echo Planar Imaging (EPI) is a technique that allows the production of a complete image from only one FID. The EPI sequence consists of a single RF excitation pulse with slice selection gradient, followed by a large and rapidly switched gradient that causes the formation of a series of gradient echoes. The switched gradient not only causes the formation of gradient echoes but also results in frequency encoding in the applied direction, perpendicular to the slice selection direction. At the same time as the switched gradient, there is a constant but smaller magnitude gradient in a direction perpendicular to the slice selection and switched gradients. This third gradient provides each gradient echo with a different amount of phase encoding, similar to the repeatedly produced FIDs in

Spin Warp imaging. Thus the recorded signal from the echo chain can be put into a k-space matrix and Fourier transformed to produce a 2D image.
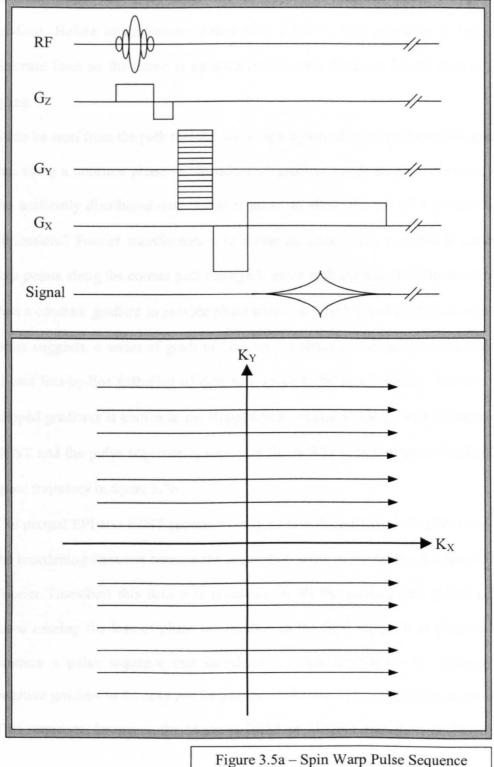
Figure 3.5a – Spin Warp Pulse Sequence
Figure 3.5b – Spin Warp k-Space Trajectory

The EPI sequence is shown in figure 3.6a and the trajectory through k-space

The EPI sequence is shown in figure 3.6a and the trajectory through k-space caused by the gradients is shown in figure 3.6b. The alternately switching read gradient means that every other line in k-space is recorded under a negative gradient. Before image reconstruction with a 2DFT, it is necessary to reverse alternate lines so the phase is encoded in the same direction for all lines of k-space.

It can be seen from the path that the evolving magnetisation takes through k-space that using a constant phase or 'Broadening' gradient yields an approximation to the uniformly distributed data points required to allow the use of a simple two dimensional Fourier transformation to create an image. It is possible to collect data points along the correct path through k-space with the use of a blipped rather than a constant gradient to provide phase encoding. The blipped gradient is, as the name suggests, a series of gradient blips in the phase encoding direction, which allows line-by-line gathering of data in k-space to be accomplished. The use of blipped gradients is known as the Blipped Echo-planar Single-pulse Technique or BEST and the pulse sequence is shown in figure 3.7a with the corresponding k-space trajectory in figure 3.7b.

The normal EPI and BEST sequences only sample the positive half of k-space in the broadening direction because the acquisition starts in the centre of k-space. To Fourier Transform this data it is necessary to fill the missing data points with zeros causing the loss of phase information in the final image. It is possible to produce a pulse sequence that samples the whole of k-space by applying a negative gradient in the read and broadening directions before the data is acquired. This sequence, known as the Modulus BEST or MBEST sequence, is shown in

figure 3.8a and causes the k-space trajectory shown in figure 3.8b. The subsequent data recorded will yield an image that is perfectly resolved in both directions.
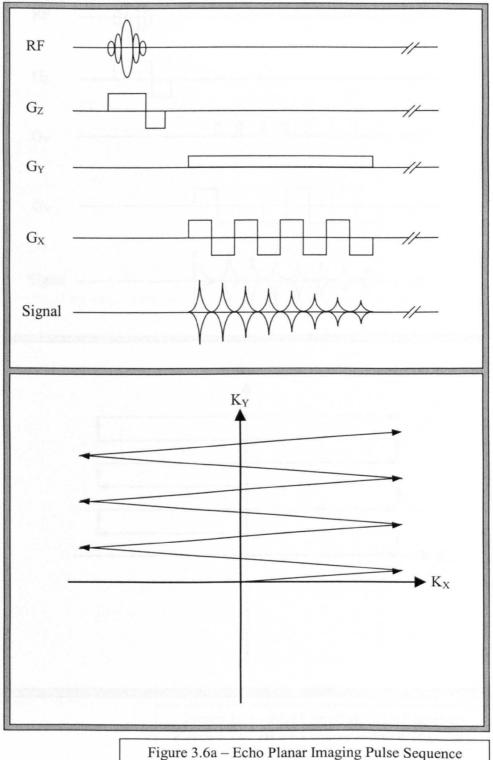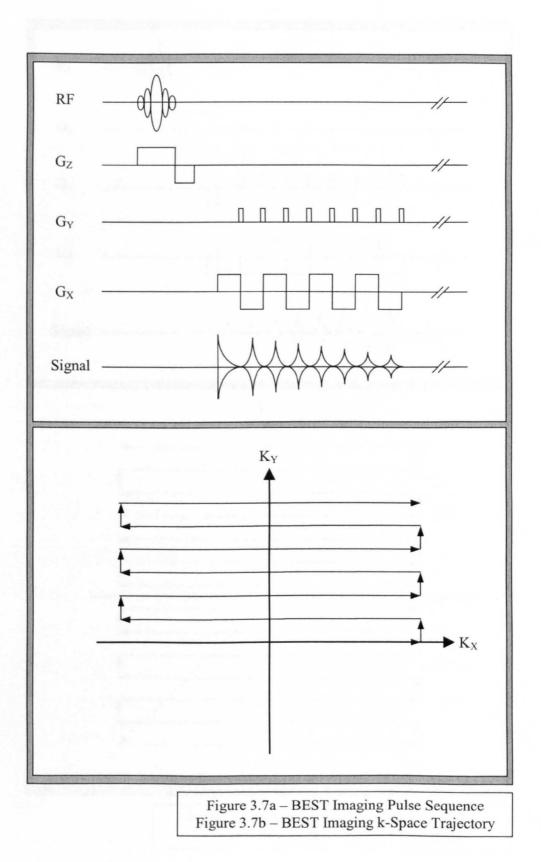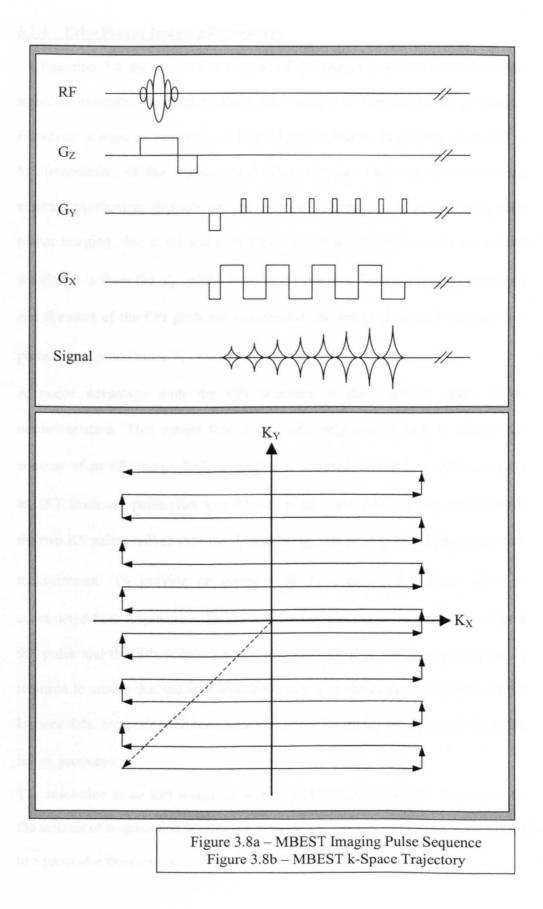
Figure 3.6a – Echo Planar Imaging Pulse Sequence
Figure 3.6b – Echo Planar Imaging k-Space Trajectory

Figure 3.7a – BEST Imaging Pulse Sequence
Figure 3.7b – BEST Imaging k-Space Trajectory

RF

G_Z

G_Y

G_X

Signal

K_Y

K_X

Figure 3.8a – MBEST Imaging Pulse Sequence
Figure 3.8b – MBEST k-Space Trajectory

3.3.4   Echo Planar Imaging Parameters

Equation 3.4 shows that the contrast of the images produced from the NMR signal is naturally weighted by the proton density of the sample being imaged. However, it must be remembered that relaxation effects have been neglected in the formulation of this equation and when they are included, the dominating contrast mechanism depends on the method of image production. With echo planar imaging, due to the image being formed from gradient echoes, the natural weighting is from the T_2^* of the sample. As the time between the RF excitation and the start of the EPI gradients is extended, the image produced becomes less proton density and more T_2^* weighted.

A major advantage with the EPI sequence is the modular nature of its implementation. This means that it is a relatively simple task to change the contrast of an EPI image. If T_1 weighting is required, then it is possible to apply an 180° inversion pulse prior to a 90°-EPI acquisition. Altering the time between the two RF pulses will change the T_1 weighting, just as with an inversion recovery measurement. To provide an image with T_2 contrast, the image must be constructed from a spin echo. This is achieved by placing an 180° pulse between a 90° pulse and the EPI acquisition. Careful placement of the refocusing pulse is required to ensure that the spin echo coincides with the acquisition of the central k-space data. Increasing the echo time will allow for increased T_2 weighting in the image produced.

The resolution in an EPI image, as with any 2DFT type image, is determined by the amount of k-space that is sampled. Equation 3.7 describes the image resolution in a particular direction, x.

$$\Delta x = 2\pi \, / \, k_{x\,MAX} \qquad\qquad - \qquad 3.7$$

Where $k_{x\,MAX}$ describes the maximum value of k_x that is sampled in the given direction, which is determined by the gradient magnitude and duration. This leads to the observation that sampling the high k-space values adds fine detail to the image, whereas the central k-space region provides gross contrast.

Equation 3.8 shows that the distance between adjacent k-space samples determines the field of view, FOV.

$$FOV_x \propto 1 \, / \, \Delta k_x \qquad\qquad - \qquad 3.8$$

This implies that to increase the field of view for a given resolution, the number of samples must be increased in the particular dimension. This can create the situation where the image acquisition time, the resolution and the FOV need to be balanced to find the optimum acquisition for a particular application.

3.3.5 Echo Planar Imaging Artefacts

The use of EPI in any of its various forms is the ideal way to produce a two or even three-dimensional image from a single excitation. However, the technique is not without its problems. Especially when trying to produce a switched gradient of sufficient magnitude to cover a large area of k-space to give good spatial resolution. The rapid switching of such large gradients can cause considerable problems with hardware design. It is necessary to use low inductance coils and the limitations of the power supply voltage and the finite coil inductance tend to

restrict image dimensions to 128×128 pixels. It is common to use sinusoidal or trapezoidal shaped gradient waveforms to try to reduce the demands on the hardware. This necessitates the use of non-linear sampling to produce the k-space data matrix that allows the use of a simple 2DFT for image reconstruction.

If there is any difference in the sampling time between alternate lines an image artefact can be created that appears as a second image that is shifted by half the field of view in the phase encode direction. This artefact is referred to as an N/2 or Nyquist ghost and arises because of the additional periodicity that the uneven sampling creates. It is possible to overcome this artefact by including a pre sample delay (PSD) time in the signal acquisition software. This can then be varied during image acquisition to balance up the alternate lines. Alternatively, this can be achieved in the post processing of the time data.

Another problem with EPI is the large receiver bandwidth needed, typically 128 kHz, which arises from the use of very fast data sampling rates. This necessitates the use of high speed digital to analogue converters, a wide receiver bandwidth and receiver coils with a low Q value, causing a reduction in the achievable Signal to Noise Ratio (SNR). In contrast, the long total sampling time leads to a reduction in the frequency separation between adjacent pixels in the phase encode direction. At 0.5 T the frequency separation is approximately 8 Hz, an order of magnitude lower than in other two dimensional imaging techniques. This causes problems because protons in different chemical environments, fat and water for example, have a different resonant frequency. The difference in the frequencies is called the chemical shift and between fat and water it is 72 Hz at a resonance frequency of 22 MHz. Thus the signal from the fat and water protons in a sample

are shifted by 9 pixels from one another causing a reduction in the quality of the final image, if no fat suppression is applied.

The EPI technique is also very sensitive to inhomogeneities in the static magnetic field as the uniformity of the field governs the T_2^* decay of the FID and hence the number of echoes that can be produced. Inhomogeneities also cause image distortion due to the low frequency separation of adjacent pixels in the phase encode direction. Small imperfections in the static field will cause shifting of the signals along the phase-encoded axis of the final image. These inhomogeneities can arise from imperfections in the static field, the presence of magnetic susceptibility differences between different materials or tissues in the sample and eddy currents generated by the rapidly switched read gradient. The inhomogeneities arising from the static field can be reduced with the use of shim coils and the eddy currents problem can be alleviated with the use of actively shielded gradient coils. Both of these techniques are further described in the next chapter.

The work carried out since its invention has shown that it is possible to overcome these difficulties with improvements in hardware design or suitable post processing of the data. Even when considering the problems inherent in the EPI sequence, it still stands alone as a unique technique for the production of an image in such a short time. The additional advantages of its modular nature and the extremely good contrast between tissue types due to the natural T_2^* attenuation of the signal during acquisition seem to outweigh any problems.

References

[1] Grant, D.M. and R.K. Harris, *Encyclopedia of Nuclear Magnetic Resonance*. 1995: John Wiley.

[2] Bruder, H., et al., *Image-Reconstruction for Echo Planar Imaging with Nonequidistant Kappa-Space Sampling*. Magnetic Resonance in Medicine, 1992. **23**(2): p. 311-323.

[3] Duerk, J.L. and O.P. Simonetti, *Theoretical Aspects of Motion Sensitivity and Compensation in Echo-Planar Imaging*. Jmri-Journal of Magnetic Resonance Imaging, 1991. **1**(6): p. 643-650.

[4] Gadian, D.G., *NMR and its Applications to Living Systems*. 2nd ed. 1995: Oxford University Press. 283.

[5] Gowland, P. and P. Mansfield, *Accurate Measurement of T(1) in-Vivo in Less-Than 3 Seconds Using Echo-Planar Imaging*. Magnetic Resonance in Medicine, 1993. **30**(3): p. 351-354.

[6] Harvey, P.R. and P. Mansfield, *Echo-volumar imaging (EVI) at 0.5 T: First whole-body volunteer studies*. Magnetic Resonance in Medicine, 1996. **35**(1): p. 80-88.

[7] Howseman, A.M., et al., *Improvements in Snap-Shot Nuclear Magnetic-Resonance Imaging*. British Journal of Radiology, 1988. **61**(729): p. 822-828.

[8] Hu, X.P. and T.H. Le, *Artifact reduction in EPI with phase-encoded reference scan*. Magnetic Resonance in Medicine, 1996. **36**(1): p. 166-171.

[9] Ljunggren, S., *A Simple Graphical Representation of Fourier-Based Imaging Methods*. Journal of Magnetic Resonance, 1983. **54**(2): p. 338-343.

[10] Mansfield, P., *Multi-Planar Image Formation Using NMR Spin Echoes*. Journal of Physical Chemistry: Solid State Physics, 1977. **10**: p. L55-L58.

[11] Mansfield, P., R. Coxon, and J. Hykin, *Echo-Volumar Imaging (Evi) of the Brain at 3.0 T - First Normal Volunteer and Functional Imaging Results*. Journal of Computer Assisted Tomography, 1995. **19**(6): p. 847-852.

[12] Mansfield, P., A.M. Howseman, and R.J. Ordidge, *Volumar Imaging Using Nmr Spin Echoes - Echo-Volumar Imaging (Evi) at 0.1-T*. Journal of Physics E-Scientific Instruments, 1989. **22**(5): p. 324-330.

[13] Mansfield, P. and P.G. Morris, *NMR Imaging in Biomedicine*. 1982: New York Academic Press. 354.

[14] Mansfield, P. and I.L. Pykett, *Biological and Medical Imaging by NMR*. Journal of Magnetic Resonance, 1978. **29**: p. 355-373.

[15] Marciani, L., *EPI of Gastric Function: The Effects of Physical Factors in Food - Ph.D. Thesis*, in *School of Physics and Astronomy*. 2001, University of Nottingham.

[16] Morris, P.G., *Nuclear Magnetic Resonance Imaging in Medicine and Biology*. 1986: Oxford : Clarendon. 320.

[17] Ordidge, R.J., et al., *Snapshot Imaging at 0.5-T Using Echo-Planar Techniques*. Magnetic Resonance in Medicine, 1989. **10**(2): p. 227-240.

[18] Posse, S., et al., *High-Speed H-1 Spectroscopic Imaging in Human Brain by Echo- Planar Spatial-Spectral Encoding*. Magnetic Resonance in Medicine, 1995. **33**(1): p. 34-40.

[19] Rinck, P.A., *Magnetic Resonance in Medicine : The Basic Textbook of the European Magnetic Resonance Forum*. 3rd ed. 1993: Blackwell Scientific Publications. 241.

[20] Stark, D.D. and W.G. Bradley, *Magnetic Resonance Imaging*. 3rd ed. 1999: Mosby International.

[21] Stehling, M.K., R. Turner, and P. Mansfield, *Echo-Planar Imaging - Magnetic-Resonance-Imaging in a Fraction of a Second*. Science, 1991. **254**(5028): p. 43-50.

4 Instrumentation
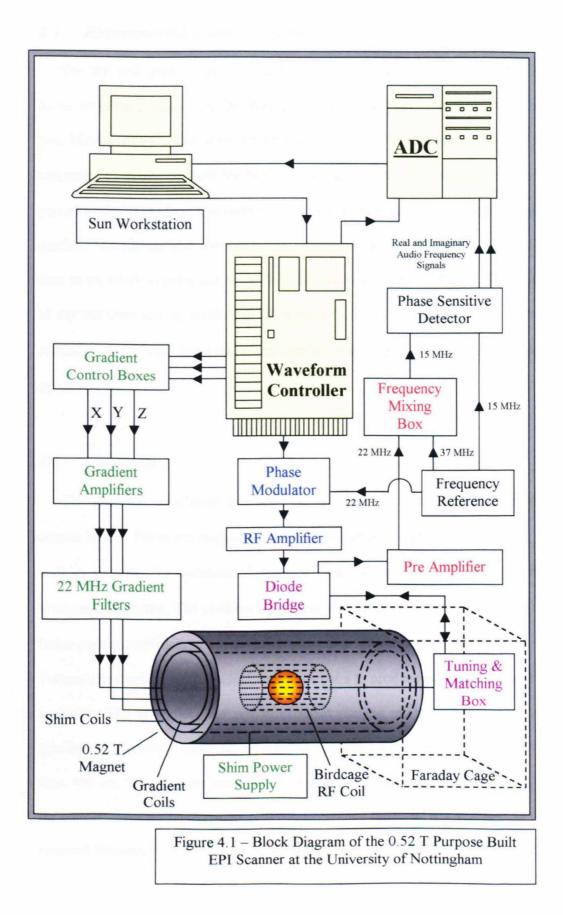
4.1 Introduction

All experimental work described in this thesis was carried out on the 0.5 T purpose built EPI scanner at the University of Nottingham outlined in Figure 4.1. The following sections contain a brief description of the experimental set up and are included for completeness. The author was not responsible for the system's design or construction except for occasional repairs that were required throughout the course of the experimental work described.

4.2 Magnet and Shim Coils

The system is built around a horizontal bore, 0.52 T superconducting magnet (SC050T 105B) supplied by Oxford Magnet Technology Ltd. The magnetic coils are surrounded by liquid Helium, which is in turn encased in a jacket of liquid Nitrogen to limit the cryogen boil-off rate. The proton resonant frequency for the system is 22.03 MHz and the static field homogeneity is quoted as 3 ppm over a 30 cm diameter sphere or 1 ppm over a 1 cm thick slice perpendicular to the field. The homogeneity is obtained with the use of a 13-channel resistive coil shim set, again provided by Oxford Magnet Technology Ltd. The shims are powered by a water-cooled power supply, model 2313, which is capable of providing 10 A per channel. With the shims in place, the magnet has a bore diameter of 90 cm and a total length of 233 cm. To limit the detection of noise caused by stray RF signals in the scanner room, one end of the magnet is enclosed in a Faraday cage, which contains the tuning and matching box and the pre amplifier discussed in sections 4.6 and 4.7. All cables entering the Faraday cage are filtered or shielded to avoid transmission of RF noise into the magnet bore.

Figure 4.1 – Block Diagram of the 0.52 T Purpose Built
EPI Scanner at the University of Nottingham

4.3   Experimental Control System

The RF and gradient pulse sequences are composed and controlled by in-house software produced by Dr. Ron Coxon run on a Sparc Ultra5 workstation, Sun Microsystems[1]. The software provides a flexible platform from which to construct an easily controllable block style experiment. The compiled code is passed to the Waveform Controller (WC), which produces the analogue RF and gradient waveforms and controls the sampling of the received signal. The WC runs as an attached processor to the Sun workstation, relieving the host computer of any run time activity whilst still allowing for 'on-the-fly' variation of sequence variables. The system has a waveform resolution of 1 μs and a sample resolution of 1/16 μs.

4.4   Gradients

The gradient waveforms produced by the WC are passed to the gradient control boxes. These are responsible for the control of the gradient amplifiers, as well as allowing for variation of the slew rate, gain and offset zeroing of the gradient waveforms. The gradient amplifiers are Techron 7790, 3 phase, 115 V linear power amplifiers wired as push pull pairs. The system uses two pairs of Techrons to produce the Z gradient and fours pairs to produce each of the X and Y gradients. The amplifiers are run in constant current mode to ensure that the gradients accurately follow the waveforms supplied, allowing rise times shorter than 400 μs. The gradient current signals are passed through 22 MHz filters as they enter the Faraday cage to prevent any noise entering the scanner at the resonant frequency.

The three orthogonal gradients are produced by a gradient set designed by Prof. Richard Bowtell, as detailed in tables 4.1 and 4.2, which is based on the distributed wire design. This design permits the production of the high amplitude, rapidly switched gradients required for EPI as it provides a coil with a lower inductance and also greater coil efficiency. The gradients are constructed on concentric cylindrical formers that reduce the accessible bore size to 600 mm. The gradient set is actively shielded to prevent the induction of eddy currents in the surrounding magnetic structure, which can distort the images. The shielding consists of a second coil set, surrounding the first or primary coil, which is designed to exactly cancel the field generated outside the secondary. The two coil sets are connected in series to avoid current imbalances, however this leads to a reduction in coil efficiency. To combat this, the distance between the two coils is maximised and as such the screen is wound onto a former with internal and external diameters of 850 and 874 mm respectively.

		Primary Coils	Shield Coils
Length / m		2.3	2.4
Inner Diameter / mm		600	850
Outer Diameter / mm		660	874
Number of Coil Turns	G_X	18	17
	G_Y	18	17
	G_Z	21	10

Table 4.1 – Gradient Coil Dimensions

	G_X	G_Y	G_Z
Current Ratio (Screen/Primary)	0.5	0.497	0.993
Primary Coil Radius / mm	323	318	313
Cylindrical Region of 95/105% Homogeneity (Diameter x Length) / mm	500 x 350	500 x 340	400 x 370
η / mTm^{-1}A^{-1}	0.062	0.064	0.094
L / μH	420	420	520
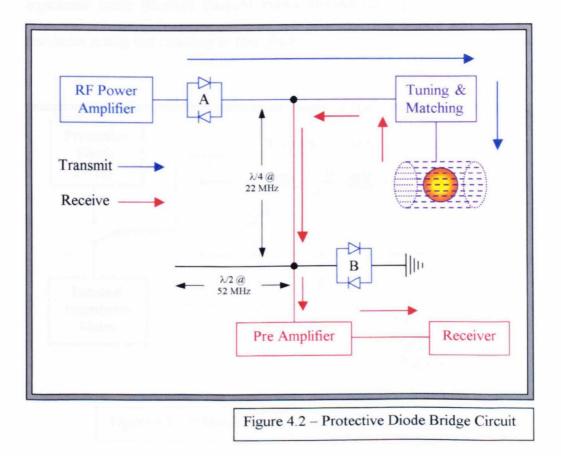
Table 4.2 – Series Gradient Coil Parameters

4.5 RF Transmitter

The RF waveform from the WC consists of the pulse profile, indicating the magnitude of the pulse envelope, and the real and imaginary components of the pulse. These waveforms are combined in the Phase Modulator and enable the generation of simple amplitude modulated pulses, like the sinc pulse, as well as more complex amplitude and phase modulated pulses, such as the hyperbolic secant pulse. The generated pulse is then modulated to 22 MHz before transmission to the 5 kW RF power amplifier, supplied by Amplifier Research (model 5000LP). The amplified signal is then passed to the RF coil via a protective diode bridge as shown in figure 4.2. The diode bridge is used to prevent the transmitted signal from damaging the pre amplifier, whilst at the same time precluding noise on the transmit line from being amplified with the received signal. The pre amplifier is protected because during transmission the two sets of crossed diodes (A & B) are made to conduct by the large amplitude signal. The
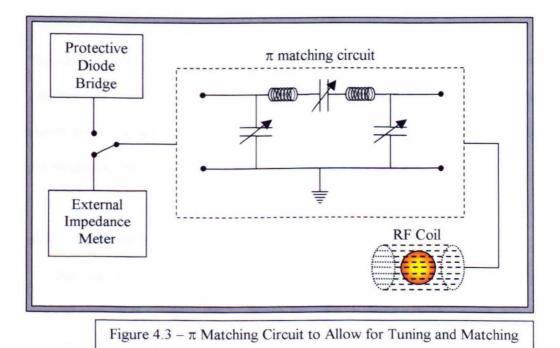
short circuit this creates in front of the pre amplifier appears as an open circuit due to the $\lambda/4$ cable and ensures all power is propagated to the tuning and matching circuit. During the receive period, the diodes will not conduct due to the small size of the induced emf. As such the transmission line and the route to earth is closed and the signal is directed through to the pre amplifier. An additional $\lambda/2$ at 52 MHz cable is inserted just before the pre amplifier to prevent the transmission of any signals at this frequency through the pre amplifier. Transmitted signals at 52 MHz may combine with the mixing frequencies of 37 MHz and 15 MHz, discussed in section 4.7, and contribute noise to the final image.

Figure 4.2 – Protective Diode Bridge Circuit

4.6   RF Coils

All experiments described were carried out on one of two RF transceiver coils;

a 16 rung, low-pass, capacitive drive, whole body birdcage coil (46 cm long and

48 cm internal diameter) and a 16 rung, low-pass, inductive drive, head birdcage

coil (35 cm long and 28 cm internal diameter). The body coil is fitted with a

slotted screen (65 cm long and 56 cm internal diameter) to prevent any coupling to

the surrounding environment. The slotted design is used to minimise the

circulation of eddy currents in the screen when loaded, both coils can be tuned to

22.03 MHz and impedance matched to 50 Ω using the π matching network shown

in figure 4.3. The tuning and matching circuit is connected to an external

impedance meter (Hewlett Packard model 4193A) via a $\lambda/2$ coaxial cable to

enable the tuning and matching to take place.

Figure 4.3 – π Matching Circuit to Allow for Tuning and Matching

4.7   RF Receiver

The low amplitude emf generated in the coil is initially amplified by a 50 dB pre amplifier (model AU-1313) provided by MITEQ. The amplified signal at 22 MHz is then combined with a reference signal at 37 MHz to produce a signal modulated at 15 MHz. Quadrature detection of the real and imaginary components is then carried out by the phase sensitive detector through the combination of the 15 MHz signal with another reference signal at the same frequency. The audio frequency signals produced are then passed through a variable bandwidth Butterworth filter before being digitised in the ADC.

4.8   Image Production

The digitised signal is Fourier transformed using in house software, again produced by Dr. Ron Coxon[1]. The software allows for the display of the pre transformed time data as well as the real, imaginary, phase and magnitude images that can be produced from the Fast Fourier Transform (FFT). It is also possible to produce half Fourier images as discussed further in chapter 7. The data can be saved in its original time format for later post processing or saved as image data for subsequent analysis using a range of in house or pre written software.

4.9   Summary

The scanner used for the work described in this thesis is purpose built for echo-planar image acquisition allowing the system design to be optimised to overcome the problems inherent in EPI. High gradient performance permits the rapid switching of the read gradient required and a high speed ADC allows fast data sampling. The low static field of the system is preferable when studying

pregnant volunteers due to the improved patient comfort and ease of use. The

reduction in safety concerns, further discussed in chapter 6, is also an advantage.

References

[1] Coxon, R. and P. Glover, *The Waveform Controller and Experimental Software.* 1995.
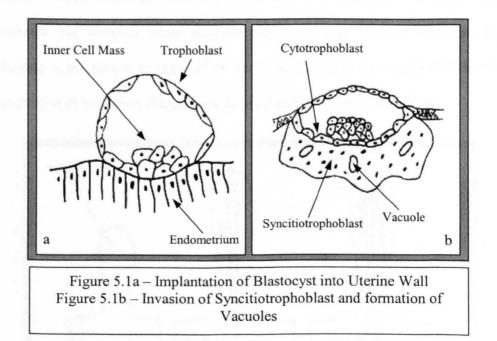
[2] Boulby, P., *The Assessment of Gastrointestinal Physiology by Echo Planar Imaging - Ph.D. Thesis*, in *School of Physics and Astronomy.* 1998, University of Nottingham: Nottingham.

[3] Traficante, D.D., *Impedance: What it is and Why it Must be Matched.* Concepts in Magnetic Resonance, 1989. 1: p. 73-92.

5 Anatomy and Pathology in Pregnancy

5.1 Fetal and Placental Anatomy and Development

For the developing fetus, the initial weeks of life involve a large increase in cell numbers with little increase in weight. The early embryonic cells migrate to form different regions of the body, such that by the sixth week the embryo is a 10 mm long cylinder with a distinct head and tail end. The developing heart is a simple pulsatile tube and the umbilical cord has formed. After eight weeks the fetus is 25 mm long with differentiated sex glands and limbs that are well formed with distinguishable fingers and toes. By the twelfth week, the fetus is 90 mm long and is well developed with all major organ systems present. From this point on, the development is mostly by growth, which is proportioned to the surface area of the placenta available for exchange[1,2].

Figure 5.1a – Implantation of Blastocyst into Uterine Wall
Figure 5.1b – Invasion of Syncitiotrophoblast and formation of Vacuoles

The placenta is initially formed by the invasion of the fertilised egg, or blastocyst, into the endometrial lining of the uterus on the sixth or seventh day after

conception. The syncitiotrophoblast cells surrounding the blastocyst penetrate the uterine lining and form a large cell mass filled with interconnecting vacuoles as demonstrated by figure 5.1b. The invading fetal cells erode maternal blood vessels causing the vacuoles to fill with maternal blood and the wall of the blastocyst, which is composed of cytotrophoblast cells, begins to develop into the syncitiotrophoblast region, forming villi. The villi initially appear as buds that penetrate the blood filled vacuoles until the appearance of mesoderm cells within them creates a basic capillary network. Figure 5.2 shows this developing network, which is capable of exchange between the fetal and maternal circulations at around the fifth week of gestation. The placenta continues to develop into a complicated and highly organised structure that is perfectly designed to act as an exchange point between the enclosed fetus and the mother. Through various transport mechanisms, the placenta provides the developing fetus with oxygen and nutrients and removes waste products that have been created. However, the placenta is not simply an organ of exchange because it is also responsible for the production of hormones that prepare the mother for the birth of the fetus.

Figure 5.2 – Development of Capillary Network Inside Fetal Villi

The fully developed placenta consists of many different villi, which continuously increase their potential for exchange by increasing their length, branching to form new villi and thinning their membranes. Exchange takes place when maternal blood squirts out under high pressure from the spiral arteries of the maternal tissue, or decidua, into the intervillous spaces where the villi float like fronds of seaweed. Figure 5.3 details how the maternal blood circulates around the villi, which are held in place by anchoring villi, until it drains back into the maternal circulation through veins in the decidual membrane. Increased blood flow to the placenta is achieved through the degradation of the muscular walls of the maternal spiral arteries. The transformed spiral arteries become like inelastic tubes with an increased lumen diameter causing a relatively low resistance to blood flow.

Figure 5.3 – Maternal Blood Circulating Around Fetal Villi

The correct growth and function of the placenta is essential if the fetus is to develop normally. Any complications that reduce the ability of the placenta to provide an adequate exchange site can have serious consequences for both the fetus and the mother.

5.2 Fetal and Placental Pathology

If the trophoblast does not implant correctly into the endometrium, there is no change in the maternal spiral arteries causing a high resistance pathway. This causes the utero-placental blood flow to be impeded, leading to insufficient supply of oxygen and nutrients to the fetus. This condition, known as placental insufficiency, can lead to Intrauterine Growth Restriction (IUGR) in early pregnancy and fetal hypoxia and death in the more advanced stages. IUGR is not only linked with significant fetal problems but has also been associated with an increased incidence of serious adult diseases in later life. In all of the work described in this thesis a diagnosis of IUGR was made on the basis of a reduced growth velocity as demonstrated by ultrasound scan or by an abnormal Doppler ultrasound waveform in the umbilical artery. The diagnosis was then confirmed at delivery if the Individualised Birthweight Ratio (IBR) was below the fifth centile. The IBR is a measure of fetal outcome that takes into account gestational age at delivery, parity, fetal sex, maternal height and ethnic origin as well as birthweight[3].

IUGR is often associated with another complication of pregnancy known as Essential Hypertension or Pre-Eclampsia (PE), which is a common condition that is found in up to ten percent of pregnancies in the UK[4]. The exact cause of PE is unknown but it has been suggested that it may be due to a failure of the immune

tolerance between the mother and fetus, poor trophoblastic invasion or genetic factors[5]. Whatever the reason, the condition is characterised by a failure of the maternal vasculature to adapt correctly to the pregnancy leading to a poor placental perfusion and an insufficient supply of oxygen and nutrients to the fetus. The high resistance to blood flow also causes the onset of maternal hypertension and a poor blood supply to the kidneys. The decrease in the renal blood supply prevents the correct function of the kidneys and eventually induces the release of protein in the urine (Proteinuria) and the retention of water. These symptoms can endanger the lives of the fetus and the mother and may lead to eclampsia, or fitting, in the later stages of pregnancy. Although untreatable, early diagnosis of pre-eclampsia is essential to allow constant monitoring of the well being of the patient. If the symptoms escalate and the lives of the mother or the fetus are at risk, delivery of the fetus can be considered by induction or by Caesarean section. In this work, pre-eclampsia has been characterised by an increase in the maternal blood pressure to at least 140/90 mmHg and the presence of Proteinuria at a level of 0.5 g/l in a 24 hour period.

As mentioned, fetal growth can be measured with the use of ultrasound techniques and abnormal blood supply to the placenta can be monitored by observation of the blood velocities in the uterine and umbilical arteries using Doppler ultrasound. However, these measurements yield no information about the structure of the placenta or the way that blood flows through it in conditions like pre-eclampsia or intrauterine growth restriction. The ability of MRI, and EPI in particular, to provide detailed quantitative results about structure and blood flow makes it an ideal technique to investigate further the abnormalities of the placenta in these severe conditions of pregnancy. EPI can be used to make measurements of NMR

parameters[6], such as relaxation times and magnetisation transfer coefficients, which may provide additional information about normal and pathological anatomy in the placenta. It is also possible to directly study blood flow[7,8] and perfusion[9,10] within the placenta with the use of several different flow sensitive techniques.

References

[1] Polin, R.A. and W.W. Fox, *Fetal and Neonatal Physiology*. 2nd ed. 1997: WB Saunders. 2765.

[2] Symonds, E.M. and I.M. Symonds, *Essential Obstetrics and Gynaecology*. 3rd ed. 1998, New York: Churchill Livingstone. 336.

[3] Wilcox, M.A., et al., *The Individualized Birth-Weight Ratio - a More Logical Outcome Measure of Pregnancy Than Birth-Weight Alone*. British Journal of Obstetrics and Gynaecology, 1993. **100**(4): p. 342-347.

[4] Hull, M., et al., *Undergraduate Obstetrics and Gynaecology*. 3rd ed. 1997: Butterworth-Heinemann. 467.

[5] Chamberlain, G., *Lecture Notes on Obstetrics*. 4th ed. 1980: Blackwell Scientific Publications. 309.

[6] Gowland, P.A., et al., *In vivo relaxation time measurements in the human placenta using echo planar imaging at 0.5 T*. Magnetic Resonance Imaging, 1998. **16**(3): p. 241-247.

[7] Moore, R.J., et al., *In vivo intravoxel incoherent motion measurements in the human placenta using echo-planar imaging at 0.5 T*. Magnetic Resonance in Medicine, 2000. **43**(2): p. 295-302.

[8] Moore, R.J., et al., *In utero perfusing fraction maps in normal and growth restricted pregnancy measured using IVIM echo-planar MRI*. Placenta, 2000. **21**(7): p. 726-732.

[9] Francis, S.T., et al., *Non-invasive mapping of placental perfusion*. Lancet, 1998. **351**(9113): p. 1397-1399.

[10] Gowland, P.A., et al., *In vivo perfusion measurements in the human placenta using echo planar imaging at 0.5 T*. Magnetic Resonance in Medicine, 1998. **40**(3): p. 467-473.

[11] Asch, R.H. and J.W.W. Studd, *Advances in Reproductive Medicine - Volume 2*. 1995: Parthenon Publishing. 300.

[12] Ashworth, J.R., et al., *Loss of endothelium-dependent relaxation in myometrial resistance arteries in pre-eclampsia*. British Journal of Obstetrics and Gynaecology, 1997. **104**(10): p. 1152-1158.

[13] Baker, P.N., et al., *Estimation of Fetal Lung Volume Using Echo-Planar Magnetic Resonance Imaging*. Obstetrics and Gynecology, 1994. **83**(6): p. 951-954.

[14] Baker, P.N., et al., *Measurement of Fetal Liver, Brain and Placental Volumes with Echo-Planar Magnetic-Resonance-Imaging*. British Journal of Obstetrics and Gynaecology, 1995. **102**(1): p. 35-39.

[15] Baker, P.N., et al., *Fetal Weight Estimation by Echo-Planar Magnetic-Resonance- Imaging*. Lancet, 1994. **343**(8898): p. 644-645.

[16] Brosens, I., H.G. Dixon, and W.B. Robertson, *Fetal Growth Retardation and the Arteries of the Placental Bed*. British Journal of Obstetrics and Gynaecology, 1977. **84**: p. 656-663.

[17] Cameron, A.D., et al., *Doppler Waveforms in the Fetal Aorta and Umbilical Artery in Patients with Hypertension in Pregnancy*. American Journal of Obstetrics and Gynecology, 1988. **158**(2): p. 339-345.

[18] Duncan, K.R., et al., *Assessment of fetal lung growth in utero with echo-planar MR imaging*. Radiology, 1999. **210**(1): p. 197-200.

[19] Johnson, I.R., et al., *Study of Internal Structure of the Human Fetus Inutero by Echo- Planar Magnetic-Resonance-Imaging*. American Journal of Obstetrics and Gynecology, 1990. **163**(2): p. 601-607.

[20] Johnson, I.R., et al., *Imaging the Pregnant Human-Uterus with Nuclear Magnetic- Resonance*. American Journal of Obstetrics and Gynecology, 1984. **148**(8): p. 1136-1139.

[21] Khong, T.Y., et al., *Inadequate Maternal Vascular-Response to Placentation in Pregnancies Complicated by Preeclampsia and by Small-for- Gestational-Age Infants.* British Journal of Obstetrics and Gynaecology, 1986. **93**(10): p. 1049-1059.

[22] Levine, D. and P.D. Barnes, *Cortical maturation in normal and abnormal fetuses as assessed with prenatal MR imaging.* Radiology, 1999. **210**(3): p. 751-758.

[23] Mansfield, P., et al., *Echo Planar Imaging of the Human Fetus Inutero at 0.5-T.* British Journal of Radiology, 1990. **63**(755): p. 833-841.

[24] Moore, R.J., et al., *In vivo diffusion measurements as an indication of fetal lung maturation using echo planar imaging at 0.5T.* Magnetic Resonance in Medicine, 2001. **45**(2): p. 247-253.

[25] Moore, R.J., et al., *Antenatal determination of fetal brain activity in response to an acoustic stimulus using functional magnetic resonance imaging.* Human Brain Mapping, 2001. **12**(2): p. 94-99.

[26] Powell, M.C., et al., *Magnetic-Resonance Imaging (Mri) in Obstetrics .2. Fetal Anatomy.* British Journal of Obstetrics and Gynaecology, 1988. **95**(1): p. 38-46.

[27] Roberts, N., et al., *Estimation of Fetal Volume by Magnetic-Resonance-Imaging and Stereology.* British Journal of Radiology, 1994. **67**(803): p. 1067-1077.

[28] Sheppard, B.L. and J. Bonnar, *The Ultrastructure of the Arterial Supply of the Human Placenta in Pregnancy Complicated by Fetal Growth Retardation.* British Journal of Obstetrics and Gynaecology, 1976. **83**: p. 948-959.

[29] Smith, F.W., et al., *NMR Imaging in Human Pregnancy: A Preliminary Study.* Magnetic Resonance Imaging, 1984. **2**: p. 57-64.

[30] Stehling, M.K., et al., *Echo-Planar Imaging of the Human Fetus Inutero.* Magnetic Resonance in Medicine, 1990. **13**(2): p. 314-318.

[31] Trudinger, B.J. and C.M. Cook, *Doppler Umbilical and Uterine Flow Wave-Forms in Severe Pregnancy Hypertension.* British Journal of Obstetrics and Gynaecology, 1990. **97**(2): p. 142-148.

6   Safety Issues Relating to MR Imaging in Pregnancy

6.1   Introduction

Safety must be the first concern for any medical imaging technique, especially one that is relatively new and rapidly developing such as magnetic resonance imaging. MRI is considered to be a safe imaging modality because there is no use of ionising radiation, but there are safety considerations that must be taken into account whenever anyone undergoes an examination. The possible risks involved in an MRI exam can be considered to arise from any one of the three types of magnetic field encountered by the patient during a scan. These fields are the static magnetic field, the spatially and temporally varying field (gradient field) and the radiofrequency field. The following three sections outline the particular risks and concerns that arise due to each of these magnetic fields and details issues that are particularly relevant to echo planar imaging techniques.

At the present moment, the clinical use of MRI during pregnancy is still limited and so, at this early stage, concern must be paid to the particular safety issues surrounding the imaging of pregnant patients. The developing fetus is contained in a unique environment that posses certain issues that must be addressed before the absolute safety of the technique can be assured. As such, the final section of this chapter covers safety concerns that are of specific interest to obstetric echo planar MRI. The section also reviews the relevant safety literature produced from the work that has been carried out over the last 13 years in Nottingham.

6.2   The Static Magnetic Field

Safety issues surrounding the use of the large static magnetic fields needed for MRI can be divided into two main groups; the possibility of any detrimental

bioeffects caused, and the hazards that arise due to the presence of metallic objects in the scanning environment. There is a wealth of literature covering the possible bioeffects that might occur due to exposure to large static magnetic fields. Many different groups have reported adverse reactions brought about by high field exposure but most of these findings have proved impossible to repeat. It has been demonstrated that, due to the conductive nature of blood, there is an increase in the t-wave amplitude on an electrocardiogram that is proportional to the magnitude of the static field. There is also evidence that fibrin and fibrinogen, as well as deoxygenated sickled red blood cells, will align with strong magnetic fields[1]. However, neither of these findings have been shown to be clinically significant.

Although there are no indications that short-term exposure to static fields below 2 T has any detrimental effect, there have been reports of patients exposed to higher field strengths experiencing unwanted side effects including nausea, dizziness and vertigo. These symptoms have been related to the effect of movement through a static magnetic field on the conducting fluid in the middle ear. There have also been reports of magnetophosphenes or flashes of light caused by direct stimulation of the optic nerve in people working in and around 4 T MR systems due to motion through the large static field[1,2]. Due to the continuing trend to scan at higher field strengths and the imminent production of clinical MRI scanners that operate at 3 T, it is important that any possible safety concerns are monitored very closely. The guidelines on static field exposure issued by the National Radiological Protection Board (NRPB) for clinical magnetic resonance procedures are detailed in table 6.1[3]. They include limits for uncontrolled patient examination and upper limits for patients who are physiologically monitored during the scan.

Part of Body	Uncontrolled Level (T)	Upper Level (T)
Trunk and Head	2.5	4.0
Limbs	4.0	4.0

Table 6.1 – NRPB Limits on Static Magnetic Field Exposure

The presence of metallic objects in the scanning environment is a more direct concern. The possible hazard of loose metal objects being drawn towards the scanner and injuring anyone inside the scanner or in the path of the object must be prevented. It is usual to achieve this by screening patients and their relatives before they enter the scanner room and restricting all other access to trained personnel. The possible effect that the static field may have on any metallic implants inside the patient must also be considered. The chance that an implant may be dislodged or stopped from functioning, as in the case of an artificial pacemaker, is a serious contraindication for an MRI exam. Again, the use of careful screening procedures can help to prevent any unsuitable patients from being scanned and the growing use of MRI compatible implants is further limiting the possibility of any adverse events.

6.3   Spatially and Temporally Varying Magnetic Fields

Spatially and temporally varying magnetic fields are used in MRI to provide positional information and allow the formation of images. The possible adverse effects of these fields come about due to the induction of voltages in any conducting material within the scanner. The magnitude of the induced voltage will

depend on the rate of change of the magnetic field and so will be increased by larger gradients or faster switching times. This is a considerable problem when using EPI due to the large and rapidly switched gradients that are used to produce the frequency encoding. The induction of voltages or currents within the patient could lead to power deposition and hence heating of the tissue. However, it is accepted that the levels of power deposited due to gradient switching in MRI are clinically insignificant. A more important consideration is the possibility of direct neuromuscular stimulation caused by the induced currents or voltages. There is a chance of cardiac fibrillation or nerve activation, but only at current density levels significantly higher than those commonly used in clinical imaging. However, further consideration must be given when scanning patients who may be particularly susceptible to the induced currents or voltages. For example, patients who have reduced nerve activation potentials due to disease or patients who have conductive pathways, such as those created by cardiac triggering leads that have not been fully removed after a surgical procedure. To ensure no undesirable effects the NRPB guidelines are particularly conservative and they are detailed in table 6.2[3].

Another problem caused by the gradient fields is an acoustic one, which is brought about by the movement of the gradient coils. Due to their position in the static magnetic field, a torque is generated on the coils when currents are passed through them making the coil act like a loud speaker. In imaging sequences like EPI, where the gradients are switched at relatively high rates, the noises generated can be in excess of 100 dB and would be detrimental to the patient and anybody within the scanner room. Providing patients with foam earplugs or MR compatible headphones, which can attenuate the sound levels down to an acceptable level, can

alleviate this problem. There is currently a considerable amount of research taking place to reduce the sound levels produced through the use of active or passive noise cancellation.

Duration of Field Change	Uncontrolled Level (Ts^{-1})	Upper Level (Ts^{-1})
t > 3 ms	20	20
120 μs < t < 3 ms	20	60×10^{-3} / t
45 μs < t < 120 μs	2.4×10^{-3} / t	60×10^{-3} / t
2.5 μs < t < 45 μs	2.4×10^{-3} / t	1300^{*} $(2\ Wkg^{-1})^{\#}$
t < 2.5 μs	950^{*} $(1\ Wkg^{-1})^{\#}$	1300^{*} $(2\ Wkg^{-1})^{\#}$

Table 6.2 – NRPB Limits on Rate of Change of Magnetic Flux Density (dB/dt)

6.4   Radiofrequency Magnetic Fields

The RF power that is transmitted to the patient during an MR examination is mostly transformed into heat within the patient's tissues. Thus any adverse biological effect from the RF field is thought to be due to the increased heat load that this may place on the patient. It is known that an elevated body temperature can lead to an increased heart rate and blood pressure and their relevant consequences. Additional concern must also be paid to temperature sensitive organs like the eye and the testis. Particular attention must be given to patients

---

* Peak dB/dt values are calculated assuming a tissue electric conductivity of 0.4 Sm^{-1} and an inductive loop radius of 0.15 m.
# At such rapid switching rates, tissue heating can become significant and so maximum energy deposition levels are also quoted.

who may have a compromised ability to cope with an increased heat load, for example patients with cardiovascular disease, diabetes and obesity. Some medications, such as sedatives, diuretics and β-blockers, may also hamper the body's ability to regulate temperature. The increase in temperature that is experienced by a patient is related to the amount of energy that they absorb. The absorbed energy is quoted as the Specific Absorption Rate (SAR), in units of watts per kilogram (W/kg), and depends on many factors including the efficiency of the coil, the resonant frequency, the volume of tissue within the coil and the type of RF pulse used. The transfer of energy is found to be most efficient when the tissue thickness is approximately half the wavelength of the incident radiation. For MR imaging at 0.5 T, the wavelength is approximately 15 cm and as such the absorption is mostly at the surface of the patient causing heating of the subcutaneous tissues. The NRPB have set down guidelines for maximal whole body and part body exposure to RF radiation in terms of the SAR and the associated temperature increase that is permitted[3]. These guidelines are summarised in tables 6.3 and 6.4.

	Uncontrolled Level	Upper Level
Whole Body Temperature Increase (°C)	0.5	1.0
Whole Body SAR* (Duration of Exposure)	1 W/kg (>30 min)	2 W/kg (>30 min)
	30 Wmin/kg (15-30 min)	60 Wmin/kg (15-30 min)
	2 W/kg (<15 min)	4 W/kg (<15 min)

Table 6.3 – NRPB Limits on Whole Body RF Radiation Exposure

There have been suggestions that there may also be effects due to non-thermal mechanisms associated with RF radiation but it is considered that these effects would occur at levels above those needed to induce thermal effects. The use of EPI alleviates RF heating concerns to a large extent because each image is produced with a single RF excitation.

	Head	Trunk	Limbs
Maximal Local Tissue Temperature (°C)	38	39	40
Part Body SAR# (Duration of Exposure)	2 W/kg (>30 min)	4 W/kg (>30 min)	6 W/kg (>30 min)
	60 Wmin/kg (15-30 min)	120 Wmin/kg (15-30 min)	180 Wmin/kg (15-30 min)
	4 W/kg (<15 min)	8 W/kg (<15 min)	12 W/kg (<15 min)

Table 6.4 – Limits on Part Body RF Radiation Exposure

---

* Averaged over any 15 min period.
# For any one kilogram of tissue and averaged over any 6 min period.

6.5   *MR Safety in Pregnancy*

Although not routinely used in the clinical assessment of pregnancy, the use of MRI in research into the complications of pregnancy has greatly increased in the past few years[4]. Also, with the large increase in the number of patients undergoing MR scans, there is a higher probability of scanning an expectant mother for conditions unrelated to the pregnancy. It is at this early stage in the development of obstetric MRI that the absolute safety of the technique must be assured. The effects and concerns outlined in the previous sections are obviously relevant to the safety of a pregnant patient, but there are specific considerations that must be given in the case of assessing the safety of obstetric MRI.

The early stages of development of the fetus involve a rapid increase in cell numbers and cell specificity. During the process of cell division the DNA is particularly vulnerable to damage and this is a major concern, especially when there are very few cells that will go on to make up each organ in the fetus. Although there is no concrete evidence to prove that there are any harmful effects on the process of cell division caused by the large static magnetic fields used in MRI, there have been concerning reports that would indicate a cautious approach. The large static magnetic field must also be considered due to its possible effect on the process of cell migration. One of the proposed methods for the movement of cells to form the different fetal organs is termed galvanotaxis. This is a process that relies on the presence of small potential differences, which cause cells to migrate to specific parts of the developing embryo. Movement through the static field, or the presence of gradient fields, could generate voltages that would disrupt galvanotaxis and lead to developmental abnormalities. To minimise the possibility

of this, or any adverse effect on cell division, scanning is not carried out in the first trimester of pregnancy.

The effect of the rapidly switched gradient fields used in EPI is a particular concern in obstetric MRI. The possibility of cardiac defibrillation is increased because the fluid filled lungs and subsequently the fluid filled amniotic sac surround the fetal heart, generating a larger area for the induction of currents by the time varying magnetic fields. However, the risk is reduced by the central location of the fetal heart where the magnitude of the field variation is minimal. A study carried out to monitor the fetal heart rate before and during magnetic resonance imaging revealed no apparent alteration of the heart rate parameters due to the imaging technique[5]. This is a result that not only indicates that MRI has no direct effect on fetal cardiac performance but also on fetal well-being, which FHR is considered to be a marker of.

The acoustic noise inherent in the EPI technique is another cause for concern when considering obstetric MRI. It is a simple procedure to supply the mother with ear protection during the examination but the same cannot be said for the fetus. However, protection is offered due to the poor mismatch of sound transfer from the air to the abdominal wall and amniotic fluid. To ensure that a suitable level of protection was being offered by this sound mismatch, the sound level was measured by a hydrophone inside a fluid filled stomach. It was shown that sound levels were attenuated to an acceptable level, below 90 dB, and that much higher peak pressures could be generated by finger tapping on the abdomen[6]. The lack of any adverse effect due to the acoustic noise has also been demonstrated by the absence of any hearing deficits in nine-month and three-year follow up studies of children imaged *in utero*[7,8].

As with any patients, the concern with the applied RF magnetic field is the possibility of tissue heating. In this respect the developing fetus may be at considerable risk because of the limited thermoregulatory system caused by the separation of the maternal and fetal circulations. When using EPI, the SAR levels are minimal and any adverse effects should be prevented. This is born out by the absence of any fetal heart rate changes during MRI as previously mentioned. However, additional care must be taken when using more SAR intensive sequences like RARE or magnetisation transfer contrast. A greater discussion of the SAR issues raised by MT imaging sequences can be found in chapter 8.

Due to the inability of the investigator to thoroughly analyse the well-being of the fetus at the time of imaging, except when using FHR measurements, the safety of MR imaging during pregnancy must be assessed retrospectively. As such, several reports have been submitted from the Nottingham group on the outcome of pregnancies monitored with echo planar MRI[7,8,9]. An initial three-year follow up of 20 compromised pregnancies revealed no demonstrable increase in the occurrence of disease or disability (including hearing deficit) that could be related to echo-planar imaging techniques. A subsequent study of 74 pregnant women who underwent exposure to EPI during their pregnancy showed a significantly lower birthweight and a lower gestational age at delivery to a matched control group. However, the lower gestational age at delivery can be linked to the increased obstetric intervention of the study group and when the individualised birthweight ratio[10] was calculated there were no significant differences shown, which would indicate that echo planar imaging did not have a marked effect on intrauterine fetal growth. A further study of 20 infants exposed to echo planar imaging *in utero* showed a normal paediatric assessment at nine months of age. A

small decrease in length was shown, along with an increase in gross motor function. A ten year follow up of children imaged *in utero* is currently being performed but these initial findings would seem to demonstrate that there are no significant adverse reactions to the use of EPI during the second and third trimesters of pregnancy. The current guidelines from the NRPB preclude scanning in the first trimester and only allows clinical imaging up to the lower safety levels presented in this chapter when the only reasonable alternative to MR imaging would involve ionising radiation. It seems that with the growing body of evidence to suggest the safety of the technique and its usefulness in providing pertinent clinical information, it is only a short time before clinical application of obstetric MRI becomes common place. This would also allow for a more complete study of the safety issues with a considerably larger follow up study possible.

References

[1] F. G. Shellock & E. Kanal (1996) Magnetic Resonance: Bioeffects, Safety, and Patient Management (2nd Ed). Pub. By Lippincott, Williams & Wilkins.

[2] Budinger, T.F., *Nuclear Magnetic-Resonance (Nmr) Invivo Studies - Known Thresholds for Health-Effects.* Journal of Computer Assisted Tomography, 1981. 5(6): p. 800-811.

[3] NRPB, *Documents of the NRPB - Board Statement on Clinical Magnetic Resonance Diagnostic Procedures.* 1991, National Radiological Protection Board: Didcot, Oxon.

[4] Garel, C., et al., *Magnetic resonance imaging of the fetus.* Pediatric Radiology, 1998. 28(4): p. 201-211.

[5] Vadeyar, S.H., et al., *Effect of fetal magnetic resonance imaging on fetal heart rate patterns.* American Journal of Obstetrics and Gynecology, 2000. 182(3): p. 666-669.

[6] Glover, P., et al., *An Assessment of the Intrauterine Sound Intensity Level During Obstetric Echo-Planar Magnetic-Resonance-Imaging.* British Journal of Radiology, 1995. 68(814): p. 1090-1094.

[7] Clements, H., et al., *Infants exposed to MRI in utero have a normal paediatric assessment at 9 months of age.* British Journal of Radiology, 2000. 73(866): p. 190-194.

[8] Baker, P.N., et al., *A Three Year Follow-Up of Children Imaged in Utero with Echo-Planar Magnetic Resonance.* American Journal of Obstetrics and Gynecology, 1994. 170(1): p. 32-33.

[9] Myers, C., et al., *Failure to detect intrauterine growth restriction following in utero exposure to MRI.* British Journal of Radiology, 1998. 71(845): p. 549-551.

[10] Wilcox, M.A., et al., *The Individualized Birth-Weight Ratio - a More Logical Outcome Measure of Pregnancy Than Birth-Weight Alone.* British Journal of Obstetrics and Gynaecology, 1993. 100(4): p. 342-347.

[11] Duncan, K., et al., *Treat patients with kindness during magnetic resonance imaging.* British Medical Journal, 1996. 312(7043): p. 1421-1421.

[12] Shellock, F.G., C.A. Litwer, and E. Kanal, *Magnetic Resonance Imaging: Bioeffects, Safety, and Patient Management.* Reviews of Magnetic Resonance in Medicine, 1992. 4: p. 22-63.

[13] Moore, R.J., *The Application of Magnetic Resonance Imaging to Obstetrics - Ph.D. Thesis,* in *School of Physics and Astronomy.* 2001, University of Nottingham.

[14] NRPB, Documents of the NRPB - Board Statement on Restrictions on Human Exposure to Static and Time Varying Electromagnetic Fields and Radiation. 1993, National Radiological Protection Board: Didcot, Oxon.

[15] Smith, H., Revised Guidance on Acceptable Limits of Exposure During Nuclear Magnetic-Resonance Clinical Imaging. British Journal of Radiology, 1983. 56(672): p. 974-977.

7   Multi-Echo Measurement of the Transverse Relaxation Time

7.1   Introduction

The transverse relaxation time, T_2, can provide useful information in many circumstances. Previous measurements in the human placenta have shown a trend for T_2 to decrease through the gestational period[1]. It has also been shown that the transverse relaxation time is generally lower in pregnancies compromised by IUGR or Pre-Eclampsia. However, random and non-periodic motions of the fetus hamper accurate quantitative measurement, causing an increase in the error associated with any such measurements. The ability to produce a quantitative measurement of the transverse relaxation time from a single FID would improve the precision of *in vivo* T_2 measurements and would also allow for mapping of the transverse relaxation time on a pixel-by-pixel basis, making it possible to determine any positional variation in the measurement. Transverse relaxation time measurements have also been used previously to monitor the dilution of model meals in the human stomach[2,3]. The rate of dilution is of the same order as the time used to produce the measurement and as such valuable information may be being lost. The use of a rapid sequence to measure T_2 would again be useful to increase the accuracy of such experiments.
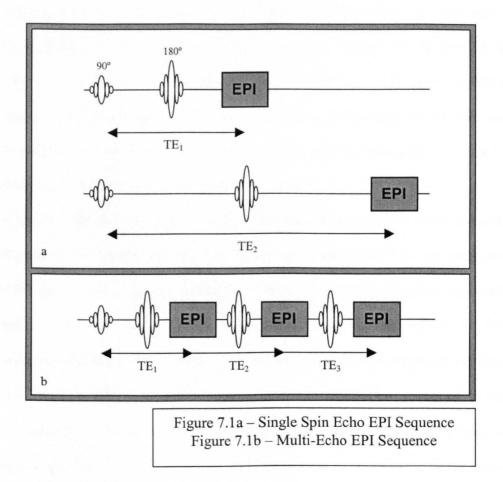
Measurements of T_2 are usually made using multi-echo 2DFT (Spin Warp) imaging sequences, which are highly efficient in terms of signal to noise per unit time, and which also reduce errors introduced into the measurement due to diffusion processes[4]. However, they are particularly prone to errors in the RF inversion/refocusing pulses used to create the chain of spin echoes. Incomplete

inversion of the transverse magnetisation can lead to the generation of a longitudinal component of magnetisation as well as a refocused and an unaffected transverse component that will, with successive applications of the imperfect pulse, interact in a complex manner[5]. This will produce a chain of echoes with amplitudes that yield a poor fit to the exponential form expected and inaccurate estimates of T_2. The multi-echo 2DFT sequences can also be very time consuming (~30 minutes), due to the relatively long repetition times used and the need for phase cycling. This is an unacceptably long time if the focus of the study is an organ that is prone to unpredictable or non-periodic motions, such as the placenta or the stomach, or if the transverse relaxation time is varying on a time scale that is significantly less than the measurement time, such as measurement of gastric dilution.

In the studies previously mentioned[1,2,3], the measurement time was reduced and the sensitivity to RF pulse errors was removed with the use of a single spin echo EPI sequence as shown in figure 7.1a. However, the single spin echo measurement still takes approximately 3 minutes and it has long been recognised that such sequences can suffer from errors due to spin diffusion within local field inhomogeneities in the time between the excitation and the echo formation[4]. These diffusion errors can be minimised with the use of a multi-echo sequence. In this chapter, the combination of the multi-echo sequence with the rapid acquisition of EPI has been used to minimise the measurement time and to also reduce any diffusion related errors. The major problem of errors introduced by the multi-echo sequence's natural sensitivity to RF inversion pulse errors was tackled by applying spoiling gradients and adiabatic refocusing. The completed sequence, shown in figure 7.1b, has been used to measure the transverse relaxation time in

the human placenta and of model meals in the human stomach as well as to subsequently monitor gastric dilution rates *in vivo*.

Figure 7.1a – Single Spin Echo EPI Sequence
Figure 7.1b – Multi-Echo EPI Sequence

7.2   *RF Insensitive Multi-Echo T₂ Measurement Techniques*
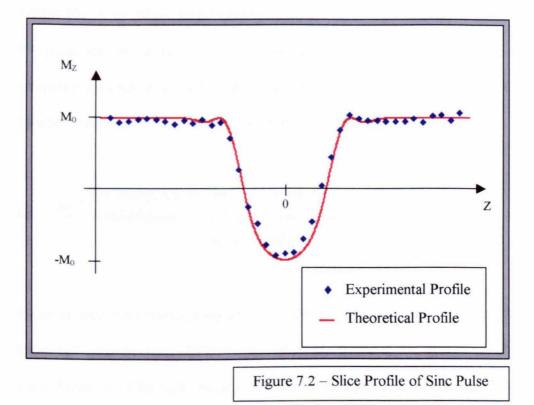
The multi-echo sequence simply consists of a 90° pulse, followed by a chain of echoes created by a series of inversion pulses. The sequence was originally designed to reduce the diffusion and flow effects that can hamper spin echo measurements of the transverse relaxation time[4]. The spin echo sequence works because the phase shift given to any particular spin by inhomogeneities in the local magnetic field are completely reversed after the action of a 180° pulse. Diffusing or flowing spins that are moving in space will receive different phase shifts before and after the inversion pulse because the local field will be varying.

In between the inversion pulses, the echo is acquired to produce a signal reflecting the transverse magnetisation at that particular echo time. In general, for spin warp imaging, the echo is acquired under a read gradient to fill a single line in k-space. By measuring the signal from the chain of echoes, images can be built up at different echo times. The transverse relaxation time can be obtained by fitting equation 2.26 to the image signal intensities. The number of data points that can be obtained for the fit is clearly limited by the number of echoes that can be created before the signal has completely died away.

In practice, the inversion pulses are applied along the y-axis of the rotating frame, which is a 90° phase shift from the initial excitation pulse. This provides two advantages to the sequence. Firstly, the echoes are all refocused along the y-axis rather than alternately on the ±y-axes and, secondly, the effects of any imperfections in the 180° pulses are reduced, as they tend to cancel rather than add[6]. Despite this, the main problem with the multi-echo sequence is the increasing loss of signal with echo time due to pulse imperfections, which leads to an underestimate of the transverse relaxation time[5]. Imperfections in the pulse amplitudes are almost intrinsic to MRI. They arise from RF coil inhomogeneity, poor slice profile or inaccurate setting of the RF amplitude. If the pulse does not cause an inversion over the entire region of spins selected by the excitation pulse, then spins at the extremes of the selected region will be rotated through less than 180°. The optimum slice profile is a rectangle, so that the RF power provided to all spins in the selected region is constant. If a Gaussian pulse is used then the pulse profile is Gaussian in shape and as such the edges of the region are poorly defined leading to spins that are not fully inverted. However, if a sinc pulse shape is used, then the pulse profile approaches the ideal form of a rectangle and so is

more useful in creating a region of constant rotation. Yet the result is still far from perfect as demonstrated by the profile shown in figure 7.2.

Figure 7.2 – Slice Profile of Sinc Pulse

The multi-echo sequence is particularly sensitive to RF pulse errors because of the cumulative nature of any errors in the chain of spin echoes that are produced. If the inversion pulse generates less than a $180°$ rotation of the transverse magnetisation, the solution of the Bloch equations with standard rotation matrices shows that three components of magnetisation are created[5]. If the rotation of the magnetisation caused by a $\theta°$ RF pulse is described by the matrix $\mathbf{R}[\theta]$ and the free precession of the magnetisation is described by the matrix $\mathbf{P}[t]$, then the magnetisation $\mathbf{M}_1[t]$ at a time, t, after the application of the $\theta°$ inversion pulse in a single spin-echo experiment is given by the following matrix equation.

$$\mathbf{M}_1[t] = \mathbf{P}[t]\mathbf{R}_y[\theta]\mathbf{P}[\tau]\mathbf{R}_x[90°]\mathbf{M}_0 \qquad - \qquad 7.1$$

Where $\mathbf{M}_0$ is the initial magnetisation $(0, 0, M_0)$ and τ is the time between the

$90°$ pulse and the inversion pulse. Assuming the $90°$ pulse is perfect and the

relaxation parameters T_1 and T_2 are long compared to τ, the solution of this

equation leads to the following expression for the magnetisation.

$$\mathbf{M}_1 = \frac{M_0}{2} \begin{bmatrix} (1+\cos(\theta))\sin(\omega t + \omega\tau) + (1-\cos(\theta))\sin(\omega t - \omega\tau) \\ (1+\cos(\theta))\cos(\omega t + \omega\tau) + (1-\cos(\theta))\cos(\omega t - \omega\tau) \\ -2\sin(\omega\tau)\sin(\theta) \end{bmatrix} \qquad - \qquad 7.2$$
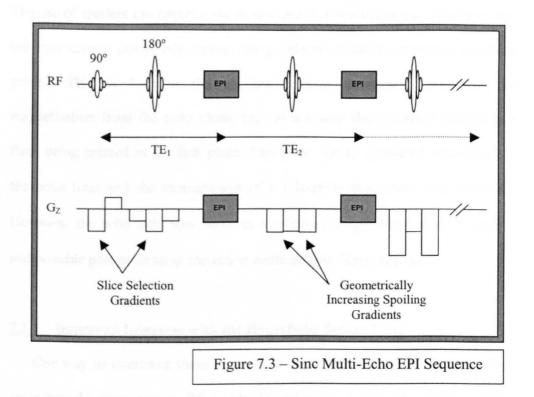
It can be seen from studying equation 7.2, that the application of a perfect $180°$

pulse will generate magnetisation only along the y-axis at the spin echo when

$t = \tau$. However, if the pulse yields a rotation that is imperfect ($\theta \neq 180°$), then the

magnetisation produced can be resolved into three separate components; one

component along the longitudinal axis and two in the transverse plane. One of the

transverse components can be considered to be due to spins that were unaffected

by the inversion pulse and the other due to spins that received the expected

inversion, giving rise to the spin echo. In a single spin echo sequence, the pulse

error simply reduces the measured intensity but has no effect on the measurement

of T_2 as each echo receives the same fractional reduction. However, when the

multi-echo sequence is used the errors propagate from one echo to the next, and

the components of magnetisation combine in a complex way. This generates an

echo chain that does not fit to the expected exponential decay and may show

oscillations. The measurement will yield a T_2 value that is generally lower than

that achieved with a single spin echo sequence. The stimulated echoes created can also give rise to mirror artefacts in 2DFT imaging and are normally overcome by various methods of phase cycling[7], although this is not a problem with EPI encoding.

To improve the multi-echo sequence, two methods can be used to prevent the RF pulse errors from affecting the transverse relaxation time measurement. The first is to prevent the unwanted components persisting through the echo chain by spoiling around each inversion pulse. This will prevent the formation of spurious echoes but will cause increasing attenuation of the echoes in the train. A better method would be to improve the inversion pulses to provide a more accurate inversion in the first place.

7.2.1 Spoiling

Spoiling (or crushing) of the transverse magnetisation is required in the multi-echo sequence to dephase any transverse magnetisation created by the refocusing pulse. It can also be used to dephase transverse components that have not been refocused by every inversion pulse whilst leaving the magnetisation that was refocused by every pulse unaffected. This can be achieved by placing spoiling gradients, of the same duration and amplitude, on either side of the inversion pulses as shown in figure 7.3. The first gradient causes a dephasing of all transverse components and the second gradient only refocuses the component inverted by the intervening RF pulse. The component that was left unaffected by the pulse will continue to dephase under the effect of the second gradient, resulting in negligible contribution to the measured signal.

Figure 7.3 – Sinc Multi-Echo EPI Sequence
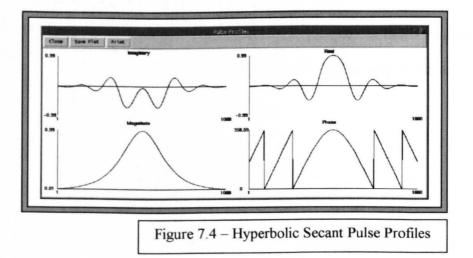
Spoiling can also suppresses the component that is tipped into the longitudinal axis and which could be reintroduced to the transverse plane by a subsequent imperfect RF refocusing pulse. If the first pulse creates a longitudinal component, then a fraction of it could be brought down into the transverse plane by the second, third or even later pulses. The magnetisation can be rotated so that it combines either positively or negatively with the primary echo. Balanced spoilers can again be used to remove the effect of the longitudinal magnetisation if they are increased in amplitude at each RF pulse following a geometric progression. This will ensure that any component of longitudinal magnetisation rotated into the transverse plane will encounter a spoiling gradient greater than the one that was applied before the pulse that created it. This means that only primary echoes can contribute to the measured signal and should prevent the complex transmission of pulse errors.
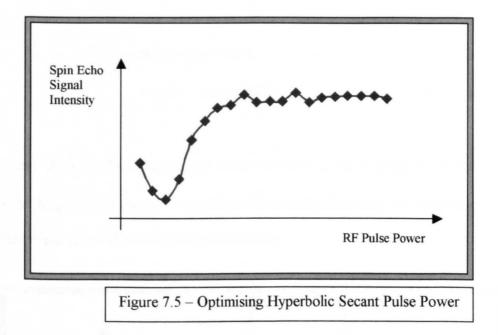
The use of spoilers can improve the measurement of the transverse relaxation time but they cannot completely correct for problems caused by imperfect inversion pulses. This is because the spoilers remove unwanted components of magnetisation from the echo chain, but do not stop the unwanted components from being created in the first place. This gives rise to additional attenuation of the echo train and the measurement of a relaxation time lower than expected. However, the echo train now becomes a relatively simple function of T_2 and θ and possible post processing correction methods have been proposed[8].

7.2.2   Improved Inversion with the Hyperbolic Secant Pulse

One way to overcome these errors is to use adiabatic inversion pulses, which are relatively insensitive to RF amplitude. Adiabatic pulses are usually used for inversion rather than refocusing. This section will show that they can be used to create a spin echo with low sensitivity to RF errors. Figure 7.4 shows a commonly used adiabatic inversion pulse known as the Hyperbolic Secant (HSC) pulse, which was first suggested by Silver et al in 1984[9].

Figure 7.4 – Hyperbolic Secant Pulse Profiles

Adiabatic pulses modulate the frequency/phase of the applied RF fields as well as the amplitude and their flip angle depends on the phase modulation, which is more easily controlled than the RF (B_1) field amplitude[10]. Adiabatic inversion pulses provide an inversion independent of the maximum B_1 field amplitude as long as the amplitude is greater than a threshold value, B_{max}. This is demonstrated by measuring the signal intensity of a single spin echo at a variety of HSC pulse powers as shown in figure 7.5.

Figure 7.5 – Optimising Hyperbolic Secant Pulse Power

The modulation function for the hyperbolic secant pulse, so called because the amplitude is modulated as a sech function and frequency modulated as a tanh function, is given in equation 7.3.

$$B_1(t) = \Omega \sec h(\beta t)^{1+i\mu} \qquad - \qquad 7.3$$

Where β and μ, the side to width parameter, are real constants that define the bandwidth of the pulse as shown in equation 7.4.

$$Bandwidth = 2\beta\mu \qquad\qquad - \qquad 7.4$$

If we make a transformation into a frame of reference that is rotating at the instantaneous frequency of the pulse[11], as shown in figure 7.6a, then the field experienced by a spin at the Larmor frequency can be determined from the following components.

$$B_1(t) = \Omega \sec h(\beta t) \qquad\qquad - \qquad 7.5$$

$$\Delta\omega(t) = -\mu\beta \tanh(\beta t) \qquad\qquad - \qquad 7.6$$

Where B_1 is the field experienced along the x-axis of the rotating frame and $\Delta\omega$ is the frequency of the pulse relative to the Larmor frequency and determines the field experienced in the longitudinal direction.
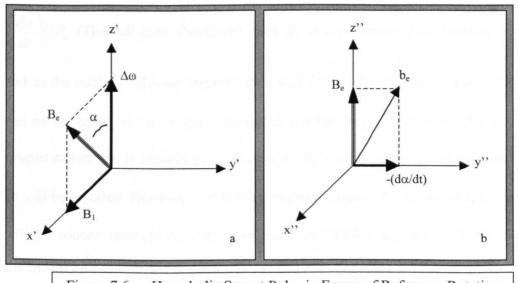
Figure 7.6a – Hyperbolic Secant Pulse in Frame of Reference Rotating at the Instantaneous Frequency of the Pulse.
Figure 7.6b – Hyperbolic Secant Pulse in Frame of Reference Where the Direction of the Effect Field, B_e, is Constant Throughout the Pulse.

The effect of these two components is to produce an effective field, B_e, that makes an angle, α, with the longitudinal axis. The effective field starts aligned along the longitudinal axis because the field is entirely made from the $\Delta\omega$ component. It then sweeps down through the transverse plane as B_1 increases until it comes to rest at the end of the pulse anti-parallel to the longitudinal direction.

If we now make a second transformation of the reference frame so that the direction of the effective field is constant throughout the pulse, as shown in figure 7.6b, we introduce a third component of the magnetic field[11]. This additional component is equal in magnitude to $\left(\dfrac{d\alpha}{dt}\right)$ and is perpendicular in direction to the effective field. The effect of this new component is to generate a new effective field, b_e. Any magnetisation that is initially parallel to b_e, and therefore B_e as they are the same at the beginning of the pulse, will precess around the effective field direction. Providing that the sweep rate of the frequency is small, i.e. $\left(\dfrac{d\alpha}{dt}\right)\langle\langle B_e$ (The Adiabatic Condition), then B_e is approximately the same as b_e and so the initially collinear magnetisation will follow B_e at all times and at the end of the pulse will be aligned anti-parallel to the longitudinal axis. Also any magnetisation that is initially perpendicular to B_e will remain perpendicular and so will be inverted. However, due to the precession around B_e, the magnetisation will be rotated through the transverse plane introducing a phase shift that is dependant on position and as such will not be refocused. This may seem to make the HSC pulse useless as a refocusing pulse, but the application of a second HSC

pulse will invert the magnetisation again, whilst at the same time adding a phase shift to cancel that introduced by the first pulse[12].

Figure 7.7 – Hyperbolic Secant Multi-Echo Sequence
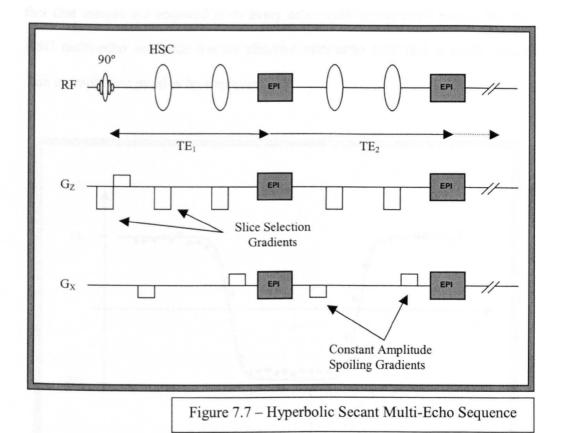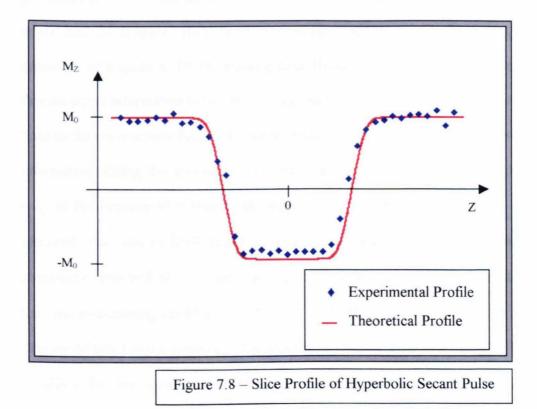
Figure 7.7 shows the simplest way to implement the use of HSC pulses in a multi-echo sequence with the substitution of HSC pulses for the sinc pulses used previously and only acquiring images after every second inversion pulse. Due to the phase shift that the pulses introduce, it is also necessary to place spoiling gradients so that they are balanced around pairs of HSC pulses rather than individual refocusing pulses. The improved inversion of the HSC pulse, as demonstrated by figure 7.8, means that the magnitude of the spoiling gradients do not need to be as large as with sinc pulses and it is sufficient to maintain the gradients at a constant level throughout the sequence rather than geometrically increasing them for successive pulses. Unfortunately it is necessary to leave a

time, T_E, between all the RF pulses to be able to form a chain of spin echoes and the minimum echo time is determined by the EPI sampling time. Therefore, the fact that images are acquired from every other echo in the chain means that the HSC multi-echo sequence has an effective inter-echo time that is much longer than a simple sinc multi-echo sequence.

Figure 7.8 – Slice Profile of Hyperbolic Secant Pulse

7.2.3 Reducing the Acquisition Time: Half Fourier Acquisition

When attempting to measure relatively short relaxation times (200-300 ms or less), the intensity in the later images will have dropped down to the level of the background noise and it will be necessary to shorten the echo times so that more accurate fitting can be achieved. This can be done in several different ways; firstly the images can be produced with half Fourier EPI techniques, thereby shortening acquisition time and hence the minimum time between echoes. Using half Fourier
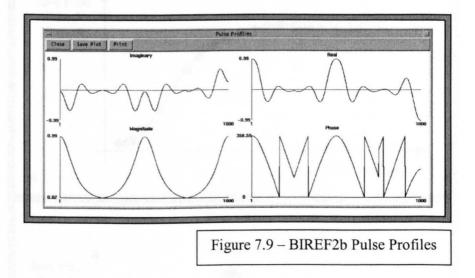
techniques it is possible to reduce the EPI data acquisition by nearly a half. In the normal EPI experiment, we collect a data matrix which is 128 by 128 elements and this provides us with a full description of k-space that enables the production of a fully resolved, 128 by 128 pixel modulus image and also a 128 by 128 pixel phase image. If we reduce the number of switched gradient cycles from 64 (2 lines per cycle) to 36, we can sample only the lower half and the first 8 lines of the upper half of k-space. Half Fourier techniques make use of the conjugate symmetry of k-space to fill the missing data. However, the problem with this is that the phase information is lost, but this can be recovered by using the central 16 lines of data in a second Fourier transform giving the low spatial frequency phase information. Using this procedure will yield the resolved image and phase data only at the expense of a loss in the signal to noise ratio (SNR) that can be achieved. The loss in SNR is not a major draw back because the shortened acquisition time will allow more images to be produced in the same amount of time and so averaging can be used to improve the SNR.

The use of half Fourier acquisition reduces the achievable echo times slightly but to allow for the measurement of relatively short relaxation times, further reductions must be made. One possibility is to acquire the data from two shorter chains, with different echo times, rather than one long chain. This will then provide twice as many data points at the lower echo times but will also double the time taken to perform the measurements.
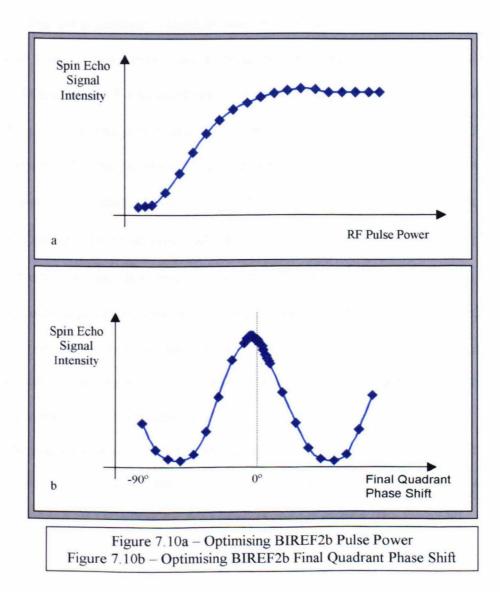
7.2.4   Reducing the Acquisition Time: BIREF Refocusing

Another way to shorten the echo times is to combine the two HSC pulses into one composite adiabatic refocusing pulse. Several pulses of this kind were suggested by Ugurbil *et al* in 1987 and are known as the BIREF (**B₁ Insensitive REF**ocusing) pulses[13]. These pulses overcome the effect of the positionally dependent phase shift that prevents the HSC pulse from refocusing, by inverting the effective field halfway through the pulse. Hence the phase shift that develops through the first half of the pulse is reversed through the second half. In particular the BIREF2b pulse, shown in figure 7.9, is particularly useful because, not only is it insensitive to B_1 inhomogeneities, but it is also slice selective and can therefore be used in a multi-slice experiment.

Figure 7.9 – BIREF2b Pulse Profiles

The BIREF2b pulse is described by the following equations.

$$
\begin{aligned}
B_1 &= \Omega \sec h(\beta t) \\
\Delta\omega &= -\mu\beta \tanh(\beta t)
\end{aligned}
\qquad 0\langle t\langle \tfrac{T}{4}
$$

$$
\begin{aligned}
B_1 &= \Omega \sec h(\beta(t - \tfrac{T}{2})) \\
\Delta\omega &= -\mu\beta \tanh(\beta(t - \tfrac{T}{2}))
\end{aligned}
\qquad \tfrac{T}{4}\langle t\langle \tfrac{3T}{4}
\qquad - \qquad 7.7
$$

$$
\begin{aligned}
B_1 &= -\Omega \sec h(\beta(t - T)) \\
\Delta\omega &= -\mu\beta \tanh(\beta(t - T))
\end{aligned}
\qquad \tfrac{3T}{4}\langle t\langle T
$$

Where β and μ are real constants that are related to the bandwidth of the pulse, as in the HSC pulse, by equation 7.4. The adiabatic nature of the BIREF2b pulse can be checked by measuring the signal intensity of a spin echo at a variety of pulse powers. Figure 7.10a shows that it is only necessary to ensure that the maximum B_1 amplitude is above a threshold level to ensure an accurate inversion. It can also be shown, by varying the phase of the final quadrant of the pulse and measuring the spin echo signal intensity, optimum performance of the pulse on the 0.5 T system described in chapter 4 is achieved with a phase shift of 5° on the final quadrant of the pulse[10]. This is demonstrated in figure 7.10b.

Figure 7.10a – Optimising BIREF2b Pulse Power
Figure 7.10b – Optimising BIREF2b Final Quadrant Phase Shift

7.3   *Experimental Method*

All scanning was performed on the 0.5 T purpose built whole body EPI scanner at the University of Nottingham described in chapter 4. The MBEST echo-planar encoding sequence was used with a switched gradient sinusoidally modulated at 0.5 KHz. Modulus images were recreated from either a 128×128 or 72×128 matrix of complex data points depending on whether full or half Fourier transform reconstruction was used.
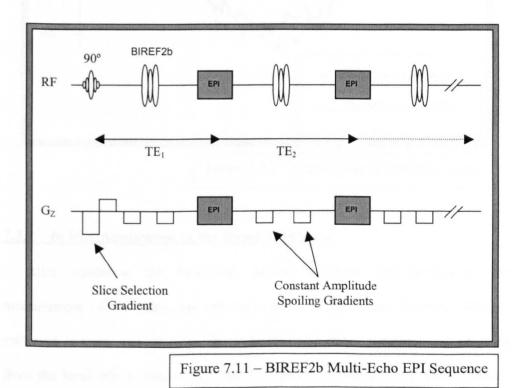
7.3.1   *In Vitro* Validation Scanning

The initial sequence validation work was carried out on a cylindrical phantom with doped water surrounding seven tubes containing varying concentrations of $CuSO_4$ solution. A sinc multi-echo sequence, shown in figure 7.3, was applied to the phantom with echo times, T_E, of 166, 332, 498 and 664 ms using a 3.5 ms duration, 90° sinc excitation pulse, and four 3.5 ms duration, 180° sinc refocusing pulses with a bandwidth of 1700 Hz. The in-plane resolution was 3.2 mm × 2.1 mm (switched × broadening gradient), the image slice thickness was 10.0 mm and the inversion slice thickness was 20.0 mm. The sequence was applied five times and each application consisted of 10 repetitions with a repetition time, T_R, of 15 s. The results of this sequence were validated against a single spin echo EPI sequence using the same echo times and repetition time. Again 10 repetitions were taken for each of 5 applications.

The experiments were then repeated using the HSC multi-echo sequence shown in figure 7.7, with echo times of 74, 293, 512 and 731 ms and using pairs of hyperbolic secant pulses for the inversion and refocusing. The hyperbolic secant pulses were 7 ms in duration with a bandwidth of 1700 Hz. The slice thickness of
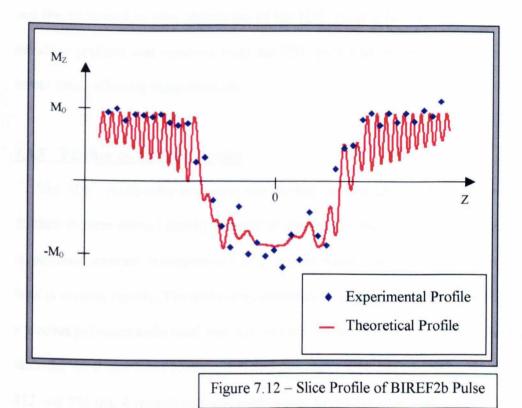
the HSC pulses was 20.0 mm and the side to width parameter, μ, was 2. Half Fourier reconstruction was used to produce the images and the results were validated against the single spin echo measurements described above. The temperature during all of the experiments was monitored and maintained at $20.6 \pm 0.2\ °C$.

The experiments were then repeated once more with a multi-echo sequence as shown in figure 7.11, using single BIREF2b pulses to refocus and echo times of 170, 340, 510, 680 ms. The BIREF2b pulses were 7 ms in duration with a bandwidth of 2300 Hz and a side to width parameter, μ, of 3.

Figure 7.11 – BIREF2b Multi-Echo EPI Sequence

No slice selection gradient was used on the BIREF2b pulses due to a poor slice selective performance as shown by the slice profile in figure 7.12. Full MBEST reconstruction methods were used and the results were again validated against a

single spin echo sequence with the same echo times as the BIREF2b multi-echo sequence. In both cases, 10 repetitions were taken for each of 5 applications and the temperature was maintained at 19.4±0.2 °C.

Figure 7.12 – Slice Profile of BIREF2b Pulse

7.3.2 *In Vivo* Application in the Human Placenta

After validation the hyperbolic secant sequence was applied in the measurement of the transverse relaxation time of the human placenta. Written, informed consent was given by the volunteer and ethics approval was obtained from the local ethics committee at the City Hospital, Nottingham. The volunteer was recruited on the basis of an uncomplicated pregnancy at 32 weeks gestation during a routine examination. A standard ultrasound examination and a transverse multi-slice set of images were initially obtained to allow for localisation of the placenta and selection of a slice adjacent to the position of umbilical cord insertion. The HSC multi-echo sequence was then applied ($T_R = 15$ s; $T_E = 74$,

293, 512, and 731 ms; 4 repetitions) with an in-plane resolution of 3.5 mm × 2.5 mm (switched × broadening gradient). The results were validated with a standard single spin echo sequence with the same parameters as the HSC sequence. For this and the additional *in vivo* application of the HSC multi-echo sequence, the slice selection gradient was removed from the HSC pulses to minimise measurement errors from inflowing magnetisation.

7.3.3 Further *In Vivo* Application

The HSC multi-echo sequence was further applied in the study of gastric dilution in three normal healthy subjects to demonstrate the ability of the sequence to produce accurate measurements in a system where the transverse relaxation time is varying rapidly. The multi-echo sequence was initially applied, *in vitro*, on a viscous polysaccharide meal and then, *in vivo*, on the volunteers at various times after the meal had been consumed. The HSC multi-echo sequence (T_E=74, 293, 512 and 731 ms; 4 repetitions) was applied and a repetition time of 10 s was used to shorten the experiment time. The number and time of the *in vivo* measurements varied depending on the rate of digestion of the particular subject. Validation was carried out on the first volunteer using a single spin echo sequence (T_R = 10 s; T_E=60, 80, 100, 120, 140, 220, 380, 700 ms; 2 repetitions) once *in vitro* and once *in vivo*.

Subsequently the BIREF2b multi-echo sequence was applied on one normal healthy subject (T_R=30 s; T_E=180, 360, 540, 720 ms; 4 repetitions) to study the effect of Gaviscon® Liquid antacid (Reckitt Benckiser Healthcare Ltd, Hull, UK) on an acidic lemon juice preparation. The sequence was initially validated with a single sinc spin echo sequence *in vitro* and *in vivo* by measuring the transverse
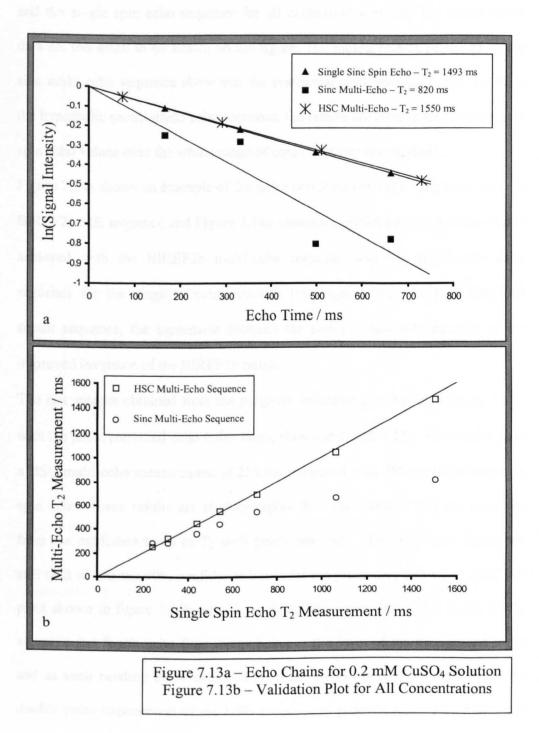
relaxation time of the lemon juice at 37 °C. The BIREF2b multi-echo sequence was then used to monitor the production of an alginate raft of Gaviscon® on the surface of the lemon juice.

7.3.4   Analysis

For all validation experiments, the transverse relaxation time was obtained by measuring the average signal intensity in a selected region of interest within the phantom and correcting the measured value to compensate for the noise in the magnitude signal using a look up table[14]. This compensation is necessary due to the effect of the formation of a magnitude image on background noise. Signals uniformly distributed about zero in the complex data are transformed to being positive in a magnitude image. The corrected values were then averaged over the repetitions and equation 2.26 was fitted to the logarithm of the averaged data using a linear weighted fit to provide a measure of the transverse relaxation time[15]. In the placental application, the transverse relaxation times were obtained from a region of interest that encompassed the whole of the placenta using the same fitting procedure as before. A similar method of analysis was used to obtain a result for the relaxation time in the gastric studies, with the region of interest being selected to cover the whole of the stomach. In one of the gastric study volunteers, a T_2 map was generated by carrying out the fitting process on a pixel-by-pixel basis in the region of interest selected and overlaying the results on an anatomical image. The BIREF2b *in vivo* data was analysed in the same manner as that with the HSC sequence. T_2 maps were also generated of the lemon juice validation scans and the Gaviscon® raft.

7.4 Experimental Results

Figure 7.13a shows an example of the noise corrected echo-trains acquired with the sinc multi-echo sequence, the hyperbolic secant multi-echo sequence and the single spin echo validation sequence.

a

b

Figure 7.13a – Echo Chains for 0.2 mM CuSO$_4$ Solution
Figure 7.13b – Validation Plot for All Concentrations

It can be seen that the sinc multi-echo data provides a very poor fit to an exponential decay. The hyperbolic secant multi-echo data shows much better agreement with the single spin echo data. Figure 7.13b shows a comparison between the T_2 measurements from the sinc and HSC multi-echo pulse sequences and the single spin echo sequence for all calibration samples. The errors in the data are too small to be shown on the figure. The measurements produced by the sinc multi-echo sequence show that the systematic error increases with T_2. With the hyperbolic secant multi-echo sequence, the results are comparable to the single spin echo values over the whole range of concentrations investigated.

Figure 7.14a shows an example of the noise corrected echo-train acquired with the BIREF2b ME sequence and Figure 7.14b shows a comparison between the results achieved with the BIREF2b multi-echo sequence and the single spin echo sequence for the range of concentrations investigated. As with the hyperbolic secant sequence, the agreement between the two is reasonable because of the improved inversion of the BIREF2b pulse.

The raw images obtained from the pregnant volunteer are shown in figure 7.15a, with the noise corrected echo trains being shown in figure 7.15b. The results yield a HSC multi-echo measurement of 256 ms compared with 265 ms from the single spin echo. These results are slightly higher than the value of 210 ms predicted from the published trend of T_2 with gestational age[1]. However, both results are still well within the 90% confidence limits for the previously published data. The plots shown in figure 7.15b only show three data points each. This is due to the signal in the fourth echo time image being at the level of the background noise and as such needing to be excluded from the fit. As previously mentioned, the double pulse requirement of the HSC sequence to produce refocusing makes the

inter echo spacing unacceptably long for measuring transverse relaxation times of the order of 200-300 ms.
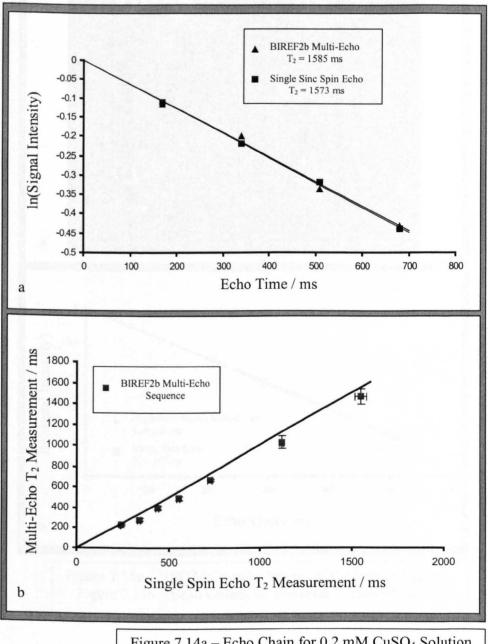
Figure 7.14a – Echo Chain for 0.2 mM CuSO$_4$ Solution
Figure 7.14b – Validation Plot for All Concentrations

Figure 7.15a – HSC Multi-Echo Images of the Human Placenta
Figure 7.15b – Echo Chains for Placental Region of Interest
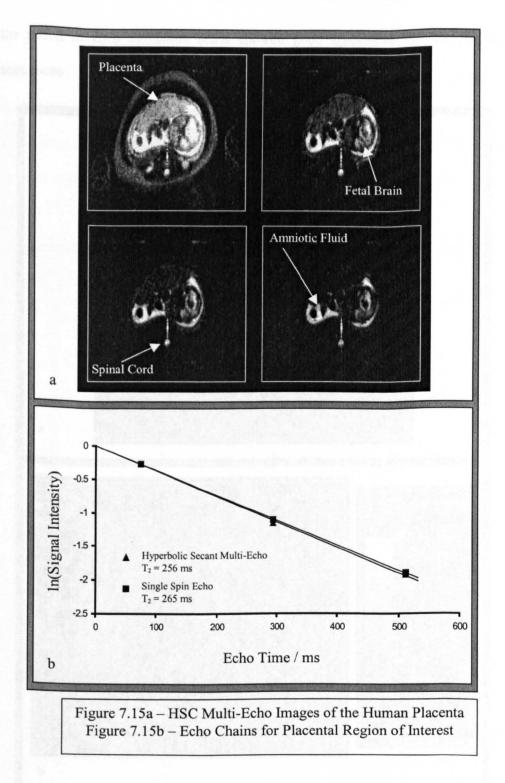
Figure 7.16a shows the raw images of the polysaccharide meal *in vivo* at each of

the echo times and figure 7.16b shows a T_2 map of the meal in the stomach. All of

the initial *in vitro* validation scans showed good agreement between the two sequences.
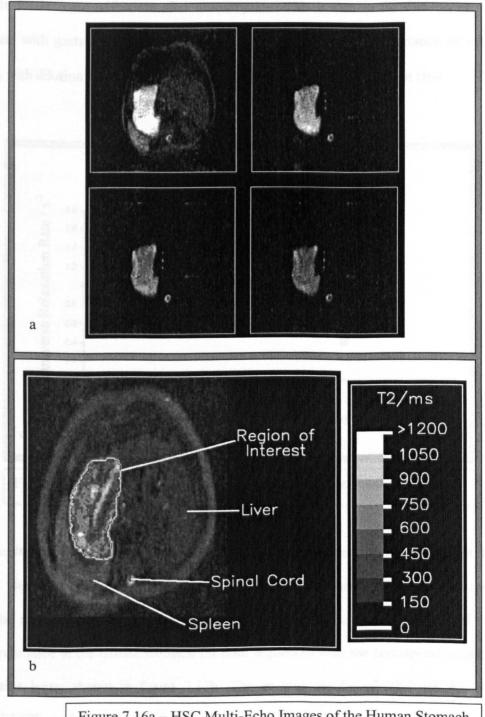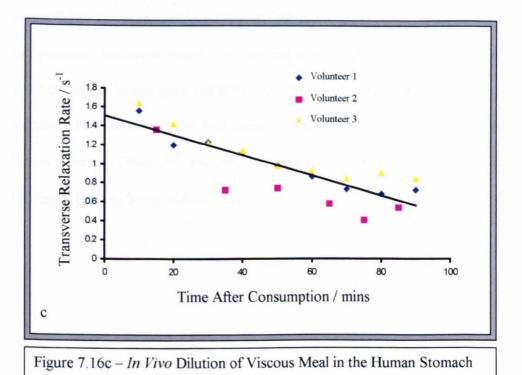
Figure 7.16a – HSC Multi-Echo Images of the Human Stomach
Figure 7.16b – T_2 Map of Viscous Meal in the Human Stomach
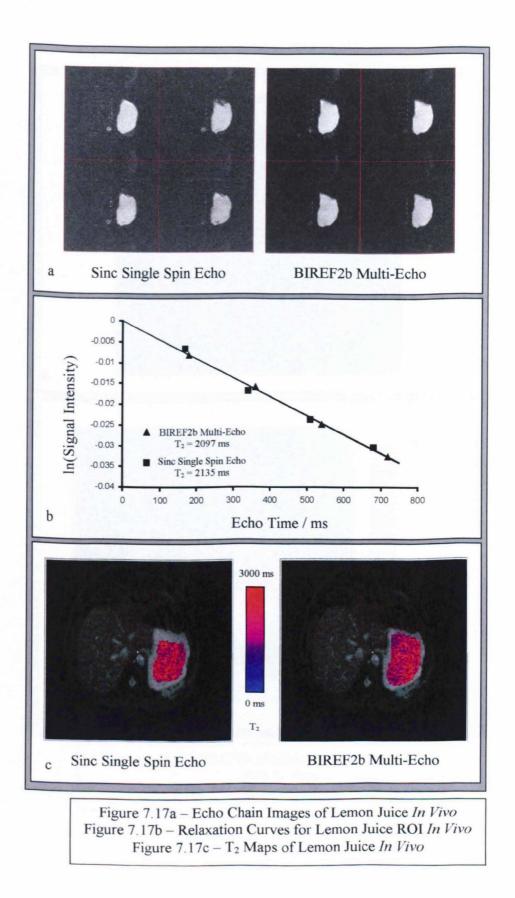
Figure 7.16c shows all of the results obtained *in vivo* with the HSC-ME sequence for the three subjects. A general trend can be seen for the transverse relaxation rate to decrease with time after consumption. This is due to the dilution of the meal with gastric secretions and, after careful calibration of the variation of meal T_2 with dilution *in vitro*, allows for measurement of gastric dilution *in vivo*.

Figure 7.16c – *In Vivo* Dilution of Viscous Meal in the Human Stomach
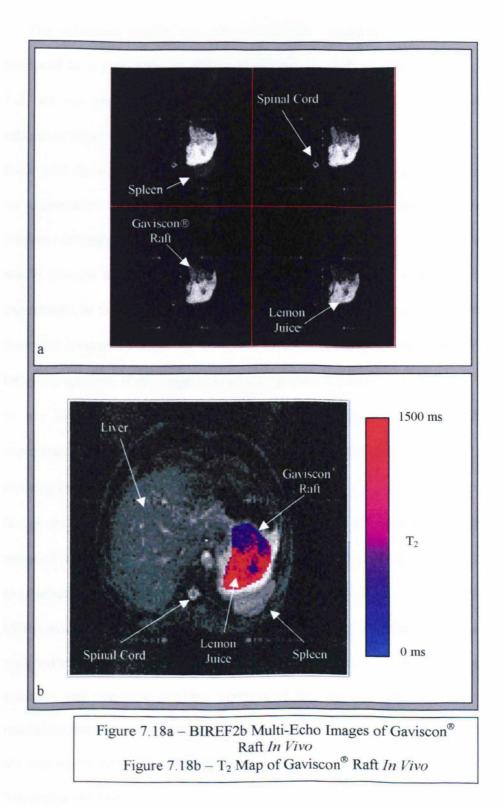
The *in vitro* validation of the BIREF2b multi-echo sequence on lemon juice at 37 °C yielded a multi-echo measurement of 2233 ms compared to a single sinc spin echo measurement of 2227 ms. Figure 7.17a shows the raw *in vivo* images of the lemon juice in the human stomach for both sequences with the corresponding echo chains being shown in figure 7.17b. The *in vivo* results of 2097 ms for the BIREF2b multi-echo measurement and 2135 ms for the single sinc spin echo sequence are in good agreement with one another and with the *in vitro* data. The slight reduction in the two values may be due to dilution effects with any gastric

secretions. The *in vivo* single spin echo measurement was made before the multi-echo measurement, possibly explaining the slight difference between the two values. Figure 7.17c contains T_2 maps for the two sequences indicating the comparability of the two. However, it is necessary to reduce the size of the ROI in the production of the single spin echo map due to movement between the images, a problem that may limit the accuracy of the technique as well.

Figure 7.18a shows an example of the BIREF2b multi-echo images of the alginate raft produced on top of lemon juice by Gaviscon® liquid. A T_2 measurement of 1377 ms for the lemon juice and 438 ms for the raft demonstrates the ability of the sequence to differentiate the two layers. Figure 7.18b shows a T_2 map of the lemon juice and Gaviscon® allowing the presence of some developing raft within the lemon juice to be identified.

a   Sinc Single Spin Echo   BIREF2b Multi-Echo

Legend in plot:
▲ BIREF2b Multi-Echo
   $T_2 = 2097$ ms
■ Sinc Single Spin Echo
   $T_2 = 2135$ ms

b

c   Sinc Single Spin Echo   BIREF2b Multi-Echo

Figure 7.17a – Echo Chain Images of Lemon Juice *In Vivo*
Figure 7.17b – Relaxation Curves for Lemon Juice ROI *In Vivo*
Figure 7.17c – T_2 Maps of Lemon Juice *In Vivo*

Figure 7.18a – BIREF2b Multi-Echo Images of Gaviscon®
Raft *In Vivo*
Figure 7.18b – T$_2$ Map of Gaviscon® Raft *In Vivo*

7.5 Discussion

The validation studies have shown that the imperfections in the inversion produced by a sinc pulse, as shown by the poorly defined slice profile in figure 7.2, are too great to allow for the accurate measurement of the transverse relaxation time in a multi-echo sequence.

Even with the use of spoiling gradients the decay curve produced is a poor fit to an exponential form due to the complex way the magnetisation components progress through the echo train. It would be expected that the spoiling gradients would prevent this complex pattern of echo amplitudes and would provide an exponential fit that yields a lower than expected value for the relaxation time. This does not happen because the inversion errors are too great to overcome with balanced spoilers. If the magnitude of the spoilers is increased further they begin to act like the pulsed gradients in a Pulsed Gradient Spin Echo (PGSE) experiment. This leads to diffusion weighting in the images and further errors entering the experiment.

It was observed that without the slice selection on the 180° refocusing pulses, the effect of the pulse errors was not as great and the spoiling gradients were adequate to produce an exponentially decaying echo train. However, each pulse in the train still provides an incomplete inversion and as such the T_2 value produced is an underestimate of the true value as demonstrated by figure 7.19. With both the slice selective and non-slice selective versions of the sequence the deviation of the relaxation time measurement away from the single spin echo value increases with the relaxation time. This finding is in agreement with the work described by Majumdar and Gore[16].

Figure 7.19 – Echo Chains for 0.2 mM CuSO$_4$ Solution Using a Single Sinc Spin Echo Sequence and a Non-Slice Selective Sinc Multi-Echo Sequence

The validation data shows that the use of improved inversion pulses, either HSC or BIREF2b, allows for a much more accurate measurement due to the fact that errors have been prevented from entering the sequence. The slice profiles of the HSC and BIREF2b pulses shown in figures 7.8 and 7.12 highlight the excellent inversion ability of these pulses on resonance. However, figure 7.12 also highlights the poor slice selective ability of this implementation of the BIREF2b pulse and explains the need to apply the BIREF2b sequence without slice selective gradients.

Both pulses provide very good inversion but they also have their disadvantages. The use of two hyperbolic secant pulses to create a refocusing pulse lengthens the acquisition and limits the measurable echo times. This means that the measurement of short T$_2$ values becomes less accurate. The use of half Fourier

acquisition techniques improves the limitations but, due to the fact that even the echoes that are not sampled must be allowed time to refocus, the improvement is restricted to shortening the first echo time. The HSC-ME sequence would therefore need to be applied twice, with different echo times, when studying samples with relatively short relaxation times. The use of the BIREF2b pulse should shorten the measurable echo times but does encounter problems with the required RF amplitude needed to produce an inversion. When used with EPI, there is not a problem from an energy deposition point of view but the BIREF2b pulse can be difficult to implement on current hardware. This is a problem that may be overcome with the implementation of the VERSE principle to reduce RF power levels through the use of time varying gradients[17].

The brief examples presented here show that both the multi-echo sequences are capable of producing accurate measurements of T_2 *in vivo* in a considerably shorter time than has previously been possible. The application of the HSC sequence in the measurement of the transverse relaxation time of the human placenta shows that it is possible to accurately measure T_2 in an organ that is prone to unpredictable and non-periodic motions. The application of the HSC sequence in a series of healthy volunteers to study gastric dilution, showed the potential use of the multi-echo sequence as a dynamic measurement tool for the study of processes that are varying in the time frame unreadable by previous T_2 measurement techniques. This is further emphasised with the application of the BIREF2b sequence in the study of alginate raft production used in antacid preparations, where the rate of change of T_2 will provide information about the rate of raft formation.

7.6   Conclusion

The results discussed above have shown that the combination of a multi-echo sequence with EPI image acquisition can be used to produce rapid and accurate measurements of the transverse relaxation time. The use of sinc pulses does not provide sufficient refocusing to prevent unwanted components of magnetisation from being created. The complex nature of these components causes a poor fit to an exponential form and an underestimate of the T_2 value. The use of HSC or BIREF2b pulses produces a more accurate inversion and a better estimate of the relaxation time.

The HSC and BIREF2b versions of the multi-echo sequence have been applied *in vivo* and have been shown to produce results that compare well with previous data and with a single spin echo EPI sequence. The application in the human placenta shows the ability of the sequence to produce accurate quantitative results in an organ that suffers from random motions. The application in the study of gastric dilution and alginate raft formation indicates the potential of the technique as a dynamic measurement tool in the study rapidly varying transverse relaxation times.

References

[1] Gowland, P.A., et al., *In vivo relaxation time measurements in the human placenta using echo planar imaging at 0.5 T.* Magnetic Resonance Imaging, 1998. **16**(3): p. 241-247.

[2] Marciani, L., et al., *Gastric response to increased meal viscosity assessed by echo-planar magnetic resonance imaging in humans.* Journal of Nutrition, 2000. **130**(1): p. 122-127.

[3] Marciani, L., et al., *Echo-planar imaging relaxometry to measure the viscosity of a model meal.* Journal of Magnetic Resonance, 1998. **135**(1): p. 82-86.

[4] Carr, H.Y. and E.M. Purcell, *Effects of Diffusion on Free Precession in Nuclear Magnetic Resonance Experiments.* Physical Review, 1954. **94**(3): p. 630-639.

[5] Majumdar, S., et al., *Errors in the Measurements of T2 Using Multiple-Echo Mri Techniques .1. Effects of Radiofrequency Pulse Imperfections.* Magnetic Resonance in Medicine, 1986. **3**(3): p. 397-417.

[6] Gadian, D.G., *NMR and its Applications to Living Systems.* 2nd ed. 1995: Oxford University Press. 283.

[7] Zur, Y., et al., *A Phase-Cycling Technique for Cancelling Spurious Echoes in NMR Imaging.* Journal of Magnetic Resonance, 1987. **71**: p. 212-228.

[8] Majumdar, S., et al., *An Estimation and Correction Scheme for System Imperfections in Multiple-Echo Magnetic-Resonance-Imaging.* Magnetic Resonance in Medicine, 1987. **4**(3): p. 203-220.

[9] Silver, M.S., R.I. Joseph, and D.I. Hoult, *Highly Selective Pi/2 and Pi-Pulse Generation.* Journal of Magnetic Resonance, 1984. **59**(2): p. 347-351.

[10] Gowland, P.A., *The Accurate Measurement of Nuclear Magnetic Resonance Parameters In Vivo - Ph.D. Thesis,* in *Physics.* 1990, University of London.

[11] Ugurbil, K., M. Garwood, and M.R. Bendall, *Amplitude-Modulated and Frequency-Modulated Pulses to Achieve 90-Degrees Plane Rotations with Inhomogeneous-B1 Fields.* Journal of Magnetic Resonance, 1987. **72**(1): p. 177-185.

[12] Conolly, S., et al., *A Reduced Power Selective Adiabatic Spin-Echo Pulse Sequence.* Magnetic Resonance in Medicine, 1991. **18**(1): p. 28-38.

[13] Ugurbil, K., et al., *Amplitude-Modulated and Frequency Phase-Modulated Refocusing Pulses That Induce Plane Rotations Even in the Presence of Inhomogeneous B1 Fields.* Journal of Magnetic Resonance, 1988. **78**(3): p. 472-497.

[14] Henkelman, R.M., *Measurement of Signal Intensities in the Presence of Noise in Mr Images.* Medical Physics, 1985. **12**(2): p. 232-233.

[15] Press, W.H., et al., *Numerical Recipes in C.* 2nd ed. 1993: Cambridge University Press.

[16] Majumdar, S. and J.C. Gore, *Effects of Selective Pulses on the Measurement of T2 and Apparent Diffusion in Multiecho Mri.* Magnetic Resonance in Medicine, 1987. **4**(2): p. 120-128.

[17] Conolly, S., et al., *Variable-Rate Selective Excitation.* Journal of Magnetic Resonance, 1988. **78**(3): p. 440-458.

[18] Bakker, C.J.G., C.N. Degraaf, and P. Vandijk, *Derivation of Quantitative Information in Nmr Imaging - a Phantom Study.* Physics in Medicine and Biology, 1984. **29**(12): p. 1511-1525.

[19] Barker, G.J. and T.H. Mareci, *Suppression of Artifacts in Multiple-Echo Magnetic-Resonance.* Journal of Magnetic Resonance, 1989. **83**(1): p. 11-28.

[20] Bendall, M.R., et al., *Adiabatic Refocusing Pulse Which Compensates for Variable Rf Power and Off-Resonance Effects.* Magnetic Resonance in Medicine, 1987. **4**(5): p. 493-499.

[21] Conolly, S., D. Nishimura, and A. Macovski, *Sweep-Diagram Analysis of Selective Adiabatic Pulses.* Journal of Magnetic Resonance, 1989. **83**(3): p. 549-564.

[22] Crawley, A.P. and R.M. Henkelman, *Errors in T2 Estimation Using Multislice Multiple-Echo Imaging.* Magnetic Resonance in Medicine, 1987. **4**(1): p. 34-47.

[23] Does, M.D. and J.C. Gore, *Complications of nonlinear echo time spacing for measurement of T-2.* Nmr in Biomedicine, 2000. **13**(1): p. 1-7.

[24] Does, M.D. and R.E. Snyder, *Multiecho imaging with suboptimal spoiler gradients.* Journal of Magnetic Resonance, 1998. **131**(1): p. 25-31.

[25] Hahn, E.L., *Spin Echoes.* Physical Review, 1950. **80**(4): p. 580-594.

[26] Kunz, D., *Frequency-Modulated Radiofrequency Pulses in Spin-Echo and Stimulated-Echo Experiments.* Magnetic Resonance in Medicine, 1987. **4**(2): p. 129-136.

[27] Majumdar, S., et al., *Errors in the Measurements of T2 Using Multiple-Echo Mri Techniques .2. Effects of Static-Field Inhomogeneity.* Magnetic Resonance in Medicine, 1986. **3**(4): p. 562-574.

[28] McKenzie, C.A., et al., *Fast acquisition of quantitative T-2 maps*. Magnetic Resonance in Medicine, 1999. **41**(1): p. 208-212.

[29] Mulkern, R.V., et al., *Cpmg Imaging Sequences for High-Field Invivo Transverse Relaxation Studies*. Magnetic Resonance in Medicine, 1990. **16**(1): p. 67-79.

[30] Ordidge, R.J., et al., *Frequency offset corrected inversion (FOCI) pulses for use in localized spectroscopy*. Magnetic Resonance in Medicine, 1996. **36**(4): p. 562-566.

[31] Payne, G.S. and M.O. Leach, *Implementation and evaluation of frequency offset corrected inversion (FOCI) pulses on a clinical MR system*. Magnetic Resonance in Medicine, 1997. **38**(5): p. 828-833.

[32] Poon, C.S. and R.M. Henkelman, *Practical T2 Quantitation for Clinical-Applications*. Jmri-Journal of Magnetic Resonance Imaging, 1992. **2**(5): p. 541-553.

[33] Rosenfeld, D. and Y. Zur, *Is the sech/tanh adiabatic pulse really adiabatic?* Journal of Magnetic Resonance, 1998. **132**(1): p. 102-108.

[34] Santyr, G.E., et al., *Off-Resonance Spin Locking for Mr-Imaging*. Magnetic Resonance in Medicine, 1994. **32**(1): p. 43-51.

[35] Stables, L.A., R.P. Kennan, and J.C. Gore, *Asymmetric spin-echo imaging of magnetically inhomogeneous systems: Theory, experiment, and numerical studies*. Magnetic Resonance in Medicine, 1998. **40**(3): p. 432-442.

[36] Tannus, A. and M. Garwood, *Adiabatic pulses*. Nmr in Biomedicine, 1997. **10**(8): p. 423-434.

[37] Town, G. and D. Rosenfeld, *Analytic Solutions to Adiabatic Pulse-Modulation Functions Optimized for Inhomogeneous-B1 Fields*. Journal of Magnetic Resonance, 1990. **89**(1): p. 170-175.

[38] Ugurbil, K., M. Garwood, and A.R. Rath, *Optimization of Modulation Functions to Improve Insensitivity of Adiabatic Pulses to Variations in B1 Magnitude*. Journal of Magnetic Resonance, 1988. **80**(3): p. 448-469.

[39] Yongbi, M.N., C.A. Branch, and J.A. Helpern, *Perfusion imaging using FOCI RF pulses*. Magnetic Resonance in Medicine, 1998. **40**(6): p. 938-943.

8   Quantification of Magnetisation Transfer

8.1   Introduction

Magnetisation Transfer (MT) is frequently used as a simple source of contrast due to the different effect it has on tissues depending on the relative proportions of free and bound protons contained within them. It is often implemented in Magnetic Resonance Angiography (MRA) to suppress the signal from tissue to highlight blood in vessels[1]. However, if MT is to be used to its full potential it is necessary for quantitation to be carried out.

Much of the original work on magnetisation transfer involved the calculation of the magnetisation transfer ratio (MTR), which is a ratio of the signal intensities from images that are produced with and without saturation of the bound protons. Although quantitative, MTR is dependant on the details of the pulse sequence used and the imaging hardware. Also, MTR can be affected by changes in the relaxation times of the pools as well as the magnetisation transfer exchange rates. To produce any thorough quantitative experiment, it is necessary to first model the magnetisation transfer process and then design the experiment around this model.

Many groups have recently attempted to model the magnetisation transfer process. Henkelman *et al* used a two-pool model to describe magnetisation transfer by solving the Bloch equations in the steady state[2]. Others, including Sled[3,4], Lee[5], Chai[6] and Gochberg[7], have followed the work of Henkelman making changes to both the model used and the experimental technique. Sled *et al* used the Bloch equations to describe the free proton pool and then modelled the bound proton pool using the Redfield-Provotorov theory. The experimental technique employed by Sled *et al* also differed from Henkelman's work through the use of pulsed off-resonance irradiation. In comparison Gochberg *et al* used an experiment that

saturated the bound proton pool with successive inversions of the free proton pool. In this chapter, I have built on the model suggested by Henkelman *et al* and applied it with the aim of quantifying the size and the transverse relaxation time of the bound proton pool in a clinically feasible time.

A problem with many of the original magnetisation transfer experiments was the continuous wave (CW) RF energy used to produce saturation of the bound proton pool. Many MRI scanners cannot apply RF energy continuously, and the high levels of energy deposition, and hence sample heating, will limit CW experiments in those that can. More recently, magnetisation transfer has been investigated using chains of pulses, either on resonance with binomial pulses or off resonance. Following the work proposed by Ranjeva *et al*[8], who produced a sequence to yield MTR images of the human brain, I have combined a chain of off-resonance pulses with EPI to produce a rapid imaging sequence with relatively low energy deposition.

The aim of this work is to further our understanding of a result previously mentioned in chapter 7. It has been shown that the transverse relaxation time of the human placenta decreases through the gestational period and is generally reduced in pregnancies complicated by IUGR and Pre-Eclampsia[9]. It has also been shown that this is the case with the longitudinal relaxation time but with a lower significance to the gestational age trend and a more significant difference with compromised pregnancies. These differences could be due to structural changes that alter water binding or movement within the placenta or may be due to changes in the macromolecular concentration. Alteration of the transverse relaxation time may also be linked to changes in the oxygenation level of blood flowing in the placenta. It is postulated that the ability to quantify the size of the

bound proton pool within the placenta as a function of gestational age will provide further information allowing a deeper understanding of the variation in the relaxation times.

8.2 Theory

The model consists of two pools of protons, M^A (free protons) and M^B (bound protons) with initial longitudinal magnetisations M_{A0} and M_{B0} respectively. The pools relax with relaxation parameters R_A, R_B, T_{2A} and T_{2B}, and exchange between the pools is described by the rate constant R_X. As such the modified Bloch equations describing the system can be written as follows[2]:
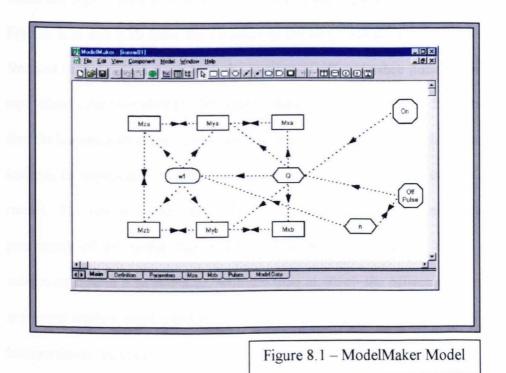
$$\frac{dM_z{}^A}{dt} = R_A\left(M_{A0} - M_z{}^A\right) - R_X M_{B0} M_z{}^A + R_X M_{A0} M_z{}^B + \omega_1{}^x M_Y{}^A \qquad - 8.1$$

$$\frac{dM_z{}^B}{dt} = R_B\left(M_{B0} - M_z{}^B\right) - R_X M_{A0} M_z{}^B + R_X M_{B0} M_z{}^A + \omega_1{}^x M_Y{}^B \qquad - 8.2$$

$$\frac{dM_X{}^{A,B}}{dt} = -\left(M_X{}^{A,B}\Big/ T_2{}^{A,B}\right) - 2\pi\Delta M_Y{}^{A,B} \qquad - 8.3$$

$$\frac{dM_Y{}^{A,B}}{dt} = -\left(M_Y{}^{A,B}\Big/ T_2{}^{A,B}\right) + 2\pi\Delta M_X{}^{A,B} - \omega_1{}^x M_z{}^{A,B} \qquad - 8.4$$

Where the subscripts X,Y,Z indicate the x,y,z components of the magnetisation and the superscripts A,B refer to the free and the bound proton pool respectively. Δ is the frequency offset of the applied RF pulses and $\omega_1{}^x$ is a term describing the

shape and power of the pulses. Many other models have suggested the use of separate rate constants, k_{AB} and k_{BA}, to describe the exchange from pool A to B and from pool B to A. However, this model follows the Henkelman model in the use of a single rate constant, R_X, which is weighted to the relative sizes of the two pools. This allows the two relative pool sizes to be investigated and also ensures that equilibrium conditions are satisfied.

Figure 8.1 – ModelMaker Model

8.2.1   The ModelMaker Model
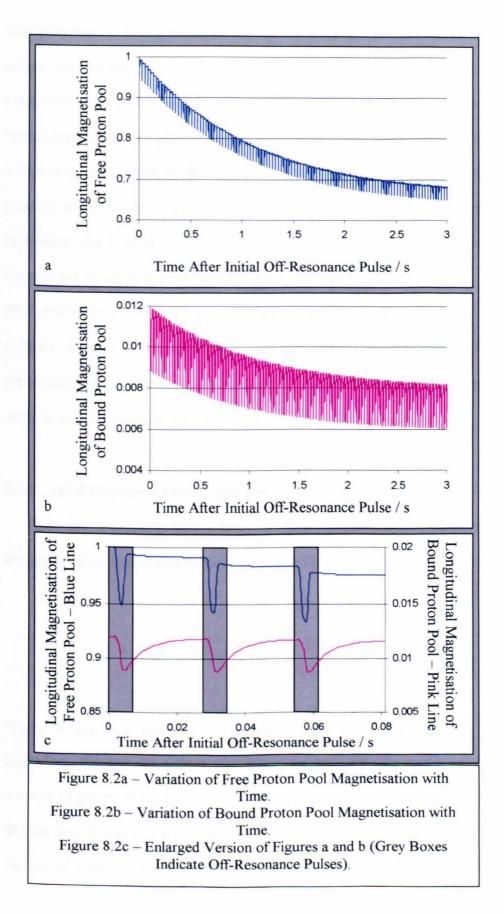
From these equations, a multi-compartmental model was set up within ModelMaker (Cherwell Scientific) to determine the relationship between the measured values of M_A and the saturation of M_B caused by the application of off-resonance pulses[10]. This is achieved by solving the modified Bloch equations numerically in an iterative process using a Runge-Kutta integration method. The model, shown in figure 8.1, contains six compartments to illustrate the one

longitudinal and two transverse components contained within both of the proton pools. The links between the various components describe the magnetisation transfer and relaxation properties of the two pools, as well as the effect that the application of a chain of off-resonance pulses will have on their magnetisation. This leads to a completed model that is fully described by the eight parameters (ω_1^x, Δ, M_{A0}, M_{B0}, R_X, R_A, R_B, T_{2A} and T_{2B}) of equations 8.1 – 8.4. The relative effect and significance of each of these are discussed in the following sections.

Figures 8.2a and 8.2b show the variation in the longitudinal magnetisation of the free and bound proton pools with the number of off-resonance pulses applied or equivalently the time after the first off-resonance pulse was applied. It can be seen that the longitudinal magnetisation of both pools decreases through the experiment towards an asymptotic value that is determined by the various parameters of the model. The rate at which this value is approached is also dependant on the parameters of the model. Figure 8.2c shows an enlarged version of the initial section of figures 8.2a and 8.2b, with the time at which the off-resonance pulses are being applied highlighted in grey. The effect of the off-resonance pulses on both pools can be seen.

Figure 8.2a – Variation of Free Proton Pool Magnetisation with Time.

Figure 8.2b – Variation of Bound Proton Pool Magnetisation with Time.

Figure 8.2c – Enlarged Version of Figures a and b (Grey Boxes Indicate Off-Resonance Pulses).

The free proton pool magnetisation is reduced by a small amount even though the pulses are applied 2000 Hz off-resonance and the bound proton pool magnetisation is significantly decreased. During the interval between pulses, the bound proton pool magnetisation recovers longitudinal magnetisation through exchange processes with the free proton pool and to a much lesser extent, through longitudinal relaxation. Conversely the free proton pool magnetisation continues to decrease due to losses to the bound proton pool that are more significant than the recovery of magnetisation through relaxation processes.

This section has provided a broad overview of the model used and the following sections describe in detail the different components of the model. Before proceeding with any experimental work, the model was thoroughly tested and investigated by simulating the effects of changes in the model parameters.

8.2.2   Off-Resonance Pulse Description

Gaussian windowed sinc pulses are used to provide the off-resonance irradiation of the bound proton pool in the model as described by equation 8.5.

$$\omega_1{}^x = RF_{AMP} \frac{\sin(\beta t)}{\beta t} e^{\left(\frac{-t}{A}\right)^2} \qquad - \qquad 8.5$$

Where RF_{AMP} is a measure of the pulse amplitude, β describes the pulse bandwidth (500 Hz) and A is a constant that determines the form of the Gaussian window of the pulse (0.002 s^{-1}). This description of the pulses used is included directly into the model via the parameter $\omega_1{}^x$ as a time dependant variable. All of the variables describing the pulses are set as they are for their implementation on

the scanner with the exception of the pulse amplitude. The amplitude of the pulse is programmed into the scanner so that it is set relative to the size of a 180° sinc pulse, which is in turn calibrated each time the scanner is set up by ensuring complete inversion of the equilibrium magnetisation of the sample being studied. The value of RF_{AMP} used in the model is set in a similar manner by constructing a second model in ModelMaker (Cherwell Scientific) that only contains one proton pool. In this second implementation of the model a single 180° sinc pulse is applied on-resonance and the value of RF_{AMP} is altered until a complete inversion of the longitudinal magnetisation is achieved. The value of RF_{AMP} in the magnetisation transfer model is then set by multiplying this value by the relative difference in amplitude between the 180° sinc pulse and the Gaussian windowed sinc pulse. The only other parameter of the model that describes the off-resonance pulses is Δ, the off-resonance frequency. This is simply entered into the model at the frequency offset as set on the scanner.

8.2.3   Relative Pool Sizes

As mentioned in the introduction, the model proposed by Henkelman differs from many others in the use of a single exchange rate to describe transfer of magnetisation between the pools. The weighting of this single rate constant to the size of the pools allows for simple achievement of the equilibrium state. From equation 8.1 we can see that in the equilibrium state (when $M_z^A = M_{A0}$ and $M_z^B = M_{B0}$), the two exchange terms cancel out and equilibrium is maintained. This is also true for equation 8.2. As the aim of this work is to investigate the relative sizes of the two proton pools, the model can be simplified by setting the size of

the free proton pool to unity ($M_{A0} = 1$) and examining any variation in the relative size of the bound proton pool, M_{B0}.
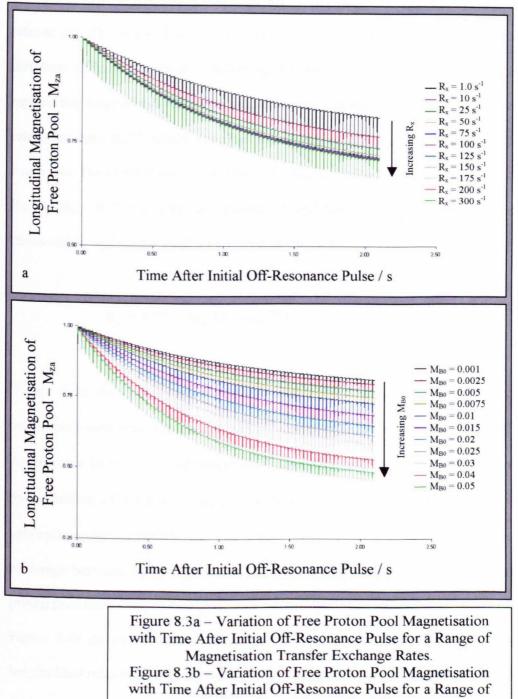
Variations in M_{B0} and R_X were simulated individually by setting all other parameters to those defined by the experimental hardware or quoted by Henkelman[2] for a 4% concentration agar gel phantom studied when using a 0.6 T system. These values are detailed below in table 8.1.

Model Parameter	Value Used in Simulation
Off-resonance Frequency / Δ	2000 Hz
Relative Size of Bound Proton Pool / M_{B0}	0.012
Exchange Rate / R_X	178.97 s^{-1}
Free Proton Pool Longitudinal Relaxation Rate / R_A	0.612 s^{-1}
Bound Proton Pool Longitudinal Relaxation Rate / R_B	1 s^{-1}
Pulse Amplitude / RF_{AMP}	4600
Free Proton Pool Transverse Relaxation Time / T_{2A}	0.0394 s
Bound Proton Pool Transverse Relaxation Time / T_{2B}	12.7 μs

Table 8.1 – Model Parameter Values Used in All Simulations

Figure 8.3a shows the variation in the longitudinal magnetisation of the free proton pool with time through the experiment, for a range of R_X values between 1 and 300 s^{-1}. It can be seen that an increase in the exchange rate leads to a greater attenuation of the longitudinal magnetisation of the free proton pool. It can also be seen that this is an effect that becomes much smaller as the exchange rate becomes significantly greater than the longitudinal relaxation rate of the bound proton pool. Figure 8.3a was obtained by using an R_B value of unity and as such, the effect of an increase in R_X beyond 100 s^{-1} appears to be insignificant.

Figure 8.3b shows the effect of variation in the relative size of the bound proton pool on the longitudinal magnetisation of the free proton pool as the experiment progresses. It shows that an increase in M_{B0} leads to a decrease in the asymptotic value of the longitudinal magnetisation of the free proton pool in the range investigated, $M_{B0} = 0.001$ to 0.05. As the size of the bound proton pool is increased, not only does the asymptotic value decrease but the rate at which it is reached increases.

Figure 8.3a – Variation of Free Proton Pool Magnetisation
with Time After Initial Off-Resonance Pulse for a Range of
Magnetisation Transfer Exchange Rates.
Figure 8.3b – Variation of Free Proton Pool Magnetisation
with Time After Initial Off-Resonance Pulse for a Range of
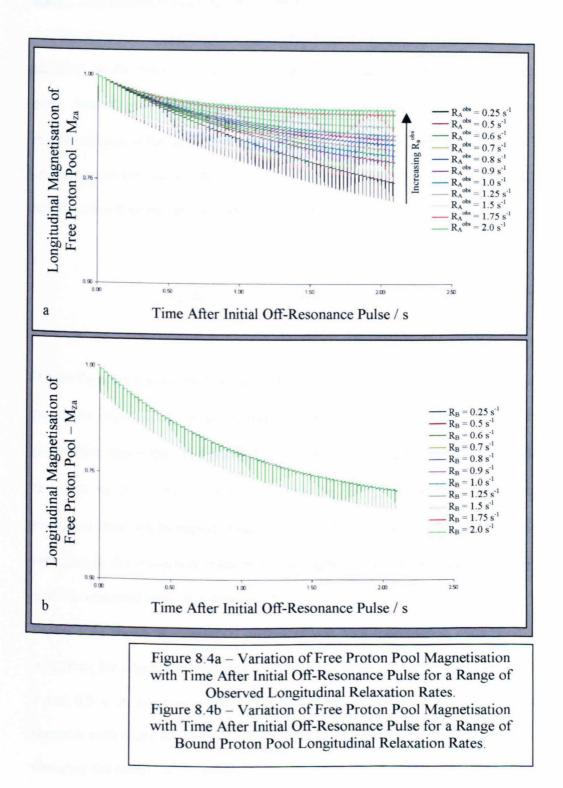Relative Bound Proton Pool Sizes.

8.2.4 The Longitudinal Relaxation Rates

A difficulty in the model arises when considering the longitudinal relaxation rates to use. The longitudinal relaxation rates are usually similar in magnitude and therefore difficult to separate. Following the work of Henkelman[2], we chose to replace the longitudinal relaxation rate of the free proton pool with the observed relaxation rate, R_A^{obs}, which describes the combined relaxation properties of the two pools. The explicit relationship between R_A, R_A^{obs}, R_B and M_{B0}, assuming that $R_X \gg (R_B - R_A^{obs})$, is given in equation 8.6 and was used in the construction of the model to replace the need for a measurement of R_A.

$$R_A = R_A^{obs} - M_{B0}\left(R_B - R_A^{obs}\right) \qquad - \qquad 8.6$$

Figure 8.4a shows the variation in the longitudinal magnetisation of the free proton pool with time, for a series of R_A^{obs} values ranging from 0.25 s^{-1} to 2.0 s^{-1}. An increase in the observed longitudinal relaxation rate causes the longitudinal magnetisation of the free proton pool to tend towards a higher value as well as approaching its asymptotic value at a faster rate. This is because there is less exchange between the two pools because of a faster rate of recovery of the free proton pool back to equilibrium between the off-resonance pulses.

Figure 8.4b shows the variation of the model for a range of bound proton pool longitudinal relaxation rates between 0.25 and 2.0 s^{-1}. No significant difference in the model can be seen over this considerable range of values, highlighting the lack of interest in further study of this parameter and confirming the findings of Henkelman that this parameter cannot be measured through a simple magnetisation transfer experiment.

Figure 8.4a – Variation of Free Proton Pool Magnetisation
with Time After Initial Off-Resonance Pulse for a Range of
Observed Longitudinal Relaxation Rates.
Figure 8.4b – Variation of Free Proton Pool Magnetisation
with Time After Initial Off-Resonance Pulse for a Range of
Bound Proton Pool Longitudinal Relaxation Rates.

8.2.5   The Transverse Relaxation Times

The presence of exchange between the free and bound proton pools can have an effect on the measurement of the transverse relaxation time of the free proton pool. According to the work of Hazlewood *et al*[11], the observed transverse relaxation time of the free proton pool can be written in the form of equation 8.7, assuming that the size and the transverse relaxation time of the free proton pool is much greater than that of the bound proton pool.

$$\frac{1}{T_{2A}{}^{obs}} = \frac{1}{T_{2A}} + \frac{P_B}{\tau_B + T_{2B}} \qquad - \qquad 8.7$$

Where P_B is the population fraction of the bound proton pool (similar to the model parameter M_{B0}) and τ_B is the average residence time of a proton in the bound proton pool (equivalent to $1/R_X M_{B0}$). In the study of agar gel phantoms, due to the fact that $\tau_B \gg T_{2B}$, $P_B \ll 1$ and τ_B is near to unity, the observed transverse relaxation time can be approximated to that of the free proton pool. Hence future reference to the transverse relaxation will equate the actual relaxation time, T_{2A}, with the observed relaxation time, $T_{2A}{}^{obs}$.

Figure 8.5a shows the variation in free proton pool longitudinal magnetisation with time, for a range of free proton pool transverse relaxation times between 0.01 s and 0.5 s. A trend is apparent for the saturation of the free proton pool to decrease with increasing relaxation time. This can be explained by the effect that changing the transverse relaxation time has on the width of the free proton pool's lineshape. An increased T_2 is equivalent to a narrower lineshape and as such the off-resonance pulses have less of an effect on the free proton pool magnetisation.

This leads to a point where any further increase in the transverse relaxation time of the free proton pool has no effect on the model because the lineshape has become so narrow that the off-resonance pulses have no effect on the free proton pool.
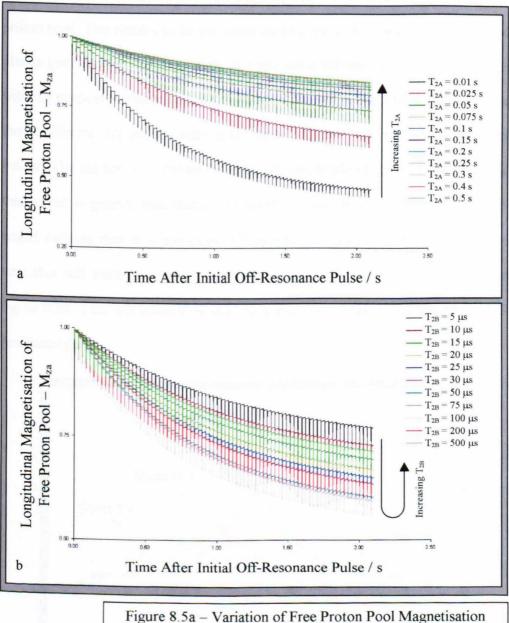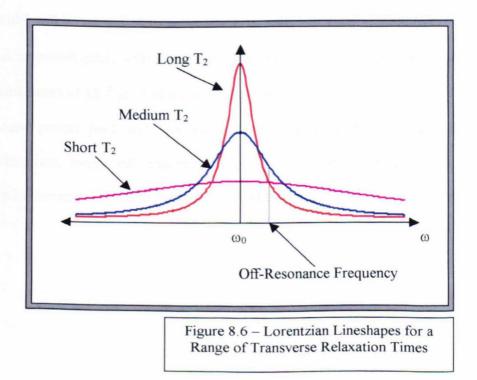

Figure 8.5a – Variation of Free Proton Pool Magnetisation with Time After Initial Off-Resonance Pulse for a Range of Free Proton Pool Transverse Relaxation Times.
Figure 8.5b – Variation of Free Proton Pool Magnetisation with Time After Initial Off-Resonance Pulse for a Range of Bound Proton Pool Transverse Relaxation Times.

Figure 8.5b shows how the model varies with the transverse relaxation time of the bound proton pool for a range of T_{2B} values between 5 μs and 500 μs. It can be seen that increasing the transverse relaxation time leads to an increase in the saturation of the bound proton pool up to a maximum level. Any further increase in the transverse relaxation time causes a decrease in the saturation of the bound proton pool. This result can be explained by examining the lineshape of the bound proton pool and how its magnitude at a particular off-resonance frequency varies with the transverse relaxation time. Figure 8.6 shows the Lorentzian lineshapes for three different transverse relaxation times. At the off-resonance frequency indicated by the arrow, it can be seen that the magnitude of the medium relaxation time curve is greater than that of the short or long relaxation time curves. This would indicate that at a particular off-resonance frequency there is a relaxation time that will yield a maximal saturation of the bound proton pool as shown in figure 8.5b. This relaxation time will be a function of the frequency of the off-resonance pulses.

Figure 8.6 – Lorentzian Lineshapes for a Range of Transverse Relaxation Times

It must be noted that through the use of a single transverse relaxation time to describe the bound proton pool, an assumption of a Lorentzian lineshape is being made. However, this is necessary to allow the use of the modified Bloch equations and the validity of this assumption will be further discussed later.

8.2.6   Parameter Measurement
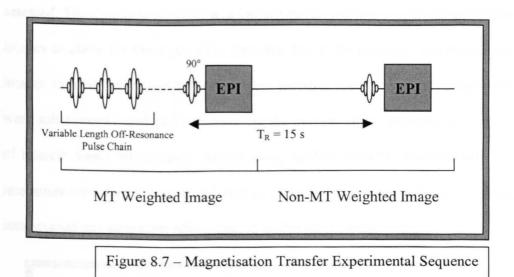
As discussed above, some parameters of the model are set by the experimental conditions or the model (Δ, ω_1 and M_{A0}), some can be determined by simple experimental means (R_A^{obs} and T_{2A}), some are insignificant (R_B) and some need to be measured or investigated further (M_{B0}, T_{2B} and R_X). In the following sections, the application of this model in the study of agar gel phantoms is discussed. According to the work of Henkelman[2], the exchange rate (R_X) for agar gel at 0.6 T is approximately 179 s^{-1}. This puts it in the region where any reasonable variation will lead to no appreciable effect on the model. The transverse relaxation time of the bound proton pool has a very complex effect on the model and so initially the model will be simplified by assuming a constant transverse relaxation time for the bound proton pool, setting this parameter in the model to the value quoted by Henkelman of 12.7 µs. The initial sections will investigate the relative size of the bound proton pool with the use of various concentrations of agar gel and subsequent work will concentrate on a more detailed investigation of the transverse relaxation time of the bound proton pool.

8.3   *Preliminary Experimentation*

8.3.1   Scanning

All scanning described in this chapter was performed on the 0.5 T purpose built EPI scanner at the University of Nottingham described in chapter 4. The MT sequence used (figure 8.7) comprised a chain of 7 ms duration, Gaussian windowed sinc pulses 2 kHz off resonance separated by 20 ms. This was followed 20 ms later by a 90° slice selective sinc pulse and a single MBEST imaging module to produce an MT weighted image. Between each application of the sequence, a non-MT weighted image acquisition was obtained by applying the sequence with no off-resonance pulses but the same gradients to allow for normalisation of the signal intensities.

Figure 8.7 – Magnetisation Transfer Experimental Sequence

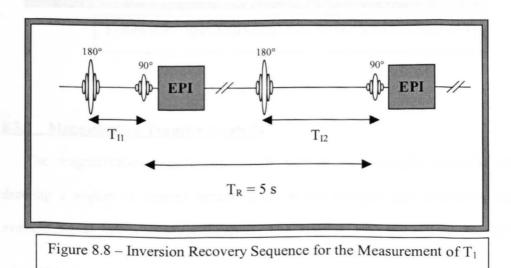The sequence was initially used in the study of four different Agar gels with concentrations of 1, 2, 3 and 4% by weight. For each gel the sequence was applied with five different pulse chains ranging in length from 15 to 75 pulses and the sequence was repeated three times for each different chain length. A repetition time, T_R, of 15 s was allowed in between each application of the sequence to

ensure full recovery of the equilibrium magnetisation and the experiment was carried out ten times to allow the accuracy and repeatability of the experiment to be assessed.
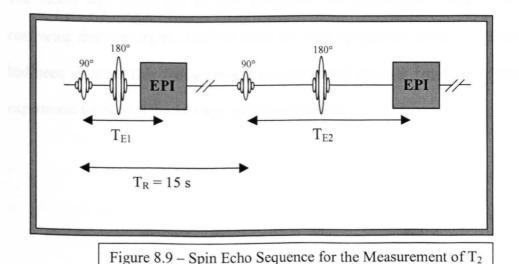
8.3.2 Relaxation Time Measurement

As required by the model, the longitudinal and transverse relaxation times of the agar gels were measured. The observed longitudinal relaxation rate, R_A^{obs} was obtained with the inversion recovery sequence shown in figure 8.8. The sequence was repeated five times for each of ten inversion times, T_I, ranging from 10 ms to 3300 ms. The sequence was applied with a repetition time, T_R, of 5 s and the experiment was carried out six times to allow the accuracy and reliability to be assessed. The time data acquired was initially processed into magnitude and phase images to allow for the sign of the modulus data to be detected. The magnitude images located before the null point were inverted using the phase images and were subsequently analysed by measuring the average signal intensity in a region of interest drawn around each sample using Analyze (MAYO Foundation). The intensities were then averaged and used to fit for T_1 in equation 2.25 whilst taking into account any saturation effects caused by the short repetition time.

Figure 8.8 – Inversion Recovery Sequence for the Measurement of T_1

The transverse relaxation time of the free proton pool, T_{2A}, was obtained using the spin echo sequence shown in figure 8.9. The sequence was repeated three times for each of twelve echo times, T_E, ranging from 80 ms to 260 ms. The sequence was applied with a repetition time, T_R, of 15 s to ensure full recovery of the equilibrium magnetisation and the experiment was carried out six times to allow the accuracy and reliability to be assessed. The magnitude images acquired were initially analysed by drawing a region of interest around each of the samples and measuring the average signal intensity using Analyze. The measured intensities were then corrected for background noise[12], as discussed in chapter 7, and after averaging over the repetitions, used to fit for T_2 in equation 2.26 with a weighted linear fit[13].

Figure 8.9 – Spin Echo Sequence for the Measurement of T_2

8.3.3 Magnetisation Transfer Analysis

The magnetisation transfer magnitude images were initially analysed by drawing a region of interest around each of the samples and measuring the average signal intensity using Analyze. The average intensities from the MT

weighted images were then normalised to their respective non-MT weighted images to provide a measure of the longitudinal magnetisation of the free proton pool at the time of image acquisition. The normalised intensities were averaged over the repetitions and entered into the ModelMaker model, with the standard deviation of the measurements being used as a measure of their accuracy. The relaxation time measurements discussed above and the experimental parameters were also entered into the model along with the values obtained by Henkelman at 0.6 T for the exchange rate, R_X, and the bound proton pool relaxation parameters, R_B and T_{2B}. Using the Marquardt[*] fitting algorithm within ModelMaker[10], the relative size of the bound proton pool, M_{B0}, was optimised by fitting the longitudinal magnetisation of the free proton pool, M_{ZA}, to the experimental data. The model was considered to have completed the optimisation when it had completed five convergent steps[#] or when the limit of accuracy of the computer had been reached. This fitting process was conducted for each repetition of the experiment for each of the four agar gel concentrations.

---

[*] The Marquardt fitting algorithm (also known as the Levenberg-Marquardt method) is a method of non-linear regression that combines a Taylor's series approach when near to the minimum with an iterative steepest descent method when further away, producing a very robust fitting algorithm.
[#] A convergent step is considered to have occurred when the algorithm improves the value of χ^2 marginally without altering the model parameters significantly.

Agar Gel Concentration	Longitudinal Relaxation Rate (R_A^{obs}) / s^{-1} Ave. ± S.D.	Transverse Relaxation Time (T_{2A}) / s Ave. ± S.D.
1%	0.48 ± 0.02	0.145 ± 0.003
2%	0.55 ± 0.02	0.077 ± 0.001
3%	0.62 ± 0.02	0.052 ± 0.002
4%	0.69 ± 0.02	0.040 ± 0.003

Table 8.2 – Relaxation Parameters of Agar Gel Phantoms

8.3.4   Results

The longitudinal and transverse relaxation parameters obtained are detailed in table 8.2. As expected, both the transverse and the longitudinal relaxation rates are linear with gel concentration. Figure 8.10a shows an example of the experimental and the fitted model data for the 4% agar gel phantom. Excellent agreement can be seen between the experimental data and the model. Figure 8.10b shows the normalised signal intensity from the 75 off-resonance pulse application of the experiment (S_{75}/S_0) as a function of agar concentration. A linear relationship between agar gel concentration and signal attenuation can be seen.

Figure 8.10a – Example of Experimental (Pink Squares) and Fitted
Model (Blue Line) Data for 4% Agar Gel Phantom.
Figure 8.10b – Variation in the Magnetisation Transfer Ratio with
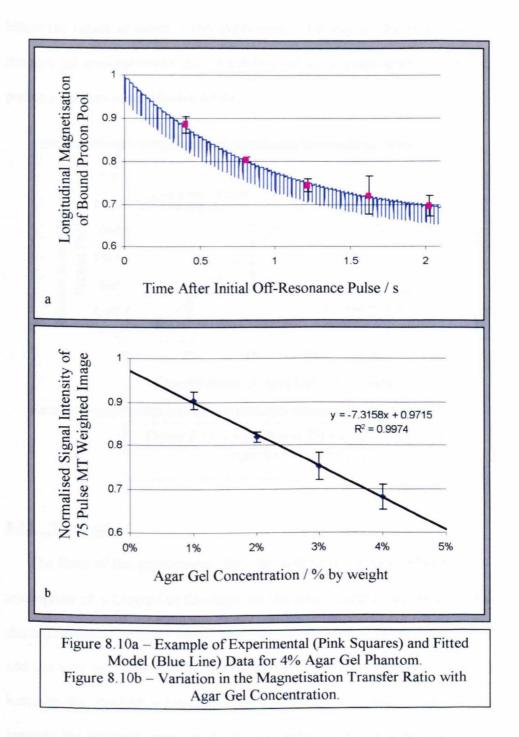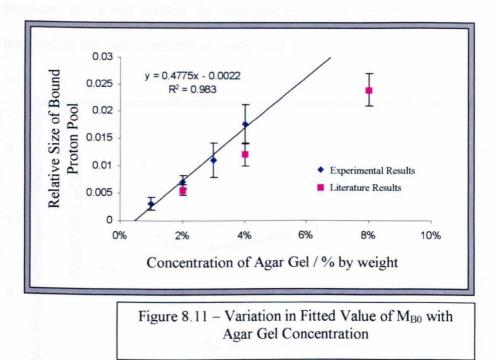Agar Gel Concentration.

Figure 8.11 shows the variation of fitted value for the bound proton pool size with

agar gel concentration. Again a linear relationship with agar gel concentration can

be seen. The values quoted by Henkelman at 0.6 T are also shown and they all lie

below the values obtained in this experiment. This may be due to a difference in the agar gel preparations or due to a difference in the assumed value of the bound proton pool transverse relaxation time.

Figure 8.11 – Variation in Fitted Value of M_{B0} with Agar Gel Concentration
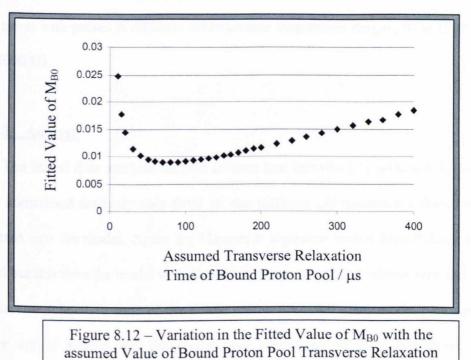
8.3.5 Discussion

The form of the experimental data fits well to the model, indicating that the assumption of a Lorentzian lineshape for the bound proton pool is acceptable in this application. The linear relationship between the size of the bound proton pool and the agar gel concentration is in agreement with the findings of Henkelman, however the absolute values differ slightly. Figure 8.12 shows the relationship between the assumed value for the bound proton pool transverse relaxation time and the fitted value of M_{B0} for the 4% agar gel data. It can be seen, as with the variation of the model in section 8.2.5, that an increase in the transverse relaxation time initially leads to a decrease in the fitted value down to a minimum. Any further increase in the value of T_{2B} causes the fitted value to increase. This finding

would suggest that a higher value of T_{2B} would yield a result more inline with the data published by Henkelman. However, the difference may also be due to differences in the agar used or in the method of agar preparation. It is therefore necessary to try and quantify the transverse relaxation time of the bound proton pool before any conclusion can be made on this.

Figure 8.12 – Variation in the Fitted Value of M_{B0} with the assumed Value of Bound Proton Pool Transverse Relaxation Time for the 4% Agar Gel Sample.

8.4   *Improving the Analysis*
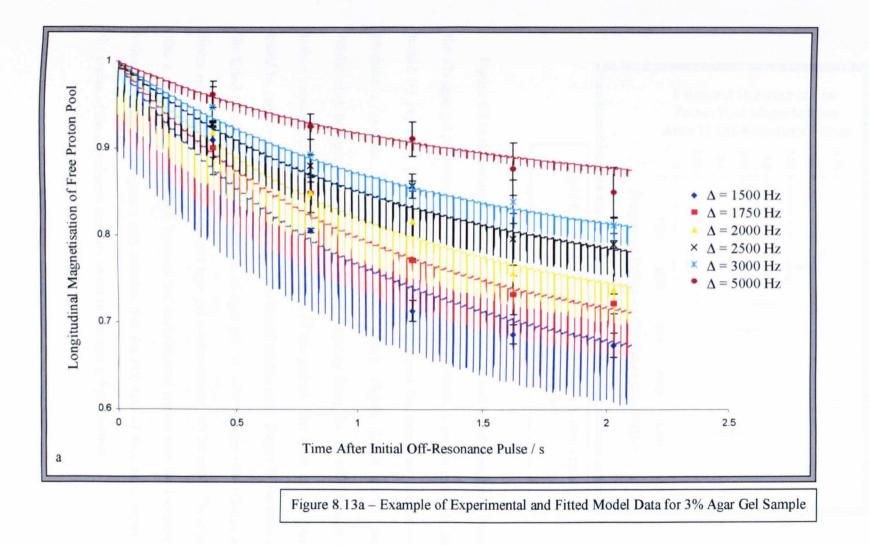
In order to improve the model and the fitting process, it is necessary to expand the technique so that it is possible to fit for the transverse relaxation time of the bound proton pool as well its relative size. Preliminary attempts to use the data already acquired to fit for both parameters proved unsuccessful due to a lack of sensitivity to the value of T_{2B}. This is due to the fact that the acquired data does not probe the bound pool lineshape in any way. In order to improve the model, it is essential to investigate how the system varies with the frequency of the off-

resonance pulses. This would probe the bound pool lineshape and provide the model with more sensitivity to the bound pool's transverse relaxation time.

8.4.1   Experimental Method

The experimental method employed follows that used previously, as described in section 8.3.1. Differing only in the fact that the whole experiment was repeated six times with pulses at different off-resonance frequencies ranging from 1500 Hz to 5000 Hz.

8.4.2   Analysis

The initial data analysis method follows that described in section 8.3.3 with the normalised intensity data from all the different off-resonance values being entered into the model. Again the Marquardt algorithm within ModelMaker was used but this time the model was allowed to optimise both the relative size and the transverse relaxation time of the bound proton pool. All other model parameters were set as before and the model was considered to have completed the optimisation after five convergent steps or when the limit of the computer's accuracy had been reached.

Figure 8.13a – Example of Experimental and Fitted Model Data for 3% Agar Gel Sample

8.4.3 Results

Figure 8.13b – Variation in the Magnetisation Transfer Ratio with Frequency Offset.
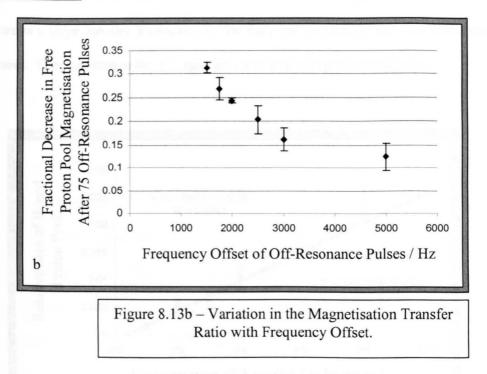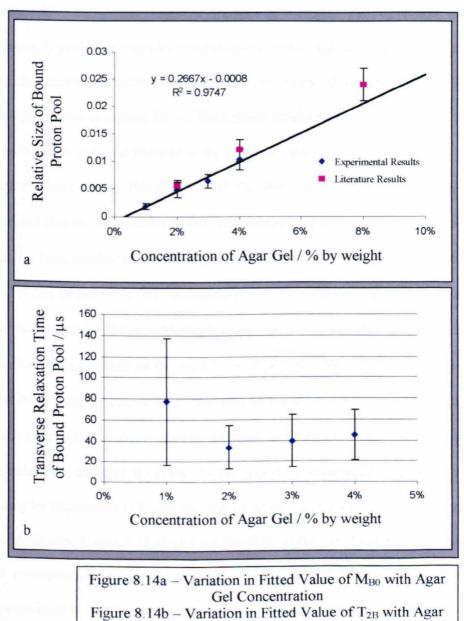
Figure 8.13a shows an example of the experimental and fitted model data from the 3% agar gel phantom for all six of the resonance offsets. It can be seen that, as would be expected, pulses applied further away from the resonance frequency produce a smaller magnetisation transfer effect. Figure 8.13b shows the relationship between the normalised signal intensity from the 75 off-resonance pulses experiment and the frequency offset of the pulses. The form of this plot could be used to probe the lineshape of the bound proton pool. Figure 8.14a shows the fitted values of M_{B0} as a function of agar gel, as with the previous results, a linear relationship between M_{B0} and agar gel concentration can be seen. There is also a much better agreement between the experimental results and the literature values[2]. A slight discrepancy still remains, but the two sets of data agree within the errors of the experiment and any errors in the agar gel production.

Figure 8.14b shows the fitted values of T_{2b} as a function of agar gel concentration. There is a large amount a variation in the data and as such no apparent trend can be seen. The variation in the 1% agar gel sample data is particularly large.

Figure 8.14a – Variation in Fitted Value of M_{B0} with Agar Gel Concentration

Figure 8.14b – Variation in Fitted Value of T_{2B} with Agar Gel Concentration

8.4.4   Discussion

As seen before, there is a linear relationship between the agar gel concentration and the fitted value of M_{B0}. This result is as expected because 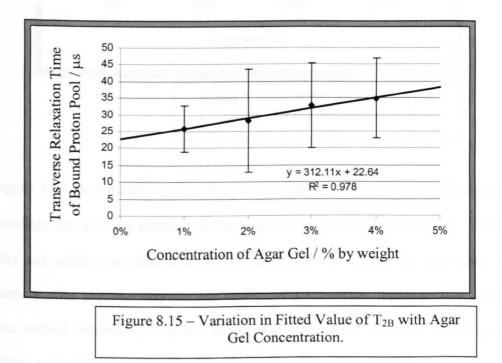an increase in the gel concentration would lead to an increase in the number of protons held within the chemical structure of the agar. The agreement with the previously published work by Henkelman is better than with the previous method and the results lie within the experimental errors of the two sets of results. However, there is a trend for the Henkelman results to lie above the fitted values, possibly indicating a difference in the agar gels used.
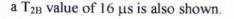
Further study of the fitted values of T_{2B} from the 1% concentration agar gel revealed that the large errors in the measurement are due to several measurements that are considerably higher than the others. When considering the form of figure 8.12 it can be seen that there is degeneracy in the measurement of T_{2B} and as such the model may be fitting to the higher value of T_{2B} that is above the minimum in the curve. This failure of the model seems to affect the lowest concentration of agar more than the others, a fact that may be explained by the lower value of M_{B0}. If the optimisation process initially attempts to fit the model on the wrong side of the minimum of figure 8.12, then by the time it has converged on a value for M_{B0}, it may be impossible to locate the true value of T_{2B} due to its distance away from the minimum. Figure 8.15 shows the variation in the fitted value of T_{2B} with agar gel concentration when all results that lie above the minimum of figure 8.12 (approximately 70 µs) have been removed. It can be seen that the errors in the results have been reduced and there appears to be a linear trend for T_{2B} to increase with agar gel concentration. This correction method is a very simplistic approach to overcoming the failure of the model to fit for the correct value of T_{2B} and more

detailed study of how the form of figure 8.12 varies with agar concentration and frequency would be necessary before the model could be constrained to prevent it from fitting to the wrong value.

It might be expected that the transverse relaxation time of the bound proton pool would decrease with increasing agar concentration due to the decreased mobility of the protons. However, an increased effect on the bound protons by the fields from neighbouring macromolecules at lower agar concentrations could explain this result. Also, the errors in the fitting are large and the trend shown may be due to a systematic failure of the model.

Figure 8.15 – Variation in Fitted Value of T_{2B} with Agar Gel Concentration.

Study of the T_{2B} values shown in figure 8.15 reveals that they are all higher than the value of 12.7 μs produced by Henkelman. Although this difference may in part be due to differences in the Agar gel or in the gel production methods used, the assumption of a Lorentzian rather than a Gaussian lineshape for the bound proton pool is also partly responsible. Figure 8.16 shows a Gaussian lineshape, as

described by Henkelman with a T_{2B} value of 12.7 µs. A Lorentzian lineshape with a T_{2B} value of 16 µs is also shown.

Figure 8.16 – Lorentzian and Gaussian Lineshapes for the Bound Proton Pool
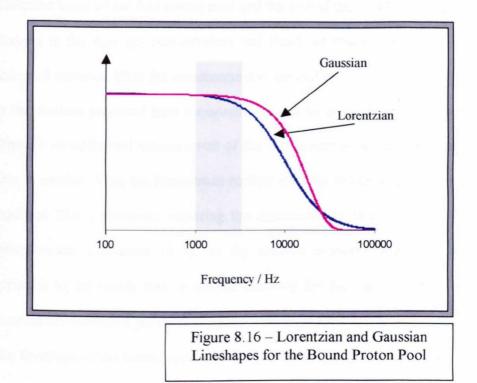
Figure 8.16 demonstrates the ability to generate a Lorentzian and a Gaussian lineshape that are very similar over the frequency range investigated (1000 – 5000 Hz) and which only diverge at the higher frequencies probed by Henkelman's method. This explains why the assumption of a Lorentzian lineshape is valid in this method. However, to obtain this similarity, a higher T_{2B} value is required, giving a possible reason for the higher T_{2B} values fitted by the model.

8.4.5 Summary

The model and method presented here builds on the work of Henkelman and there are many features that are common to both techniques. For example, the use of a fundamental rate constant to describe exchange between the two pools.

However, there are several key differences between the two methods that need to be highlighted. Firstly, the Henkelman method assumed linear changes in the relaxation times of the free proton pool and the size of the bound proton pool with changes in the agar gel concentration and fitted the model parameters globally across all samples. Thus the measurement of several samples is required, whereas in the method proposed here measurements can be made from a single sample although an additional measurement of the free proton pool transverse relaxation time is needed. Also, the Henkelman method uses the steady state solution of the modified Bloch equations, requiring the application of relatively long duration off-resonance irradiation (5 s). In the method proposed here, the transient approach to the steady state is studied allowing for the use of a chain of short duration off-resonance pulses that greatly reduce the SAR levels of the sequence.

The lineshape of the bound proton pool is another key difference between the two methods. The work of Henkelman and others has demonstrated the improved accuracy of a Gaussian lineshape in describing the bound proton pool. However, attempts to modify the Bloch equations to yield a Gaussian lineshape have proved unsuccessful and so the assumption of a Lorentzian lineshape is necessary to allow the transient approach to steady state to by studied. As demonstrated by figure 8.16, the relatively low off-resonance frequencies probed with this method ensure that the assumption of a Lorentzian lineshape is not inappropriate. However, further work is required to improve this area of the model to provide a greater accuracy over a wider frequency range.

Possibly the most important difference between the two methods discussed here is their application in the clinical setting. The Henkelman method is well suited to *in vitro* studies but its high SAR levels and long experimental duration limit its

usefulness *in vivo*. The following sections describe how the method proposed in this work can be used to study the size of the bound proton pool in a clinically feasible application.

8.5 *Application of the Technique*

As discussed in the introduction to this chapter, the aim of this work was to generate a technique to allow for quantitation of the relative size of the bound proton pool in the human placenta. Previously published data[9] has shown a trend for the transverse and longitudinal relaxation times to decrease with gestational age following the form of equations 8.8 and 8.9.

$$T_1 = -9.1t + 1538 \qquad R^2 = 0.23 \qquad p = 0.03 \qquad - \qquad 8.8$$

$$T_2 = -4.0t + 338 \qquad R^2 = 0.47 \qquad p = 4 \times 10^{-6} \quad - \qquad 8.9$$

Where t is the gestational age in weeks. The previous study also reported a significant decrease in the longitudinal and transverse relaxation times in pregnancies compromised by IUGR or Pre-Eclampsia. The aim of this work is to quantify the relative size of the bound proton pool and hence to gain a further insight into the reasons behind these trends in the relaxation times, which will allow us to understand the mechanisms leading to them.

8.5.1   Study Group Demographics

Initially a cohort of 23 volunteers was recruited to a longitudinal study during a routine examination at the Nottingham City Hospital. Written, informed consent was obtained from all volunteers and ethics approval was obtained from the local ethics committee. Volunteers were recruited on the basis of an uncomplicated pregnancy and attended the MR Centre, University of Nottingham, on four separate occasions through the pregnancy at gestational ages of 16, 22, 29 and 35 weeks. During each visit, a standard ultrasound examination and a transverse multi-slice set of images were initially obtained to allow for localisation of the placenta and selection of a slice adjacent to the position of umbilical cord insertion. MT, T_1 and T_2 measurements were then carried out as described below. During the course of the longitudinal study, 23 separate volunteers were recruited to a cross-sectional study group to investigate any effect that compromised pregnancy (IUGR and Pre-Eclampsia) might have on the magnetisation transfer measurements. The cross-sectional group were all scanned in the same manner as the longitudinal group but on only one occasion, a maximum of 48 hours before an elective caesarean section. Of the 23 women recruited, 11 had pregnancies complicated by either Pre-Eclampsia, IUGR or both conditions.

8.5.2   Magnetisation Transfer Measurements

Magnetisation transfer measurements were carried out on a transverse slice containing the placenta, adjacent to the point of cord insertion. The sequence shown in figure 8.7 and described in section 8.3.1 was applied with a frequency offset of 2 kHz and five pulse chains varying in length from 3 to 50 pulses. The experiment was repeated three times for each investigation. A region of interest

encompassing the whole placenta was drawn and the average signal intensity measured using Analyze. The signal intensities from the MT weighted images were then normalised to their respective non-MT weighted images and averaged over the repetitions.

Before application, the SAR level of the sequence was calculated by measuring the forward power to the RF coil and was shown to be less than 0.24 W/kg assuming all power to the coil was deposited in the patient. This level is considerably below the recommended restrictions on whole body SAR issued by the National Radiological Protection Board (NRPB) of 2 W/kg[14,15]. Also, the longer off-resonance pulse chain lengths were separated as much as possible to evenly distribute the SAR level throughout the acquisition.

8.5.3 Relaxation Time Measurements

The longitudinal relaxation time of the placenta was measured by applying the technique described in section 8.3.2 on the same slice as the magnetisation transfer measurements. As before five images were obtained at ten different inversion times ranging from 10 ms to 3300 ms. The transverse relaxation time of the placenta was also measured on the same slice by applying the technique described in section 8.3.2. However, only two repeats were taken at each of eight different echo times ranging from 80 ms to 260 ms. The number of repetitions and echo times used was reduced to shorten the scanning time and maintain the whole examination time below half an hour. The analysis of both relaxation times was carried out as before with the measurement being carried out on a region of interest that was drawn to encompass the whole placenta.

8.5.4   Preliminary Results

Figures 8.17-8.19 show the variation with gestational age of the longitudinal relaxation time, the transverse relaxation time and the normalised signal intensity from the 50 off-resonance pulse images for all of the volunteers scanned. As with the previous data, a trend for the relaxation times to decrease with gestational age can be seen. The equation describing the trend in the transverse relaxation time is approximately the same as previously shown and the equation describing the trend in the longitudinal relaxation time is similar but slightly less steep than before. A major difference between this study and that previously published is that neither of the relaxation times measured appear to be reduced in compromised pregnancy. Figure 8.19 shows a weak trend for the magnetisation transfer ratio to decrease with gestational age. No apparent link between the magnetisation transfer ratio and the condition of the pregnancy can be seen.
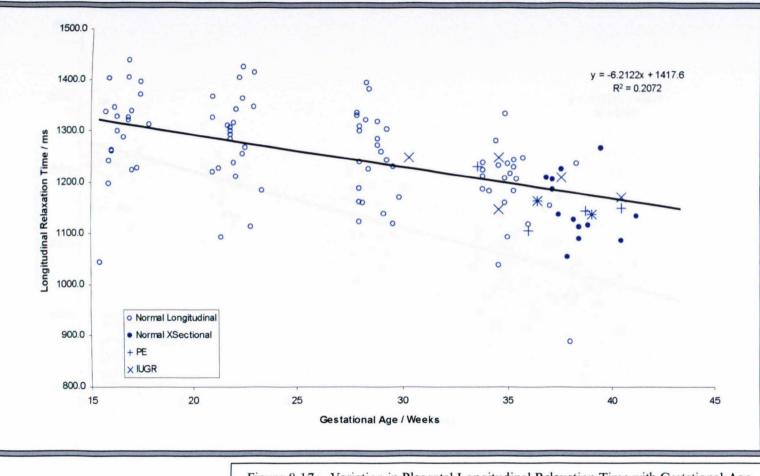
Figure 8.17 – Variation in Placental Longitudinal Relaxation Time with Gestational Age
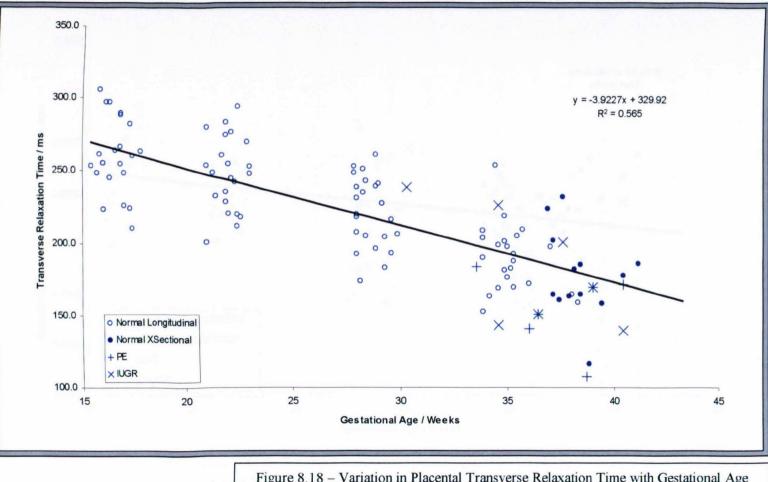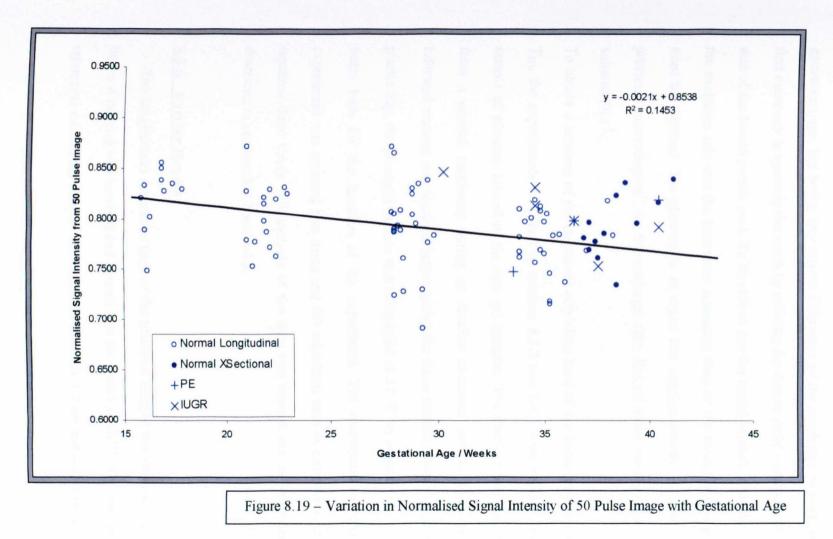
Figure 8.18 – Variation in Placental Transverse Relaxation Time with Gestational Age

Figure 8.19 – Variation in Normalised Signal Intensity of 50 Pulse Image with Gestational Age

The plot shows data points with the following legend:
- o Normal Longitudinal
- • Normal XSectional
- + PE
- × IUGR

The regression line equation is:

$$y = -0.0021x + 0.8538$$
$$R^2 = 0.1453$$

8.5.5 Obtaining a Value for the Model Parameters, T_{2B} & R_X

The magnetisation transfer ratio may show a weak trend to decrease with gestational age, but before any serious discussion of the result can be made it is first necessary to quantify the result by utilizing the data to yield a measure of the size of the bound proton pool. To be able to use the model created, a measure of the exchange rate and the transverse relaxation time of the bound proton pool must be obtained. The placenta is an organ that consists mainly of blood and previous measurements[16] on the exchange rate, R_X, of blood have produced a value of 38 s^{-1}.

To obtain a measure of the transverse relaxation time of the bound proton pool, T_{2B}, the experiments described in sections 8.3.2 and 8.4.1 were repeated on a sample of placenta instead of the agar gel samples. The placenta was obtained from a normal pregnancy during an elective caesarean section and written informed consent was obtained before taking the tissue sample. Once sealed in a plastic bag, the placental sample was maintained at 37 °C by submersing it in a water bath for the duration of the experiment. The magnetisation transfer experiment was repeated five times and the relaxation time measurements were repeated three times. All analysis of the data was carried out in the manner described in sections 8.3.2 and 8.4.2.

8.5.6 Further Results

The longitudinal relaxation time of the placental sample was measured to be 989 ± 4 ms and was inverted and entered into the model as $R_A{}^{obs}$. The transverse relaxation time of the sample was measured to be 130 ± 2 ms and was entered into

the model as T_{2A}. The model was then applied using these values and produced measurements of $M_{Bo} = 0.044 \pm 0.005$ and $T_{2B} = 45 \pm 10$ μs.

This value of T_{2B} was then used to analyse the magnetisation transfer data obtained from the *in vivo* studies, along with an exchange rate, R_X, of 38 s^{-1} and relaxation times given by the individual experiments carried out on each subject. Figure 8.20 shows the variation in the fitted value of M_{B0} with gestational age for all of the subjects scanned. The data shows a very weak trend for the value of M_{B0} to increase with gestational age but shows no apparent trend for any change with condition of pregnancy.
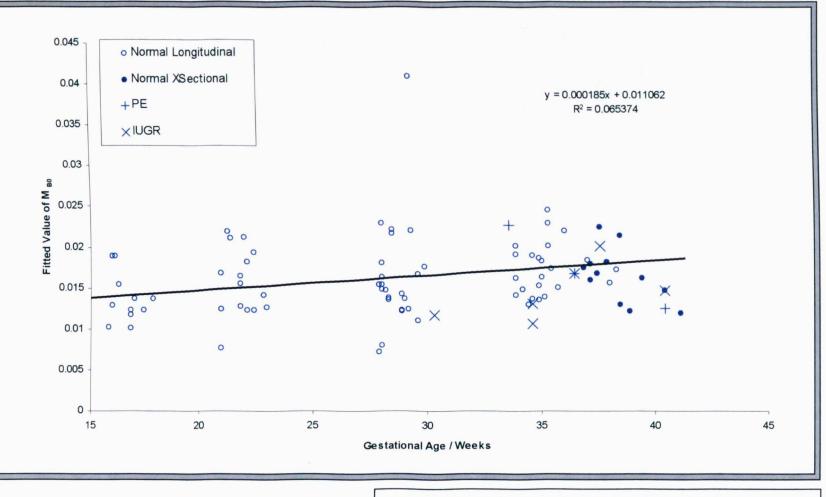
Figure 8.20 – Variation in Fitted Value of M_{B0} with Gestational Age

8.5.7   Discussion

Inspection of the *in vivo* and *ex vivo* values of the bound proton pool size in the placenta show that the fitted value obtained from the *ex vivo* sample is considerably higher than average value of the *in vivo* results. This can be explained by the fact that the placental sample will have contained significantly less blood than a placenta *in vivo*. Blood inside the placental sample will also have begun to clot whilst the experiment was being conducted. Both of these factors would serve to reduce the size of the free proton pool and increase the relative size of the bound proton pool. The fitted value of 45 µs for the transverse relaxation time of the bound proton pool obtained from the *ex vivo* experiment is similar to the value of 58 µs reported by Caines *et al* for rat muscle[17].

The *in vivo* results shown in figure 8.20 indicate a very weak trend for the fitted value of the relative size of the bound proton pool to increase with gestational age. It has been shown previously that, in the human placenta, there is a reduction in the volume of the intervillous space per unit surface area of the villi during pregnancy[9]. This would explain the increase in the value of M_{B0} with gestational age as shown. This relationship could also explain the variation in the relaxation times with gestational age. However, the trend for T_2 to decrease with gestational age is much stronger than the similar trend with T_1. This could be because any variation in the size of the bound proton pool affects the transverse relaxation time more than the longitudinal relaxation time or because there is another factor that is affecting the transverse relaxation time. A reduction in the transverse relaxation time could be explained by a reduction in the oxygenation level of the blood within the placenta, but at 0.5 T this is unlikely to be the only other factor. It is

more likely that there is a complex combination of factors that lead to the gestational age variations shown.

The previous study into the measurement of placental relaxation times showed a significant reduction in the value of T_1 and T_2 in pregnancies compromised by IUGR or Pre-Eclampsia[9]. This result was not shown in this study and there was also no change in the fitted value of M_{B0} for compromised pregnancies. It can be observed that within the compromised pregnancy group, the majority of T_2 values lie below and the majority of M_{B0} values lie above the average values. However, this is simply an observation and is not statistically significant. The difference between this study and the previously published data may be found in studying the severity of the patient's disease. There is reason to believe that patients with more severe IUGR were included in the previous study due to a different recruitment strategy.

8.6   Conclusion

The work presented here has shown that it is possible to produce a quantitative measurement of the size of the bound proton pool in a clinically feasible imaging time. It has also been shown that, by extending the duration of the experiment, it is also possible to measure the transverse relaxation time of the bound proton pool. The ability to produce a quantitative measure of magnetisation transfer yields more information than that provided by simple magnetisation transfer ratio (MTR) images. It is possible for MTR images to be misleading because changes in MTR images can be purely due to changes in the relaxation properties of the sample and not any true difference in the magnetisation transfer parameters[18].

The values of M_{B0} presented for agar gel agree well with the previously published work of Henkelman[2]. The T_{2B} values produced for the agar gel phantoms are a little higher than the published value, an effect that can be explained by the assumption of a Lorentzian rather than a Gaussian lineshape for the bound proton pool. Further study of the form of the bound proton pool lineshape is required to allow the model to be improved. It is also necessary to improve the fitting procedure to prevent the degeneracy in the value of T_{2B} allowing the model to fit for the wrong value.

The *in vivo* application of the sequence has shown that it is possible to apply the method to clinical applications and highlights the true potential of the method to produce quantitative magnetisation transfer measurements *in vivo* in the clinical setting. The SAR measurements also show that the combination of pulsed off-resonance irradiation of the bound proton pool and EPI image acquisition alleviates any safety concerns there may be with quantitative MT techniques.

The *in vivo* data shows only a weak trend for any gestational age variation in the fitted value of M_{B0} and no effect on the measurement caused by compromise in pregnancy. The results are based on an assumed value of R_X and as such the technique could be improved by attempting to include a fit for the value of R_X. However, this is a difficult improvement to make due to the relatively weak effect that R_X has on the model in comparison to M_{B0}.

References

[1] Henkelman, R.M., et al., *Magnetization Transfer in MRI: a review.* NMR in Biomedicine, 2001. **14**: p. 57-64.

[2] Henkelman, R.M., et al., *Quantitative Interpretation of Magnetization-Transfer.* Magnetic Resonance in Medicine, 1993. **29**(6): p. 759-766.

[3] Sled, J.G. & Pike, G.B., *Quantitative Interpretation of Magnetization Transfer in Spoiled Gradient Echo MRI Sequences.* Journal of Magnetic Resonance, 2000. **145**: p. 24-36.

[4] Sled, J.G. & Pike, G.B., *Quantitative Imaging of Magnetization Transfer Exchange and Relaxation Properties In Vivo Using MRI.* Magnetic Resonance in Medicine, 2001. **46**: p. 923-931.

[5] Lee, R.R. & Dagher, A.P., *Low Power Method for Estimating the Magnetization Transfer Bound Pool Macromolecular Fraction.* Journal of Magnetic Resonance Imaging, 1997. **7**: p. 913-917.

[6] Chai, J.W., et al., *Estimation of In Vivo Proton Intrinsic and Cross-Relaxation Rate in Human Brain.* Magnetic Resonance in Medicine, 1996. **36**: p. 147-152.

[7] Gochberg, D.F., et al., *Quantitative imaging of magnetization transfer using multiple selective pulses.* Magnetic Resonance in Medicine, 1999. **41**(5): p. 1065-1072.

[8] Ranjeva, J.P., et al., *Magnetization transfer with echo planar imaging.* Magnetic Resonance Materials in Physics Biology and Medicine, 1997. **5**(4): p. 259-265.

[9] Gowland, P.A., et al., *In vivo relaxation time measurements in the human placenta using echo planar imaging at 0.5 T.* Magnetic Resonance Imaging, 1998. **16**(3): p. 241-247.

[10] Walker, A. and N. Crout, *ModelMaker : User Manual.* 1997: Cherwell Scientific Publishing.

[11] Hazlewood, C.F., et al., *Nuclear Magnetic Resonance Transverse Relaxation Times of Water Protons in Skeletal Muscle.* Biophysical Journal, 1974. **14**: p. 583-605.

[12] Henkelman, R.M., *Measurement of Signal Intensities in the Presence of Noise in Mr Images.* Medical Physics, 1985. **12**(2): p. 232-233.

[13] Press, W.H., et al., *Numerical Recipes in C.* 2nd ed. 1993: Cambridge University Press.

[14] NRPB, *Documents of the NRPB - Board Statement on Clinical Magnetic Resonance Diagnostic Procedures.* 1991, National Radiological Protection Board: Didcot, Oxon.

[15] NRPB, *Documents of the NRPB - Board Statement on Restrictions on Human Exposure to Static and Time Varying Electromagnetic Fields and Radiation.* 1993, National Radiological Protection Board: Didcot, Oxon.

[16] Graham, S.J. and R.M. Henkelman, *Pulsed magnetization transfer imaging: Evaluation of technique.* Radiology, 1999. **212**(3): p. 903-910.

[17] Caines, G.H., et al., *Incorporation of Magnetisation Transfer into the Formalism for Rotating-Frame Spin-Lattice NMR Relaxation in the Presence of an Off-Resonance Irradiation Field.* Journal of Magnetic Resonance, 1991. **95**: p. 558-566.

[18] Stanisz, G.J., et al., *Why Does MTR Change with Neuronal Depolarization?.* Proc. Intl. Soc. Mag. Reson. Med., 2001. **9**: p.1192.

[19] Balaban, R.S. and T.L. Ceckler, *Magnetization Transfer Contrast in Magnetic Resonance Imaging.* Magnetic Resonance Quarterly, 1992. **8**(2): p. 116-137.

[20] Berry, I., et al., *A multicenter measurement of magnetization transfer ratio in normal white matter.* Jmri-Journal of Magnetic Resonance Imaging, 1999. **9**(3): p. 441-446.

[21] Edzes, H.T. and E.T. Samulski, *Cross Relaxation and Spin Diffusion in the Proton NMR of Hydrated Collagen.* Nature, 1977. **265**: p. 521-523.

[22] Edzes, H.T. and E.T. Samulski, *The Measurement of Cross-Relaxation Effects in the Proton NMR Spin-Lattice Relaxation of Water in Biological Systems: Hydrated Collagen and Muscle.* Journal of Magnetic Resonance, 1978. **31**: p. 207-229.

[23] Eng, J., T.L. Ceckler, and R.S. Balaban, *Quantitative H-1 Magnetization Transfer Imaging Invivo.* Magnetic Resonance in Medicine, 1991. **17**(2): p. 304-314.

[24] Forsen, S. and R.A. Hoffman, *Study of Moderately Rapid Chemical Exchange Reactions by Means of Nuclear Magnetic Double Resonance.* The Journal of Chemical Physics, 1963. **39**(11): p. 2892-2901.

[25] Gounot, D., Y. Mauss, and J. Chambron, *TO5 as a magnetization transfer contrast test object: Characterization of the gels and determination of the real magnetization transfer.* Magnetic Resonance Materials in Physics Biology and Medicine, 1996. **4**(3-4): p. 195-204.

[26] Grenier, D., S. Deval, and A. Briguet, *A New Approach for On-Resonance Magnetization Transfer Parameter Optimization.* Magnetic Resonance Materials in Physics Biology and Medicine, 1998. **7**: p. 131-140.

[27] Hajnal, J.V., et al., *Design and Implementation of Magnetization Transfer Pulse Sequences for Clinical Use.* Journal of Computer Assisted Tomography, 1992. **16**(1): p. 7-18.

[28] Hu, B.S., et al., *Pulsed Saturation Transfer Contrast.* Magnetic Resonance in Medicine, 1992. **26**(2): p. 231-240.

[29] Jones, R.A. and T.E. Southon, *A Magnetization Transfer Preparation Scheme for Snapshot Flash Imaging.* Magnetic Resonance in Medicine, 1991. **19**(2): p. 483-488.

[30] Jones, R.A. and T.E. Southon, *Improving the Contrast in Rapid Imaging Sequences with Pulsed Magnetization Transfer Contrast.* Journal of Magnetic Resonance, 1992. **97**(1): p. 171-176.

[31] McConnell, H.M., *Reaction Rates by Nuclear Magnetic Resonance.* The Journal of Chemical Physics, 1958. **28**(3): p. 430-431.

[32] Pike, G.B., et al., *Magnetization Transfer Time-of-Flight Magnetic-Resonance Angiography.* Magnetic Resonance in Medicine, 1992. **25**(2): p. 372-379.

[33] Ropele, S., et al., *Estimation of Magnetisation Transfer Rates From PACE Experiments with Pulsed RF Saturation.* Journal of Magnetic Resonance Imaging, 2000. **12**: p. 749-756.

[34] Rourke, D.E., et al., *Stereographic Projection Method of Exactly Calculating Selective Pulses.* Journal of Magnetic Resonance Series A, 1994. **107**(2): p. 203-214.

[35] Santyr, G.E., *Magnetization Transfer Effects in Multislice Mr-Imaging.* Magnetic Resonance Imaging, 1993. **11**(4): p. 521-532.

[36] Schneider, E., R.W. Prost, and G.H. Glover, *Pulsed Magnetization Transfer Versus Continuous Wave Irradiation for Tissue Contrast Enhancement.* Jmri-Journal of Magnetic Resonance Imaging, 1993. **3**(2): p. 417-423.

[37] Stanisz, G.J., et al., *Characterizing white matter with magnetization transfer and T-2.* Magnetic Resonance in Medicine, 1999. **42**(6): p. 1128-1136.

[38] Wang, Y., T.M. Grist, and C.A. Mistretta, *Dispersion in magnetization transfer contrast at a given specific absorption rate due to variations of RF pulse parameters in the magnetization transfer preparation.* Magnetic Resonance in Medicine, 1997. **37**(6): p. 957-962.

[39] Wilcox, M.A., et al., *The Individualized Birth-Weight Ratio - a More Logical Outcome Measure of Pregnancy Than Birth-Weight Alone.* British Journal of Obstetrics and Gynaecology, 1993. **100**(4): p. 342-347.

[40] Wolff, S.D. and R.S. Balaban, *Magnetization Transfer Contrast (Mtc) and Tissue Water Proton Relaxation Invivo.* Magnetic Resonance in Medicine, 1989. **10**(1): p. 135-144.

[41] Wolff, S.D. and R.S. Balaban, *Magnetization-Transfer Imaging - Practical Aspects and Clinical-Applications.* Radiology, 1994. **192**(3): p. 593-599.

[42] Wolff, S.D., J. Eng, and R.S. Balaban, *Magnetization Transfer Contrast - Method for Improving Contrast in Gradient-Recalled-Echo Images.* Radiology, 1991. **179**(1): p. 133-137.

[43] Yeung, H.N. and A.M. Aisen, *Magnetization Transfer Contrast with Periodic Pulsed Saturation.* Radiology, 1992. **183**(1): p. 209-214.

9   Work Towards a Measure of Placental Oxygenation

9.1   Introduction

The placenta is extremely well adapted to enable the transfer of oxygen and nutrients from the mother to the fetus and the removal of any waste products that the developing fetus produces. In complications of pregnancy, such as Pre-Eclampsia and IUGR, it is thought that the placenta does not implant itself into the uterine wall correctly. This leads to a less efficient transfer between mother and fetus and causes the fetus to be starved of oxygen. The lack of oxygen restricts the normal growth of the developing fetus and as such the delivered baby is abnormally small. Using magnetic resonance imaging techniques, it is possible to study the growth of the fetus[1,2] and from this any abnormalities can be detected. But it would be more useful to be able to detect any problems at their origin, namely oxygen transfer through the placenta.

Direct measurement of molecular oxygen levels is not possible due to the fact that the most common isotope of oxygen has zero spin and therefore no NMR signal. However, differences in the magnetic properties of oxyhaemoglobin and deoxyhaemoglobin inside red blood cells have been shown to lead to differences in the contrast observed in T_2 and T_2^* weighted images at different oxygenation levels[3,4]. It has also been shown that variations in the oxygenation level of blood can cause changes in the signal intensity of diffusion-weighted images because of the interaction between the diffusion sensitising gradients and the magnetic field gradients induced by the presence of deoxygenated red blood cells[5].

The variation in the signal contrast in T_2 and T_2^* weighted images with blood oxygenation was termed the Blood Oxygenation Level Dependant (BOLD) effect by Ogawa *et al*[6] and provides a means to study variations in oxygenation levels *in*

vivo. A large amount of work has been carried out by many different groups to study the origins of the BOLD effect and many applications of its use have been demonstrated, particularly in the field of Functional Magnetic Resonance Imaging (fMRI)[7,8,9,10].

The work presented in this chapter details an attempt to utilise blood oxygenation dependant forms of contrast to provide a measure of oxygenation levels within the human placenta. The overall aim of the work is to produce a technique that is able to detect the presence of a change in the oxygenation status of placentas from compromised pregnancies.

9.2 Cardiac Gated T_2^* Weighted Imaging

9.2.1 BOLD Theory

The origin of the BOLD effect lies in the magnetic properties of oxyhaemoglobin and deoxyhaemoglobin. Oxyhaemoglobin molecules are essentially diamagnetic because they are in a low electron spin state, $S=0$, but when the molecule becomes deoxygenated, there are unpaired electrons around the Fe^{2+} centre and so the electron spin state becomes high, $S=2$. This makes the deoxyhaemoglobin molecule essentially paramagnetic and leads to magnetic susceptibility differences between red blood cells and their surroundings that cause localised magnetic field gradients. These field gradients can lead to enhancement of the transverse relaxation rate, $1/T_2^*$, and in the presence of diffusion or other motions, the transverse relaxation rate, $1/T_2$. This is because water molecules in blood and the surrounding tissues experience a range of different resonance frequencies that cause a phase dispersion of the water proton signal in gradient echoes and spin echoes. Hence the presence of

deoxyhaemoglobin can reduce the signal intensity of a gradient or spin echo image, leading to image contrast that changes with the amount of deoxyhaemoglobin present. The change in signal intensity depends critically on the geometric distribution of deoxyhaemoglobin. For instance, when blood is restricted within vessels, as in most tissues, it depends on the size, distribution and orientation of the vessels.

Many groups have sought to understand the effect that changes in blood oxygenation levels will have on signal intensities *in vivo*, particularly in the study of the brain[11,12,13]. BOLD contrast is utilised in fMRI to detect neuronal activation due to the accompanying changes in cerebral blood flow (CBF), cerebral blood volume (CBV) and oxygen extraction fraction (OEF). It has been demonstrated that upon neuronal activation there is an increase in the local signal intensity in gradient echo images. It is thought that this is due to an increase in CBF in the capillaries that increases the levels of oxyhaemoglobin within them, therefore reducing the levels of deoxyhaemoglobin, and giving higher signal intensity from a gradient echo due to reduced phase dispersion.

Different groups have attempted to model the variation of signal intensity in gradient echo and spin echo images of the brain under different physiological conditions and with different sequence specific parameters. Most work has been based on Monte Carlo simulations of the random walk of a spin in and around a capillary network. The blood filled capillary has generally been modelled as a cylinder that contains material with a different magnetic susceptibility to its surroundings. This susceptibility difference causes a magnetic field around the cylinder that depends on the cylinder diameter and orientation with respect to the static magnetic field[12]. Since Ogawa *et al*[14] first presented a model for the BOLD

effect in gradient echo images, others including Kennan et al[11], Boxerman et al[13] and Weisskoff et al[12], have extended the model to account for effects due to different sized vessels, intra and extra-vascular relaxation components and a wide range of different susceptibility differences (such as those generated by paramagnetic contrast agents). All this work has led to a reasonable understanding of the BOLD effect in the capillary network of the brain. More recently, Bauer et al[15] have applied this theory in the study of the capillary region of the myocardium, but the theory remains very similar as the model is still based on the study of phase dispersion given to spins due to the magnetic fields generated around a cylinder containing deoxygenated blood.

The models that have been generated have revealed that there are three regimes of interest in the study of the BOLD effect[11]. These regimes are related to the range of different magnetic fields that a spin experiences during the production of a gradient or a spin echo. The range of different magnetic fields experienced depends on the length scale of the magnetic field gradients generated and the distance that the spin diffuses in the echo time. In the static regime, where the spins are assumed to be stationary during the time of echo formation, each spin will experience a different magnetic field dependant on its position with respect to the red blood cells or blood containing vessels. This causes a large increase in the attenuation of gradient echo images but has no effect on spin echo images because the phase shifts introduced by the field variations are refocused by the spin echo production.

In the rapidly diffusing regime, when the spins experience the full range of different magnetic fields in the time of echo formation, both the gradient echo and the spin echo show relatively little attenuation from the BOLD effect. This is due

to averaging of the magnetic fields experienced by the different spins, which limits phase dispersion and hence minimises signal attenuation. In the intermediate regime, there is motion of the spins relative to the field variations and this means that each spin will experience different fields and will undergo different phase accumulations. This leads to an intermediate attenuation in the gradient echo image and also leads to attenuation in the spin echo image. The spin echo attenuation is caused because the magnetic fields experienced before and after the 180° pulse are not the same and this means that the refocusing in the spin echo is not perfect.

9.2.2   The BOLD Effect in the Human Placenta

The work carried out previously on the theory of the BOLD effect has focussed mainly on the brain and it is very difficult to directly transfer this theory to an organ as complicated as the placenta. The structure of the placenta[16], as discussed in chapter 5, consists of pools of maternal blood that bathe the fetal villi allowing an efficient transfer of oxygen and nutrients. This is obviously very different to the capillary structure of the brain but there is still potential for the BOLD effect to alter the transverse relaxation rates observed. It could be expected that there would be relaxation enhancement within the pools of maternal blood that fill the intervillous spaces. There should also be relaxation enhancement in the vessels within the fetal villi and in the regions surrounding the villi, as with the areas surrounding the capillaries in the brain.

In fMRI, simply producing T_2^* weighted images during neuronal activity will not reveal any information about regions of activation. It is necessary to produce images during activity and during a control situation where the activated region of

the brain is in a rest state. This is not only because of the low level of the signal changes that are expected but also because T_2^* depends on the experimental set-up, e.g. shimming. Activation is then observed by looking for differences between the two sets of images. In the same way a simple T_2^* weighted image of the placenta will yield no useful information about the oxygenation levels of the maternal and fetal circulations or any oxygenation gradients between them. To produce a useful measurement, it is necessary to produce T_2^* weighted images before and after a change in the oxygenation levels and study how the signal intensity in the images has changed. Many methods for inducing a change in the oxygenation level of the placenta were considered; including giving the mother 100% oxygen to breathe[17], scanning a smoking patient before and after smoking, stimulating the fetus (as in a functional MRI protocol) using an auditory stimulus[18] and retrospectively examining images acquired at the same time as a Cardiotocograph (CTG) trace to identify periods of increased fetal activity[19]. However, it was decided that the most natural way to study a change in the oxygenation level of the placenta was to monitor the placenta through the course of the maternal cardiac cycle[20].

It has been shown that there is an oxygenation level difference of approximately 15% between the blood flowing in the maternal arteries and veins that supply the placenta. Along with this there is also a difference of approximately 35% in the oxygenation level between the blood flowing in the fetal arteries and veins that travel to the placenta[20]. These differences in the oxygenation levels would indicate that, if the blood flow in the placenta is pulsatile, there should be variations in the oxygenation level of the placenta through the maternal cardiac cycle as fresh oxygenated blood is delivered and deoxygenated blood is taken away. There

should also be oxygenation gradients across the placenta that will change as oxygen is transferred from the mother to the fetus. The changing oxygenation gradients will lead to time varying magnetic field gradients around the fetal villi and within the intervillous spaces, due to the different magnetic susceptibilities of the oxygenated and deoxygenated maternal and fetal blood. Both the varying oxygenation levels and oxygenation gradients will cause different amounts of transverse relaxation through the maternal cardiac cycle. These variations will be a complex function of the rates of delivery and removal of blood by the mother and fetus, the pattern of blood flow through the placenta and the structure of the villous trees.

Any variation in the signal intensity of T_2^* weighted images would indicate a change in blood oxygenation through the cardiac cycle. However, converting this into an indicator of the size of oxygenation gradients would require knowledge of the geometric distribution of oxygenated and deoxygenated blood, which could be obtained from a mathematical model of blood flow in the placenta. It is expected that the reduced invasion of the spiral arteries in abnormal pregnancies will lead to increased resistance to blood flow and reduced pulsatility. This would probably cause a reduction in the mixing within the placenta and would therefore lead to a reduced variation through the cardiac cycle.

9.2.3 Experimental Method

The acquisition of EPI images leads to a natural T_2^* weighting and as such it is a relatively simple task to monitor the signal attenuation arising from T_2^* effects during the maternal cardiac cycle. It is necessary to acquire a series of EPI images at different points through the cycle and examine them for any signal variation.

Several repetitions will need to be acquired at each point through the maternal cycle to minimise noise variations.

Six volunteers were recruited at a routine examination on the basis of a normal healthy pregnancy and scanned on one occasion each. Written, informed consent was given by all volunteers and ethics approval was obtained from the local ethics committee at the City Hospital, Nottingham. The gestational ages of the volunteers ranged from 16 to 40 weeks, with an average gestational age of 24 weeks (S.D. = 11). All scanning was performed on the 0.5 T purpose built whole body EPI scanner at the University of Nottingham as described in chapter 4. Data was acquired using the MBEST echo-planar encoding sequence with a switched gradient sinusoidally modulated at 0.5 kHz. Modulus images were recreated from a 128×128 matrix of complex data points giving an in plane resolution of 3.5 mm × 2.5 mm (switched × broadening gradient) and a slice thickness of 7.0 mm.

On arrival for their scan, all volunteers were initially given a standard ultrasound examination followed by the acquisition of a transverse multi-slice set of images to allow for localisation of the placenta and selection of a slice adjacent to the position of umbilical cord insertion. ECG leads were placed on the volunteer's wrists and forehead to allow for the measurement of a maternal heart trace and subsequent use of the trace to trigger the image acquisition from the R-wave of the maternal cardiac cycle. A standard 90° - EPI image acquisition, as shown in figure 9.1 was used to generate a series of T_2^* weighted images at different points in the maternal cardiac cycle. The images were acquired with an echo time, T_E, of 100 ms and a repetition time, T_R, of 15 s. Images were acquired at six different post trigger delay values evenly spaced through the maternal cardiac cycle and as many repetitions as could be achieved in a total scan time of 30 minutes were acquired.

The acquired data was post processed into modulus images and the average signal intensity from a region of interest that completely encompassed the placenta was measured using Analyze (MAYO Foundation). The average signal intensities were then plotted as a function of time through the maternal cardiac cycle. The data was further analysed to determine if there was any significant variation in the signal intensity through the maternal cardiac cycle using the single factor ANOVA statistics package within Microsoft® Excel 2000 (Microsoft Corporation, USA).
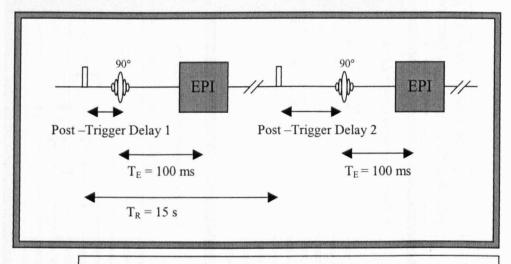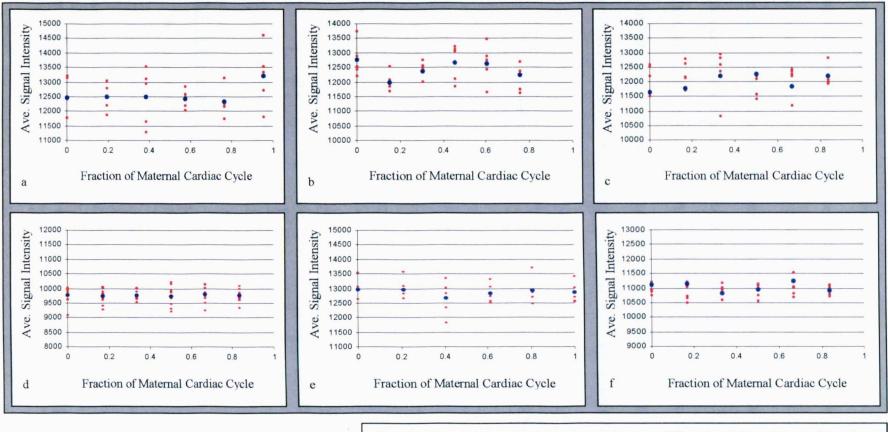
Figure 9.1 – Cardiac Gated T_2* Weighted Image Acquisition

Figures 9.2 a-f – Raw (Red Dots) and Average (Blue Dots) Signal Intensities From Maternal Cardiac Gated T_2^* Weighted Images of the Human Placenta

9.2.4   Results

Figure 9.2 shows the raw data acquired on the six volunteers. The average signal intensity at each point through the maternal cardiac cycle is represented by a blue dot. As well as showing the average intensities, all data points are shown as red dots to provide an indication of the spread in the data. No common trend for the signal intensity to vary through the maternal cardiac cycle can be seen for all volunteers but there does appear to be a sinusoidal pattern in the data from volunteer b. Table 9.1 details the single factor ANOVA statistics for all the volunteers. This demonstrates that none of the volunteers showed a statistically significant variation in the intensity through the maternal cardiac cycle.

Volunteer Number	P Value – From ANOVA
a	0.47
b	0.18
c	0.87
d	0.98
e	0.88
f	0.56

Table 9.1 – Single Factor ANOVA Statistics from Cardiac Gated T_2^* Weighted Images

9.2.5   Discussion

No consistent pattern emerged in the data for the signal intensity of T_2^* weighted images to vary with time through the maternal cardiac cycle. As mentioned, one of the volunteers appeared to show a periodic variation through the maternal cardiac cycle but the statistics showed this to be insignificant.

The relatively low field strength used here may be the reason why no variation is seen in these experiments. It has been shown that the BOLD effect increases with static magnetic field strength because the magnetic field gradients induced by the susceptibility differences increase with increasing field strength[14]. However, previous fMRI studies in the adult and fetal brain at 0.5 T have identified signal intensity variations during an auditory stimulus[18] using statistical approaches similar to those adopted here. The signal change shown in fetuses has been shown to be larger than that in adults, possibly due to differences in the susceptibilities of adult and fetal haemoglobin. Redpath *et al*[17] have also shown differences in the T_2^* values measured in the fetal liver when the mother has been hyper-oxygenated by breathing 100% oxygen. Both of these results would indicate that it is not unreasonable to expect to see T_2^* changes in the human placenta at 0.5 T through the maternal cardiac cycle.

Alternatively, the lack of any visible variation may be because the blood supply to the placenta is not pulsatile as assumed or because the geometry of the placenta is such that the magnetic field gradients generated are too small to have any detectable effect. The placenta is a very complex structure and before any conclusions could be made on the magnitude of any expected signal change, it would be necessary to produce a 3D map of the susceptibility variations within the placenta that could be converted into a 3D map of the magnetic fields expected. This could be used in a Monte Carlo simulation of the signal attenuation expected in gradient echo and spin echo sequences. However, to produce a map of susceptibility it is necessary to thoroughly model the haemodynamics of the oxygen exchange processes within the placenta. This would require investigation

of the oxygen transfer and blood flow through the intervillous spaces, the vessels within the villi and the regions immediately surrounding the villi.

To produce a model of the susceptibility variations would be very difficult because for the model to be realistic it would be crucial to have information about several factors:

- The relative oxygenation levels of the maternal and fetal blood supplies.

- The relative susceptibilities of fetal and maternal oxyhaemoglobin and deoxyhaemoglobin.

- The exact geometry of fetal vessels within the placenta and the distribution of oxygenated and deoxygenated maternal blood around them.

- The input functions of maternal and fetal blood into the placenta and how they vary through the maternal cardiac cycle.

Literature values[20] and experiments[21] could allow us to determine the first two of these factors but the final two present many more difficulties. Knowledge of the third factor is complicated by the loss in the structure of the placenta after delivery. *In vivo* the pressure of the maternal blood entering through the spiral arteries and moving around the fetal villi maintains the intervillous spaces. During delivery, the fetal side of the placenta comes away from the wall of the uterus and the structure collapses. *In vitro* histological observation can give an indication of the placental structure[16] *in vivo* but a functional model of how maternal blood circulates around the villi would be necessary to allow an appropriate geometrical model to be created. The final point could probably be best determined by direct measurements using MRI. However, sufficient precision is not currently available.

9.3   Cardiac Gated T_2 Weighted Imaging

9.3.1   Theory

Before the demonstration of the BOLD effect in 1990 by Ogawa *et al*[3] in gradient echo images, Thulborn *et al*[4] demonstrated an oxygenation level dependence of the transverse relaxation time, T_2, of blood in 1982. Thulborn *et al* attributed this dependence to the motion of spins through the magnetic field gradients surrounding deoxygenated red blood cells. It has since been shown by Van Zijl *et al*[22], Bryant *et al*[23] and Wright *et al*[24] that the dependence observed by Thulborn was in fact due to the exchange of spins in and out of the red blood cells and the associated jump in magnetic susceptibility that they experience. Following on from the Luz-Meiboom model of relaxation in the presence of exchange between two sites at different frequencies, several groups have proposed equations to describe the dependence of blood T_2 on the oxygenation level[22,23,24]. In particular Wright *et al*[24] have formulated the following equation to describe how the transverse relaxation time of blood, T_2^b, varies with the percentage of haemoglobin that is oxygenated, %HbO$_2$.

$$\frac{1}{T_2^{\,b}} = \frac{1}{T_2^{\,0}} + P_A\left[1 - P_A\right]\tau_{ex}\left[\left(1 - \frac{\%HbO_2}{100\%}\right)\alpha\omega_0\right]^2\left[1 - \frac{2\tau_{ex}}{\tau_{180}}\tanh\left(\frac{\tau_{180}}{2\tau_{ex}}\right)\right] \quad - \quad 9.1$$

In this equation, $T_2^{\,0}$ is the T_2 value of 100% oxygenated blood, P_A is the fraction of protons resident at one of the exchange sites and can be equated to the haematocrit of the blood, Hct. Also, τ_{ex} is the average time required for a proton to move between the sites, ω_0 is the resonant proton frequency, τ_{180} is the echo time of the spin echo experiment and α is a dimensionless constant that describes the

susceptibility of deoxyhaemoglobin and the geometry of the red blood cell. The term $[(1-(\%HbO_2/100\%))\alpha\omega_0]$ can be considered to be the difference in frequency between the two sites of interest and can be compared to the term $\Delta\omega$ in the similar equation published by Van Zijl et al[22].

To apply equation 9.1 in a spin echo measurement of the human placenta at 0.5 T, it is necessary to obtain estimates for the various parameters. Following the work of Van Zijl et al[22], in human adult blood the exchange time, τ_{ex}, can be assumed to be 10 ms, the haematocrit can be assumed to be 42% and the frequency difference upon exchange between the red blood cell and the surrounding plasma can be given by equation 9.2, where Y is the fraction of oxygenated haemoglobin.

$$\Delta\omega = -0.0234\,ppm - 0.217\,ppm \times [1 - Y] \qquad - \qquad 9.2$$

Previous measurements, shown in chapter 8, have revealed the transverse relaxation time in the human placenta at 0.5 T to be between 150 and 300 ms and from this it would seem that a reasonable estimate of T_2^0 would be 300 ms. Using these values and the oxygen levels obtained from the literature[20], table 9.2 details the transverse relaxation time expected in the different vessels supplying the placenta from a spin echo measurement with an echo time of 120 ms.

These values would suggest that although not particularly large, there is an observable difference in the T_2 of the blood flowing into and out of the placenta through the maternal and fetal vessels at 0.5 T. This would suggest that there might be differences in the observed transverse relaxation of the placenta as oxygenated blood enters and deoxygenated blood is removed through the maternal cardiac cycle.

Blood Vessel	Approximate Oxygenation Level / %	T_2 Value Expected from Equation 9.1 / ms
Maternal Arteries	99	298
Maternal Veins	75	280
Fetal Arteries	52	252
Fetal Veins	88	292

Table 9.2 – Estimated T_2 Values in the Vessels Supplying the Placenta

9.3.2 Experimental Method

In a similar method to that used in section 9.2, any differences in the T_2 value

of the placenta through the maternal cardiac cycle can be monitored by producing

T_2 weighted images at different points through the maternal R-R interval. This can

be achieved with the use of a spin echo EPI acquisition that is cardiac gated to the

maternal heart rate. With this aim, six further volunteers were recruited as

described in section 9.2.3 and were scanned on one occasion each. The gestational

ages of the volunteers on the date of their scan ranged from 18 to 29 weeks with

an average gestational age of 24 weeks (S.D. = 4). As before, each volunteer

underwent a standard ultrasound examination and a transverse multi-slice set of

images was acquired to allow for localisation of the placenta and selection of an

imaging slice adjacent to the site of umbilical cord insertion. An ECG trace of the

maternal heart was obtained and T_2 weighted images acquired at a series of points

along the trace using the spin echo sequence shown in figure 9.3. The resolution

and EPI parameters were as described in section 9.2.3 and the images were

acquired with an echo time, T_E, of 120 ms and a repetition time, T_R, of 15 s. Five images were acquired at each of six different points evenly spaced along the maternal cardiac cycle. An echo time of 120 ms was used because any oxygenation variation in the transverse relaxation time increases with the echo time used and 120 ms is long enough to maximise any oxygenation variation of the signal intensity whilst still yielding sufficient signal to produce images of the placenta.

The acquired data was initially processed into modulus images and the average signal intensity in a region of interest drawn to encompass the whole placenta was measured using Analyze. As before the average signal intensity was plotted against time through the maternal cardiac cycle and then analysed to determine any variation in the signal intensity through the cardiac cycle.
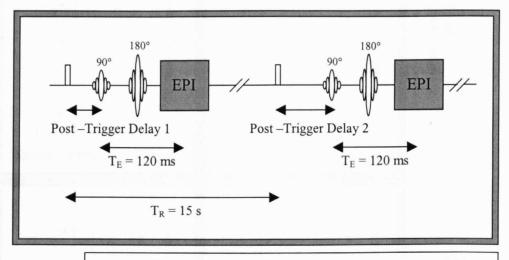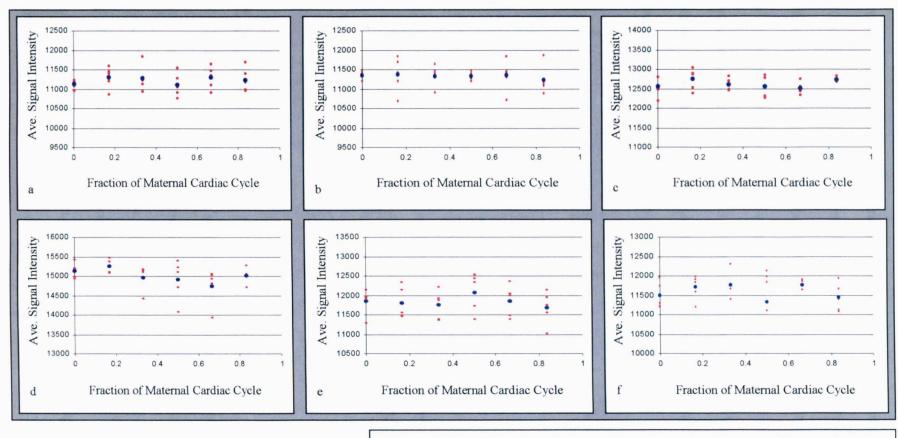

Figure 9.3 – Cardiac Gated T_2 Weighted Image Acquisition

Figures 9.4a-f – Raw (Red Dots) and Average (Blue Dots) Signal Intensities from Maternal Cardiac Gated T_2 Weighted Images of the Human Placenta.

9.3.3   Results

Figure 9.4 shows the raw data for all volunteers, the average signal intensity is represented by a blue dot and the individual data points are represented as red dots to give an indication of the spread in the data. As with the gated T_2^* results, there is no common trend for the signal intensity to vary through the maternal cardiac cycle. However, there is a low amplitude sinusoidal variation in four of the volunteers (a, c, d and e) but it is well within the spread of the data. Table 9.3 shows the single factor ANOVA statistics for all six volunteers and indicates no statistically significant variation between the data points.

Volunteer Number	P Value – From ANOVA
a	0.62
b	0.94
c	0.23
d	0.11
e	0.54
f	0.44

Table 9.3 – Single Factor ANOVA Statistics from Cardiac Gated T_2 Weighted Images

9.3.4   Discussion

The lack of any significant variation in the measured signal intensities during the maternal cardiac cycle demonstrates that there is no significant transverse relaxation time change in the placenta during this period. The calculations performed in section 9.3.2 would suggest that a detectable difference should be seen between the blood entering and leaving the placenta, especially that in the fetal arteries and veins. However, the assumption that T_2^0 is 300 ms may not be

valid and it should be noted that fetal haemoglobin is not the same as that in adult blood, meaning the fetal calculations based on literature values of susceptibility differences between adult red blood cells and plasma may not be correct.
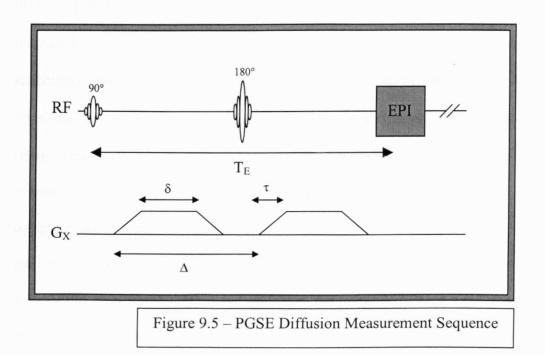
Probably the most important reason why no variation was seen is due to the distribution of blood within the placenta. When oxygenated maternal blood enters the placenta with a high T_2 value, it will surround the fetal villi containing blood at a lower oxygenation level and therefore a lower T_2 value. The measured T_2 value at this point will be an average of the two relaxation times. As oxygen is transferred between the maternal and fetal circulations, the oxygenation levels in the two circulations will become similar and therefore have similar T_2 values. This means that although there should be a measurable difference between the blood flowing into and out of the placenta, the variation within the placenta during the maternal cardiac cycle may be limited by averaging of the relaxation times.

To further investigate any transverse relaxation time, T_2, changes through the maternal cardiac cycle, accurate modelling of the distribution of oxygenated and deoxygenated blood in the placenta as discussed in section 9.2.5 is necessary. Also, performing the experiments at a field strength higher than 0.5 T would increase the size of any variation due to an increased susceptibility difference between the red blood cells and the plasma.

9.4 Diffusion Measurement with Anti-Symmetric Gradients – Sequence Validation

9.4.1 Theory

Rather than attempting to identify variations in the signal intensity of T_2^* or T_2 weighted images through the maternal cardiac cycle, it may be possible to directly investigate any magnetic field gradients that are generated in or between the maternal and fetal circulations of the placenta. As mentioned previously, the presence of deoxyhaemoglobin, and the local magnetic field gradients that it produces, will affect the intensity of diffusion-weighted images and therefore lead to an incorrect measure of the diffusion coefficient[25,26,27]. The reason behind this effect is the fact that local magnetic field gradients combine in a complex way with the gradients that are used to generate the diffusion weighting in a standard Pulsed Gradient Spin Echo (PGSE) measurement.

Figure 9.5 – PGSE Diffusion Measurement Sequence

In PGSE sequences[28], such as the one shown in figure 9.5, the signal intensity in a diffusion-weighted image will follow the form of equation 9.3.
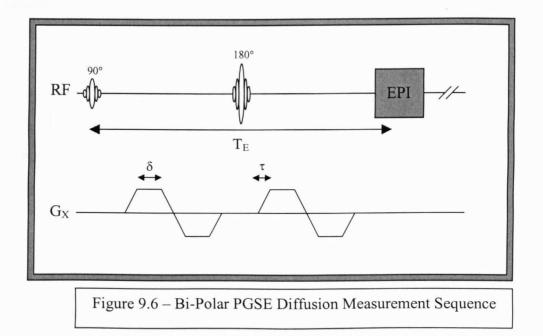
$$S(b) = S_0 e^{-bD} \qquad\qquad - \qquad 9.3$$

Where S_0 is a constant relating to the image intensity, D is the diffusion coefficient and b is a factor relating to the size of the sensitising gradients. The magnitude of the b term is calculated using equation 9.4.

$$b = \gamma^2 \int_0^{t} \left| \int_0^{t'} G(t'') dt' \right|^2 dt' \qquad - \qquad 9.4$$

Where G(t'') is the magnitude of pulsed magnetic field gradients, also known as the sensitising gradients. The calculation of b for typical gradient waveforms leads to an expression that is proportional to the square of the sensitising gradient magnitude. A measure of the diffusion coefficient can be obtained by varying the sensitising gradient magnitude and plotting the logarithm of the resulting signal intensities as a function of the square of the gradient strength. This will yield a linear variation that is proportional to the diffusion coefficient. However, this task becomes more complicated in the presence of other gradients that have components in the same direction as the sensitising gradients[29]. These other gradients can arise in certain imaging sequences (although they are not a problem with EPI as implemented here) and also from the presence of local field gradients generated within a sample. It is this case that is of interest in the study of placental oxygenation.

9.4.2 Calculation of Sensitising Gradient Strength

In the presence of any local background gradients in the same direction as the sensitising gradients, the G(t'') term in equation 9.4 will become the sum of two gradient terms, G_S, the sensitising gradient, and G_L, the local background gradient. The presence of this sum will lead to cross terms in the final solution that involve the product of G_S and G_L. These cross terms cannot be calculated when the local gradient magnitude is unknown but their contribution will change with variation of the sensitising gradient magnitude, causing errors in any measurement of the diffusion coefficient. These errors can be overcome with the use of a PGSE sequence that utilises anti-symmetric gradients like those in the bi-polar PGSE sequence shown in figure 9.6[29]. The form of these gradients causes the cross terms that hamper the standard PGSE sequence to cancel out and as such yields an accurate measurement of the diffusion coefficient. The expanded form of equation 9.4 for both the standard and the bi-polar PGSE sequences are given below for the case of no background gradient and a constant background gradient of amplitude, G_L.

Figure 9.6 – Bi-Polar PGSE Diffusion Measurement Sequence

Assuming there are no local gradients, G_L, to consider, it is possible to expand equation 9.4 for both the bi-polar and the standard PGSE sequences to yield a measure of b as a function of the sequence parameters and the sensitising gradient strength. Equation 9.5 shows the result for the standard PGSE sequence and equation 9.6 shows the result for the bi-polar PGSE sequence.

$$b = \gamma^2 G_S^2 \left[\frac{2}{3}\left(\delta + \frac{3\tau}{2}\right)^3 - \frac{43\tau^3}{60} - \frac{2\delta\tau^2}{3} + (\delta + \tau)^2 (\Delta - \delta - 2\tau) \right] \qquad - \qquad 9.5$$

$$b = \frac{1}{15}\gamma^2 G_S^2 \left[46\tau^3 + 20\delta^3 + 90\tau\delta^2 + 115\tau^2\delta \right] \qquad - \qquad 9.6$$

If a background gradient is now introduced, G_L, that is assumed to be constant throughout the duration of the experiment and in the same direction as the sensitising gradients, then the expansions can be repeated to provide a corrected measure of b. Equation 9.7 shows the results for the standard PGSE sequence and equation 9.8 shows the results for the bi-polar PGSE sequence.

$$b = \gamma^2 \begin{bmatrix} \frac{-7}{15}\tau^3 G_S^2 - \frac{1}{3}\delta^3 G_S^2 + \tau^2 \Delta G_S^2 + 2\tau\delta\Delta G_S^2 + \delta^2 \Delta G_S^2 \\ -\tau\delta^2 G_S^2 - \frac{7}{6}\tau^2\delta G_S^2 - \frac{1}{6}\delta^3 G_S G_L - \frac{1}{2}\tau\delta^2 G_S G_L \\ -\frac{1}{2}\tau\Delta^2 G_S G_L - \frac{1}{3}\tau^3 G_S G_L - \frac{1}{2}\delta\Delta^2 G_S G_L - \frac{2}{3}\tau^2\delta G_S G_L \\ + \tau T_E \Delta G_S G_L + T_E \delta \Delta G_S G_L + \frac{1}{12}T_E^3 G_L^2 \end{bmatrix} \qquad - \qquad 9.7$$

$$b = \gamma^2 \left[\frac{4}{3}\delta^3 G_S^2 + 6\tau\delta^2 G_S^2 + \frac{23}{3}\tau^2\delta G_S^2 + \frac{46}{15}\tau^3 G_S^2 + \frac{1}{12}T_E^3 G_L^2 \right] - \qquad 9.8$$

Study of the two bi-polar PGSE equations shows that, with the exception of the single G_L term at the end of equation 9.8, the two equations are the same. The fact that there are no cross-terms involving both gradient parameters means that any diffusion measurement will not be affected by the presence of a background gradient. The only effect will be an increase in the absolute value of b and this will not affect the way that b varies with an increase in the sensitising gradient strength. The same cannot be said for the two standard PGSE equations. The inclusion of a background gradient term greatly complicates the calculation of b with the inclusion of numerous cross-terms. These cross terms, if neglected, will lead to the measurement of signal intensities that do not vary linearly with increasing sensitising gradient strength and will cause errors in the measurement of the diffusion coefficient. However, comparison of the results from the two sequences allows for the production of an estimate of the background gradient, assuming that it is constant over the length of a pixel.

9.4.3   Experimental Method

The ability of the bi-polar PGSE sequence, shown in figure 9.6, to correct for cross terms caused by background magnetic field gradients was validated by comparing it to a standard PGSE sequence, as shown in figure 9.5. A temporally constant long-range magnetic field gradient was applied in the broadening gradient direction by applying a current to the X-shim coil. The strength of the gradient produced was determined by measuring the current applied and the validation was repeated at a series of currents to allow for a thorough examination of the sequence's abilities. Initially the bi-polar PGSE sequence was applied in the measurement of the diffusion coefficient of a cylindrical phantom of water at

room temperature. The sequence was applied with a ramp time, τ, of 2 ms, a gradient duration, δ, of 35 ms, an echo time, T_E, of 440 ms and a repetition time, T_R, of 15 s. The sequence was repeated three times at each of seven different sensitising gradient strengths with b values ranging from 0 to 341 smm^{-2}. The diffusion measurement was subsequently repeated twice using the standard PGSE sequence, once with positive gradient lobes and once with negative lobes. The standard PGSE sequence was applied with a ramp time, τ, of 2 ms, a gradient duration, δ, of 14 ms, a gradient lobe separation, Δ, of 60 ms, an echo time, T_E, of 440 ms and a repetition time, T_R, of 15 s. The sequence was applied three times at each of seven different sensitising gradient strengths with b values ranging from 0 to 341 smm^{-2}. The whole validation experiment was then repeated four times with currents on the X-shim coil of 1, 2, 3 and 4 Amps.

The acquired data was post processed into magnitude images and the average signal intensity in a region of interest covering the sample was measured using Analyze. The signal intensities were averaged over the repetitions and plotted against their corresponding b value in Excel. The fitting procedure within Excel was then used to provide a measure of the diffusion coefficient by following the form of equation 9.3. The data from the standard PGSE data was then used to provide a measure of the background gradient strength by substituting equation 9.7 into equation 9.3 and using the diffusion coefficient value obtained with the bi-polar PGSE sequence. The solver tool within Excel was then used to fit the experimental data to the form of the new equation 9.3 by varying the size of the background gradient, G_L. This process was carried out for both the positive and negative gradient lobe implementations of the standard PGSE sequence at each of the current values investigated.

9.4.4 Results

Figure 9.7a shows an example of the diffusion plots for all three measurements at a X-shim current of 3 A. It can be seen that the bi-polar PGSE sequence yields data with an exponential decrease with increasing b values. In comparison the standard PGSE sequences provide a poor fit to the exponential form expected and diffusion measurements that differ from the bi-polar sequence. Table 9.4 gives the diffusion coefficients produced by all three sequences, it can be seen that the diffusion coefficients yielded by the positive standard PGSE sequence decrease and those yielded by the negative standard PGSE sequence increase with increasing current applied on the shim coil.

X-Shim Current / A	Diffusion Coefficient from Bi-Polar PGSE Sequence ($\times 10^{-3}$ mm^2/s)	Diffusion Coefficient from Positive Standard PGSE Sequence ($\times 10^{-3}$ mm^2/s)	Diffusion Coefficient from Negative Standard PGSE Sequence ($\times 10^{-3}$ mm^2/s)
0	2.19	2.29	2.05
1	2.10	1.84	2.51
2	2.22	1.39	2.88
3	2.12	0.85	3.37
4	2.13	0.36	3.72

Table 9.4 – Fitted values of D for all Three Sequences

Figure 9.7b shows the variation in the fitted values of G_L with shim current. It can be seen that the positive and negative sequences yield very similar results. By examining the gradients of the two lines in figure 9.7b, the efficiency of the X-shim coil was calculated to be 1.5 mTm^{-1}A^{-1} (Positive Sequence – 1.4 mTm^{-1}A^{-1} and Negative Sequence – 1.6 mTm^{-1}A^{-1}). This is in agreement with the measured efficiency of the coil, which was found to be 1.5 mTm^{-1}A^{-1}.
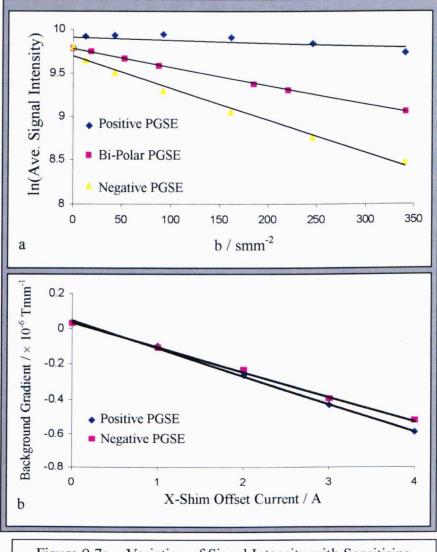

Figure 9.7a – Variation of Signal Intensity with Sensitising Gradient Strength in the Presence of a Background Gradient Caused by a 3 A Current on the X-Shim Coil.
Figure 9.7b – Variation in the Measured Background Gradient with X-Shim Current.

9.4.5   Discussion

The initial application of the bi-polar PGSE proved challenging due to the increased gradient amplitude necessary to match the diffusion sensitivity of the standard PGSE sequence. Technical limitations meant that the length of the bi-polar lobes needed to be increased and therefore an extension of the echo time was necessary. The application of the bi-polar sequence to the study of diffusion in the presence of background gradients showed its ability to overcome the cross-terms that affected the standard PGSE technique. The bi-polar sequence yielded a diffusion coefficient measurement that was unaffected by the size of the background gradient. The validation of the sequence also showed that by combining bi-polar PGSE and standard PGSE measurements, it is possible to produce an accurate measurement of the magnitude of background gradients. Further study of figure 9.7 reveals that the two lines do not pass through the origin and that there is a systematic difference between their gradients. This difference is due to a current offset being produced by the Techron gradient amplifiers causing a further small background gradient. This current offset does not affect normal imaging because it is usually compensated for by using an equal and opposite current in the shim coil.

9.5 Application of the Technique

9.5.1 Susceptibility-Induced Gradients in the Human Placenta

The experiments carried out in the previous section highlight the ability of the bi-polar sequence to produce diffusion measurements in the presence of large background gradients that are constant in time and in space. The ability of the bi-polar sequence, when combined with a normal PGSE sequence, to measure the magnitude of these gradients is also demonstrated. However, these long-range gradients are not representative of the localised gradients that would be expected within the placenta.

As with the BOLD theory covered in section 9.2.1, there are three regimes that should be considered when investigating susceptibility-induced gradients:

- Long-range gradients that are constant over a voxel.

- Short-range gradients that change appreciably over the distance that a spin diffuses during an echo time.

- Medium-range gradients that lie in between the other two ranges.

As discussed by Hong and Dixon[29], the bi-polar sequence is able to correct for errors introduced by long- and medium-range gradients. Within the placenta it is assumed that the gradients would be in the medium-range, where the gradients are varying within a voxel but are long enough so that the gradient experienced by a spin is approximately constant during an echo time. This is similar to the case discussed by Hong and Dixon of the susceptibility gradients induced with an apple. Here the gradients vary over the range of a voxel and a Gaussian distribution can be used to describe the gradients such that for every position with a given gradient strength there is another position with the opposite gradient.

Many different phantoms were constructed to simulate these medium-range local field gradients, including oil drop emulsions, fruit and Levovist ultrasound contrast agent (Schering AG, Berlin). All of these phantoms should have contained perturbers surrounded by local field gradients due to magnetic susceptibility differences between the inner and outer components. However, none of the phantoms showed any difference between the standard PGSE sequence and the bi-polar PGSE sequence. The reason that no difference was shown is most probably because of a low susceptibility difference, and hence small local field gradient, due to the low static field strength being used. Repetition of these experiments, as in the work of Hong and Dixon, at higher field strengths may produce stronger local gradients and therefore a measurable difference.

9.5.2   Flow Measurements in the Human Placenta

Although it appears as if the susceptibility variations at 0.5 T are too small to be easily studied with any of the methods described so far, there is valuable information that could be gained through the application of the bi-polar PGSE sequence in the human placenta. The bi-polar PGSE sequence, as well as correcting for gradient offsets and localised inhomogeneities, is also a flow compensated sequence[29]. This means that spins that have a constant velocity do not acquire a phase shift during the application of the bi-polar PGSE sequence as they do with the standard PGSE sequence. In the standard PGSE sequence, if there are different spins moving with a range of velocities inside a voxel, the phase shifts they acquire will lead to attenuation of the measured signal intensity[28]. As the bi-polar PGSE sequence does not lead to any phase shifts, there is no loss of intensity in the acquired images due to spins moving with a constant

velocity. This difference between the two sequences leads to them being sensitive to different types of flow and movement within a voxel and as such may provide useful information about the movement of blood within the human placenta.

It has previously been shown that the application of the standard PGSE sequence in the human placenta yields a bi-exponential signal decay that follows the form of equation 9.9[30].

$$S = S_0\left[(1-f)e^{-bD} + fe^{-bD^*}\right] \qquad - \qquad 9.9$$

Where D is the diffusion coefficient, D^* is the pseudo-diffusion coefficient and f is a measure of the fraction of blood within a voxel that is randomly moving. The pseudo-diffusion coefficient is associated with perfusion and in the placenta is considered to arise from blood that is undergoing diffusion like motions through the randomly orientated capillary network. Within the bi-exponential, the pseudo-diffusion term arises due to the effect of low amplitude sensitising gradients on fast moving blood, whereas the normal diffusion term dominates at higher sensitising gradient amplitudes.

9.5.3   Experimental Method

To investigate the effect that the bi-polar sequence has on diffusion and pseudo-diffusion measurements in the human placenta, a single volunteer was recruited during a routine examination on the basis of a normal healthy pregnancy and was scanned on a single occasion at 31 weeks gestational age. As before, the volunteer received a standard ultrasound examination and a transverse multi-slice set of images was acquired to enable localisation of the placenta and selection of a

slice adjacent to the point of umbilical cord insertion. An ECG trace of the maternal heart was obtained and the R-wave was used to gate the subsequent image acquisition to a point a third of the way through the maternal cardiac cycle. A diffusion measurement was conducted using the PGSE sequence shown in figure 9.5. Three repeats were obtained at each of eight different gradient sensitising strengths with corresponding b values ranging from 0 to 241 s/mm^2. The images were acquired with encoding parameters and a resolution as described in section 9.2.3. The sequence was applied with an echo time, T_E, of 240 ms and a repetition time, T_R, of 15 s. The PGSE gradient lobes were 14 ms long (δ) with 2 ms ramps (τ) and a separation between the leading edges of the lobes of 60 ms (Δ). Subsequently, a second diffusion measurement was made using the bi-polar PGSE sequence shown in figure 9.6. Again three repeats were taken at each of eight different gradient sensitisation strengths, this time ranging from 0 to 265 s/mm^2. The echo time, T_E, was 240 ms and the repetition time, T_R, was 15 s. The bi-polar lobes were 35 ms long (δ) with 2 ms ramps (τ).

Both diffusion measurements were analysed in the same way. The data was initially processed into modulus images and then the average signal intensity in a region of interest drawn to encompass the whole placenta was measured using Analyze. The average intensities were then used to fit for the parameters f, D and D* in equation 9.9 using the solver tool within Microsoft$^{®}$ Excel 2000.

9.5.4 Results

Figure 9.8 shows the variation in the average signal intensity with sensitising gradient strength for the two diffusion measurements conducted. It can be seen that the standard PGSE sequence leads to a more rapid initial attenuation of the

signal than the bi-polar sequence. The fitted values for f, D and D* are shown in table 9.5. Good agreement is shown in the value of f, with the bi-polar sequence leading to a slightly lower value for D and a considerably lower value for D*.
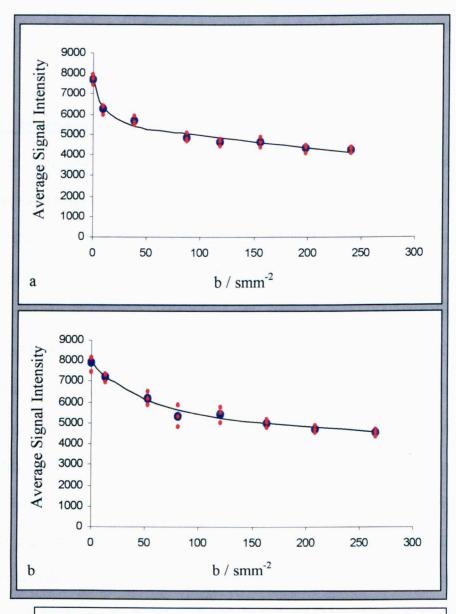

a

b

Figure 9.8a – Variation in Average Signal Intensity with Sensitising Gradient Strength for PGSE Sequence.
Figure 9.8b – Variation in Average Signal Intensity with Sensitising Gradient Strength for Bi-Polar PGSE Sequence

Sequence	f / %	D / $\times 10^{-3}$ mm^2s^{-1}	D^* / $\times 10^{-3}$ mm^2s^{-1}
PGSE	0.27	1.3	107
Bi-Polar PGSE	0.27	0.9	26

Table 9.5 – Fitted values of F, D and D^* for Both Sequences

9.5.5   Discussion

The similarity in the fitted values for f show that, due to both sequences having similar sensitising times, they both separate diffusion and pseudo-diffusion in the same way. The measurement of f has previously been shown to be reduced in pregnancies compromised by IUGR and Pre-Eclampsia[31] and this data would imply that the measurement of f is unaffected by using a bi-polar rather than standard PGSE sequence. The large difference in the measured value of D^* is an indication of the different sensitivities the two sequences have to different types of blood movements. Images measured with both sequences will have signal intensity attenuation that arises from spins moving incoherently on the scale of a voxel, either in the form of molecular diffusion or in the pseudo-diffusion of blood within capillary loops and the intervillous space. However, the bi-polar PGSE sequence will not lead to signal attenuation from spins that are moving with a constant velocity within a voxel. This fact explains the reduced attenuation, and hence lower D^* value, obtained at low b values. It may also, to a much smaller extent, explain the slight difference between the measured values of D.

The work presented here is simply an indication of the ability of the bi-polar PGSE sequence to study blood movement within the human placenta. A much

wider application of the sequence is necessary to further our understanding of blood motion within the placenta. An investigation of the effect of altering the sensitising times, as well as exploring the heterogeneity within the placenta, would yield even more information.

9.6 Conclusion

Unfortunately none of the applied methods yielded a robust method of studying the oxygenation level of blood within the human placenta. The acquisition of cardiac gated T_2^* and T_2 images at various points through the maternal cardiac cycle showed no statistically significant variation in signal intensity. Further study is necessary to provide a conclusion on this point, possibly with the experiments being conducted at a higher field strength or with correlation to a theoretical model being performed. A different approach could also be taken by trying to alter the oxygenation level of the maternal blood by allowing the volunteer to breathe 100% oxygen during the experiment.

The use of anti-symmetric sensitising gradients proved to be an accurate method for assessing diffusion in the presence of large background field gradients but gave little information about localised susceptibility based gradients. This was most probably due to the low field strength used to perform the experiments. However, the bi-polar PGSE sequence did yield useful information about the motion of blood within the placenta. The bi-polar sequence was able to produce flow compensated images that, in addition to standard PGSE techniques, could provide an interesting method of studying the incoherent motions of blood in the different regions of the placenta.

References

[1] Baker, P.N., et al., *Fetal Weight Estimation by Echo-Planar Magnetic-Resonance- Imaging.* Lancet, 1994. **343**(8898): p. 644-645.

[2] Baker, P.N., et al., *Measurement of Fetal Liver, Brain and Placental Volumes with Echo-Planar Magnetic-Resonance-Imaging.* British Journal of Obstetrics and Gynaecology, 1995. **102**(1): p. 35-39.

[3] Ogawa, S., et al., *Oxygenation-Sensitive Contrast in Magnetic-Resonance Image of Rodent Brain at High Magnetic-Fields.* Magnetic Resonance in Medicine, 1990. **14**(1): p. 68-78.

[4] Thulborn, K.R., et al., *Oxygenation Dependence of the Transverse Relaxation-Time of Water Protons in Whole-Blood at High-Field.* Biochimica Et Biophysica Acta, 1982. **714**(2): p. 265-270.

[5] Zhong, J.H. and J.C. Gore, *Studies of Restricted Diffusion in Heterogeneous Media Containing Variations in Susceptibility.* Magnetic Resonance in Medicine, 1991. **19**(2): p. 276-284.

[6] Ogawa, S., et al., *Brain Magnetic-Resonance-Imaging with Contrast Dependent on Blood Oxygenation.* Proceedings of the National Academy of Sciences of the United States of America, 1990. **87**(24): p. 9868-9872.

[7] Ogawa, S., et al., *Intrinsic Signal Changes Accompanying Sensory Stimulation - Functional Brain Mapping with Magnetic-Resonance-Imaging.* Proceedings of the National Academy of Sciences of the United States of America, 1992. **89**(13): p. 5951-5955.

[8] Ogawa, S., et al., *Functional Brain Mapping by Blood Oxygenation Level-Dependent Contrast Magnetic-Resonance-Imaging - a Comparison of Signal Characteristics with a Biophysical Model.* Biophysical Journal, 1993. **64**(3): p. 803-812.

[9] Jezzard, P. and R. Turner, *Magnetic resonance imaging methods for study of human brain function and their application at high magnetic field.* Computerized Medical Imaging and Graphics, 1996. **20**(6): p. 467-481.

[10] Jezzard, P. and A.W. Song, *Technical foundations and pitfalls of clinical fMRI.* Neuroimage, 1996. **4**(3): p. S63-S75.

[11] Kennan, R.P., J.H. Zhong, and J.C. Gore, *Intravascular Susceptibility Contrast Mechanisms in Tissues.* Magnetic Resonance in Medicine, 1994. **31**(1): p. 9-21.

[12] Weisskoff, R.M., et al., *Microscopic Susceptibility Variation and Transverse Relaxation - Theory and Experiment.* Magnetic Resonance in Medicine, 1994. **31**(6): p. 601-610.

[13] Boxerman, J.L., et al., *The Intravascular Contribution to Fmri Signal Change - Monte- Carlo Modeling and Diffusion-Weighted Studies in-Vivo.* Magnetic Resonance in Medicine, 1995. **34**(1): p. 4-10.

[14] Ogawa, S. and T.M. Lee, *Magnetic-Resonance-Imaging of Blood-Vessels at High Fields - Invivo and Invitro Measurements and Image Simulation.* Magnetic Resonance in Medicine, 1990. **16**(1): p. 9-18.

[15] Bauer, W.R., et al., *Theory of the BOLD effect in the capillary region: An analytical approach for the determination of T-2* in the capillary network of myocardium.* Magnetic Resonance in Medicine, 1999. **41**(1): p. 51-62.

[16] Jackson, M.R., T.M. Mayhew, and P.A. Boyd, *Quantitative Description of the Elaboration and Maturation of Villi from 10 Weeks of Gestation to Term.* Placenta, 1992. **13**(4): p. 357-370.

[17] Wallis, F., et al., *Measurement of fetal liver T2*in utero before and after maternal oxygen breathing-progress toward a noninvasive measurement of fetal oxygenation.* Radiology, 1999. **213P**: p. 261.

[18] Moore, R.J., et al., *Antenatal determination of fetal brain activity in response to an acoustic stimulus using functional magnetic resonance imaging.* Human Brain Mapping, 2001. **12**(2): p. 94-99.

[19] Vadeyar, S.H., et al., *Effect of fetal magnetic resonance imaging on fetal heart rate patterns.* American Journal of Obstetrics and Gynecology, 2000. **182**(3): p. 666-669.

[20] Widdicombe, J. and A. Davies, *Respiratory Physiology.* 2nd ed. 1992: Edward Arnold. 132.

[21] Weisskoff, R.M. and S. Kiihne, *Mri Susceptometry - Image-Based Measurement of Absolute Susceptibility of Mr Contrast Agents and Human Blood.* Magnetic Resonance in Medicine, 1992. **24**(2): p. 375-383.

[22] van Zijl, P.C.M., et al., *Quantitative assessment of blood flow, blood volume and blood oxygenation effects in functional magnetic resonance imaging.* Nature Medicine, 1998. **4**(2): p. 159-167.

[23] Bryant, R.G., et al., *Magnetic-Relaxation in Blood and Blood-Clots.* Magnetic Resonance in Medicine, 1990. **13**(1): p. 133-144.

[24] Wright, G.A., B.S. Hu, and A. Macovski, *Estimating Oxygen-Saturation of Blood Invivo with Mr Imaging at 1.5t.* Jmri-Journal of Magnetic Resonance Imaging, 1991. 1(3): p. 275-283.

[25] Zhong, J.H., R.P. Kennan, and J.C. Gore, *Effects of Susceptibility Variations on Nmr Measurements of Diffusion.* Journal of Magnetic Resonance, 1991. 95(2): p. 267-280.

[26] Clark, C.A., G.J. Barker, and P.S. Tofts, *An in vivo evaluation of the effects of local magnetic susceptibility-induced gradients on water diffusion measurements in human brain.* Journal of Magnetic Resonance, 1999. 141(1): p. 52-61.

[27] Does, M.D., J.H. Zhong, and J.C. Gore, *In vivo measurement of ADC change due to intravascular susceptibility variation.* Magnetic Resonance in Medicine, 1999. 41(2): p. 236-240.

[28] Norris, D.G., *Implications of Bulk Motion for Diffusion-Weighted Imaging Experiments: Effects, Mechanisms, and Solutions.* Journal of Magnetic Resonance Imaging, 2001. 13: p. 486-495.

[29] Hong, X.L. and W.T. Dixon, *Measuring Diffusion in Inhomogeneous Systems in Imaging Mode Using Antisymmetric Sensitizing Gradients.* Journal of Magnetic Resonance, 1992. 99(3): p. 561-570.

[30] Moore, R.J., et al., *In vivo intravoxel incoherent motion measurements in the human placenta using echo-planar imaging at 0.5 T.* Magnetic Resonance in Medicine, 2000. 43(2): p. 295-302.

[31] Moore, R.J., et al., *In utero perfusing fraction maps in normal and growth restricted pregnancy measured using IVIM echo-planar MRI.* Placenta, 2000. 21(7): p. 726-732.

[32] Ahn, C.B. and Z.H. Cho, A Generalized Formulation of Diffusion Effects in Mu-M Resolution Nuclear Magnetic-Resonance Imaging. Medical Physics, 1989. 16(1): p. 22-28.

[33] Bauer, W.R. and K. Schulten, Theory of Contrast Agents in Magnetic-Resonance-Imaging - Coupling of Spin Relaxation and Transport. Magnetic Resonance in Medicine, 1992. 26(1): p. 16-39.

[34] Beaulieu, C. and P.S. Allen, An in vitro evaluation of the effects of local magnetic-susceptibility-induced gradients on anisotropic water diffusion in nerve. Magnetic Resonance in Medicine, 1996. 36(1): p. 39-44.

[35] Boxerman, J.L., et al., Mr Contrast Due to Intravascular Magnetic-Susceptibility Perturbations. Magnetic Resonance in Medicine, 1995. 34(4): p. 555-566.

[36] Fisel, C.R., et al., Mr Contrast Due to Microscopically Heterogeneous Magnetic- Susceptibility - Numerical Simulations and Applications to Cerebral Physiology. Magnetic Resonance in Medicine, 1991. 17(2): p. 336-347.

[37] Golay, X., et al., Measurement of tissue oxygen extraction ratios from venous blood T-2: Increased precision and validation of principle. Magnetic Resonance in Medicine, 2001. 46(2): p. 282-291.

[38] Grune, M., et al., Quantitative T-2* and T-2 ' maps during reversible focal cerebral ischemia in rats: Separation of blood oxygenation from nonsusceptibility-based contributions. Magnetic Resonance in Medicine, 1999. 42(6): p. 1027-1032.

[39] Hardy, P. and R.M. Henkelman, On the Transverse Relaxation Rate Enhancement Induced by Diffusion of Spins through Inhomogeneous Fields. Magnetic Resonance in Medicine, 1991. 17(2): p. 348-356.

[40] Henkelman, R.M., Does IVIM Meeasure Classical Perfusion? Magnetic Resonance in Medicine, 1990. 16: p. 470-475.

[41] Karlicek, R.F. and I.J. Lowe, A Modified Pulsed Gradient Technique for Measuring Diffusion in the Presence of Large Background Gradients. Journal of Magnetic Resonance, 1980. 37: p. 75-91.

[42] Lebihan, D., et al., Separation of Diffusion and Perfusion in Intravoxel Incoherent Motion Mr Imaging. Radiology, 1988. 168(2): p. 497-505.

[43] Lebihan, D., et al., Mr Imaging of Intravoxel Incoherent Motions - Application to Diffusion and Perfusion in Neurologic Disorders. Radiology, 1986. 161(2): p. 401-407.

[44] Lin, W.L., et al., Experimental hypoxemic hypoxia: Changes in R-2* of brain parenchyma accurately reflect the combined effects of changes in arterial and cerebral venous oxygen saturation. Magnetic Resonance in Medicine, 1998. 39(3): p. 474-481.

[45] Muller, R.N., et al., Transverse Relaxivity of Particulate Mri Contrast-Media - from Theories to Experiments. Magnetic Resonance in Medicine, 1991. 22(2): p. 178-182.

[46] Pekar, J., C.T.W. Moonen, and P.C.M. Vanzijl, On the Precision of Diffusion Perfusion Imaging by Gradient Sensitization. Magnetic Resonance in Medicine, 1992. 23(1): p. 122-129.

[47] Willcourt, R.J., J.C. King, and J.T. Queenan, Maternal Oxygenation Administration and the Fetal Transcutaneous-Po2. American Journal of Obstetrics and Gynecology, 1983. 146(6): p. 714-715.

10   Conclusions

10.1   Overview of Thesis

The development and implementation of various quantitative sequences, which allow for the characterisation of transverse relaxation times, magnetisation transfer and blood movement within the human placenta has been presented. Validation studies carried out on multi-echo imaging sequences have revealed that the imperfections in the inversion produced by a standard sinc pulse are too great to allow accurate quantification of the transverse relaxation time. Even the use of geometrically increasing spoiling gradients, balanced around the inversion pulses, does not sufficiently overcome the problems to yield an accurate measurement.

The implementation of adiabatic refocusing pulses, either two back to back hyperbolic secant pulses or a single BIREF2b pulse, yield a substantially improved inversion and as such a more accurate measurement of the transverse relaxation time. However, both pulses have their problems. The use of two HSC pulses leads to an increase in the inter echo spacing and the use of longer echo times. This in turn prevents the use of the sequence in the measurement of very short relaxation times. The BIREF2b pulse negates these problems because it is a refocusing pulse, as well as an accurate inversion pulse, but due to the relatively high RF power level needed to achieve an inversion, it can be technically difficult to implement.

The application of the HSC multi-echo sequence in the human placenta has shown the ability of the sequence to accurately measure the transverse relaxation time in an organ that is prone to unpredictable and non-periodic motions. The subsequent application of both the HSC and the BIREF2b multi-echo sequences in the study

of gastric function has highlighted the wider use of multi-echo imaging sequences in clinical applications.

The development of a quantitative magnetisation transfer sequence has demonstrated the potential for the combination of pulsed off-resonance irradiation and echo planar image acquisition to yield a measurement of the size of the bound proton pool in a clinically feasible imaging time. The lower RF power levels required when using pulsed irradiation combined with the minimal power deposition produced by the EPI acquisition lead to a sequence with no SAR issues. The SAR concerns are further reduced because the extension of the model suggested by Henkelman *et al* has allowed the study of the transient approach of the bound proton pool towards saturation rather than examining the system in the steady state.

The validation of the developed sequence and model in the study of agar gel phantoms has illustrated the various effects that the different model parameters have on the complex magnetisation transfer system. Of particular interest was the large effect caused by the degenerate nature of the bound proton pool transverse relaxation time at a given off-resonance frequency. The subsequent extension of the experiment to examine the variation of the off-resonance frequency lead to an improved technique that allowed for the measurement of the bound proton pool size and its transverse relaxation time. Extensive study of the agar gel phantoms yielded measurements that were accurately matched to those found in the published literature.

The measurement of the longitudinal and transverse relaxation times at various stages of normal pregnancies yielded results that were very similar to those previously published. However, the measurement of the relaxation times in

pregnancies compromised by IUGR or pre-eclampsia failed to repeat the previously shown reduction. In an attempt to explain the previous findings the quantitative magnetisation transfer sequence was applied and yielded a very mild trend for the size of the bound proton pool to increase with gestational age but showed no difference in compromised pregnancies. This gestational age trend may go some way towards explaining the reduction shown in the relaxation times but indicates that there is probably a combination of factors leading to the observed variations.

The attempt to quantify the oxygenation level within the human placenta proved to be a very difficult task. Acquisition of cardiac gated T_2^* and T_2 weighted images at various stages through the maternal cardiac cycle showed no statistically significant variation in intensity. A mild periodic variation was seen in some cases but the variation was too small to be quantifiable.

Validation of a PGSE sequence that utilised anti-symmetric sensitising gradients in the presence of a large background gradient confirmed the sequences ability to overcome cross-terms that can introduce errors into the standard PGSE sequence. However, subsequent application of the sequence in the measurement of local field gradients caused by susceptibility differences was not possible. The sequence was applied in the study of blood flow in the human placenta to examine its flow compensating properties. It was shown that the sequences yielded different results from a standard PGSE sequence due to the sensitivity of the two sequences to different types of flow.

10.2 Future Directions

There are several possible ways that the technical developments presented in this thesis could be extended and improved. The rapid measurement of the transverse relaxation time is a technique that could find application in many different settings. The two applications given herein are simply meant as an indication of the advantages that the technique provides when measuring T_2 in organs that are affected by motion. I feel sure that the technique will find different uses, possibly in the field of functional MRI. The multi-echo sequences discussed could be further improved with the use of lower SAR versions of the adiabatic refocusing pulses using the VERSE principal. There is also scope for producing a sequence that could measure both T_2 and T_2^* from just one or two FIDs.

The quantitation of the magnetisation transfer process is a field that is currently very exciting. I believe that the power of magnetisation transfer will lie in the ability to provide quantitative measurements that relate specifically to the biochemical environment. I feel that there is great potential for the sequence presented here to be applied in the study of the human brain, possibly in the study of conditions such as multiple sclerosis. There is a lot of scope for further improvement in the model presented here. Continued work on the study of the bound proton pool lineshape is necessary, along with optimisation of the image acquisition scheme to allow the most accurate fitting procedure from the model.

Monitoring oxygenation levels through the study of relaxation time effects is, I believe, a technique that will require study at field strength higher than 0.5 T. The same is true for the use of the bi-polar PGSE sequence in the study of oxygenation levels but there is scope for the further application of this sequence in the study of blood flow within the placenta and possibly fluid flow in other systems.